2-17-2017

Advanced Manufacturing and Microenvironment Control for Bioengineering Complex Microbial Communities

Andrea Kadiak
University of Connecticut - Storrs, akadilak@gmail.com

Advanced Manufacturing and Microenvironment Control for Bioengineering Complex Microbial Communities

Andrea Laura Kadilak, Ph.D.

University of Connecticut, 2017

Micro- and millifluidic, or lab-on-a-chip, devices are superior platforms for cell culture applications where replicating complex microenvironments or spatial interactions are important. Unlike traditional cell culture techniques, such as agar plates, liquid culture flasks, or microwell plates, they are able to more accurately reproduce the micro-scale geometry of actual environments. Furthermore, lab-on-a-chip microhabitats enable researchers to have better control over environmental conditions, such as oxygen, nutrient, or other chemical gradients, on a cellular scale. This research project aims to develop tools to enable replication of the oxygen and chemical gradients found within the termite digestive tract in order to culture and study the complex microbial community inhabiting termites in nature.

Reproducing the physiochemical environment inside the termite gut requires a number of engineering solutions. One particular design requirement is maintaining nearly anoxic conditions in much of the device, with a slightly oxic gradient near the exterior boundary. In order to accomplish this, a procedure was developed to fabricate microelectrodes *in situ* along the interior side walls of a microfluidic channel. Theoretically, at these microelectrodes, oxygen could be produced and used to supply the cell culture area of the device. While ultimately oxygen and nitrogen saturated liquids were used for establishing oxygen gradients within test devices due to

ease of use, the surface chemistry and specific photopatterning techniques developed can be used for a variety of other applications.

Additionally, a 3D-printed cell culture millifluidic device was designed and manufactured to enable long-term microbial cell culture. Methods were developed to test and minimize adverse biotoxicity effects of 3D-printed polymer, which had not previously been done with bacterial cells. Hydrogel polymer barriers were engineered to form a boundary between the substrate supply flow channel and the cell culture area of the designed device. These UV-patterned hydrogels allowed diffusion of oxygen, carbon substrates, and other important chemical species into the culture area, but successfully prevented cell motility out of the specified region when tested with the bacteria *Pseudomonas putida* KT2440. The *P. putida* cells were successfully cultured in this proof-of-concept device for 44 h, which had not been documented with a bacteria in a stereolithography 3D-printed channel before. The incorporation of additive manufacturing in this project has identified 3D-printed as an enabling technology for scaling up from microfluidic to millifluidic devices and making lab-on-a-chip technology more attainable for a wider variety of users. The techniques and engineering tools developed in this project may be applied to design, fabricate, and control conditions with a wide variety of cell types and synthetic microhabitat systems.

Advanced Manufacturing and Microenvironment Control for Bioengineering Complex Microbial Communities

Andrea Laura Kadilak

B.S. Worcester Polytechnic Institute, 2008

M.S., University of Connecticut, 2015

A Dissertation

Submitted in Partial Fulfillment of the

Requirements for the Degree of

Doctor of Philosophy

at the

University of Connecticut

2017

Doctor of Philosophy Dissertation

Advanced Manufacturing and Microenvironment Control for Bioengineering Complex Microbial Communities

Presented by

Andrea Laura Kadilak, B.S., M.S.

Major Advisor _____
Leslie M. Shor

Associate Advisor _____
Ranjan Srivastava

Associate Advisor _____
Daniel Burkey

Associate Advisor _____
Kenneth Noll

Associate Advisor _____
George Bollas

University of Connecticut

2017

Acknowledgements

I would like to acknowledge financial support from NSF EFRI award 1137249 and fellowship support through NSF GK-12 award 0947869. I would also like to acknowledge support from the UConn CESE Graduate Assistantship and the UConn Graduate School Doctoral Dissertation Fellowship.

I would first like to thank my advisor, Dr. Leslie Shor. When I came to UConn during a campus visit for prospective graduate students and talked to her for the first time, her research projects and ideas made me realize she was someone I wanted to work with. Throughout my PhD, she has never let me settle for less than I was capable of, so I want to thank her for always pushing me to do my best. She has taught me to be a better writer, a better engineer, and a better steward of science to girls and other students who might not otherwise have opportunities to learn about scientific research.

I would also like to thank the rest of the members on my committee for their time, knowledge, and guidance: Dr. Daniel Burkey, Dr. George Bollas, Dr. Ranjan Srivastava, and Dr. Ken Noll. I would like to thank Dr. Burkey for introducing our lab to 3D-printing. Without that, I'm not sure what I would have pursued when my other microfabrication techniques weren't working. I would like to thank Dr. Bollas for teaching a great Computer Simulations class that I'm glad I took early in my graduate career. All of the knowledge I gained from him in that class has been so important to this project and I'm sure will still be useful to me many years from now. I would like to thank Dr. Srivastava for his support and especially his help in my getting a great job I'm very excited to start soon. I greatly appreciated all of his comments and ideas during the Termite Project meetings – I have really enjoyed working on a big, interdisciplinary project

where I can learn from and work with all sorts of other amazing scientists and engineers, and he has been a large part of that. I would also like to thank Dr. Noll, who is one of those great professors I was able to meet through the termite project. His opinions and thoughts as a biologist in a room of engineers have been invaluable, and on several occasions helped me to see my project from a different point of view.

I would also like to thank Reed Goodwin and Charles Bridges for their microbiologist consulting services. Thank you for both being a wealth of knowledge, and thank you to Charles in particular for your collaboration and all of your ideas and insights for my biocompatibility experiments. I would like to thank Dr. Kendra Maas at the MARS facility for all of your help with collecting my growth curve data. Thank you to Travis Omasta and Danielle Heichel for your help with ATR-FTIR readings and thank you to Dr. William Mustain and Dr. Kelly Burke for your suggestions and access to your students and equipment. I would like to thank Jeff Roth and Lhacene Adnane for all your help and friendly company in the clean room. I am also grateful for all of the advice, help, and support from Leah Winterberger, Susan Soucy, and Marita Decozio-Wiley.

I would like to thank all of my lab mates over the years, Dr. Jessica Furrer Chau, Dr. Jinzi Deng, Grant Bouchillon, Brian Cruz, and Yi-Syuan Guo. All of their support when I was stressed out or when experiments weren't working, their ideas when I was all out of my own, and our mutual love of board games and the Dairy Bar made our lab a fun and collaborative place. I am thankful for all of the wonderful, smart, and motivated undergraduates I've had a chance to work with, particularly Jess Rehaag, Cam Harrington, Haley MacPhee, Amanda Card, and Tom Kelly. This research would not have gotten done without all of their efforts. I'd also like to thank Dr. Dan Anastasio and Christine Endicott for the much-needed therapeutic lunches on some days

and for the fun lunches on all the other days. Coming in to work every day is much easier when you can look forward to seeing your friends there.

I would like to thank my parents, my brother, and the rest of my family for always telling me they were proud of me, and always encouraging me when I needed it most.

Lastly, I want to thank my boyfriend Sean. He has patiently looked at graphs and microscope pictures when I had a good research day and just had to show someone, and he has made me feel better about everything on the bad days. He has been there every time I wasn't sure I could do this, and he always told me I could. His love, patience, laughs, and support motivated me every step of the way towards this PhD.

Table of Contents

1 Overview

1.1 Motivation

Microfluidic, or lab-on-a-chip, devices encompass a quickly growing field of research devoted to the study of fluid behavior on the sub-millimeter size scale. These devices have a number of advantages over larger-scale analytical methods, such as smaller sample size required for analysis, high through-put capabilities, faithful reproduction of complex geometries, and ability to manipulate fluid flow in the laminar regime.

Another advantage of microfluidic techniques is the ability to accurately model devices using computational fluid dynamics (CFD) software, such as COMSOL Multiphysics. One main reason microfluidic devices lend themselves to CFD modeling is because, due to the very small size scale, the Reynold's number in flow systems is very low. Therefore, flow is well within the laminar regime, which is significantly easier to model and compute. Additionally, photolithography and soft lithography casting techniques used to fabricate microfluidic devices ensure a precise and consistent geometry. Again, this is a benefit in simulating the system because the geometry of a particular microfluidic design is uniform for all castings and experiments, and can be imported easily into the CFD software. Throughout this project, CFD modeling has been employed to better understand the electrochemical reaction kinetics, flow regimes, and diffusive transport within the various microdevices used.

Microfluidic technologies have been utilized in a variety of fields, but can be especially useful in biomedical and microbiological applications. Microfluidics are increasingly employed in cell culture applications because they can replicate a wider range of microenvironments experienced by cells than traditional bulk-volume culture techniques like agar plates and culture

flasks. Microfluidic techniques have been used to culture both prokaryotic and eukaryotic cells. Applications of prokaryotic, or bacterial, cell culture in microdevices include fermentation,[1] microbial fuel cells,[2, 3] chemotaxis studies,[4-6] and growth studies in complex structures, such as porous media.[6, 7] A wide variety of eukaryotic cell lines, including stem cells,[8] cancer cells,[9, 10] immune cells,[9] and epithelial cells[10] have been cultured in microfluidic devices. Additionally, microfluidic devices can be used to co-culture cell types that may be in close proximity in their natural microenvironment.[9-12]

However, many of the research groups that have developed these biological microfluidic applications are engineering groups with many years of expertise in the field. In order to successfully fabricate microfluidic devices such as these, researchers must possess in-depth knowledge of the complex photolithography patterning methods used and have access to the expensive clean room facilities and equipment needed for these techniques. While soft lithography casting methods used to make soft polymer molds do not require the same degree of experience or as extensive facilities, they still require a sizeable amount of laboratory space to create a designated dust free area or hood. Because of these hurdles, despite the many microfluidic devices and assays developed for biological applications, microfluidics have not replaced many of the more traditional assays or techniques used in the biological and medical fields. This is likely because many of these lab-on-a-chip technologies offer only minimal improvements over traditional methods, while being overly complicated for biologists to fabricate or use.[13]

Additive manufacturing, or 3D-printing, provides a possible solution to some of these difficulties in making micro- and millifluidic technologies more accessible. In recent years, the capabilities of 3D-printing have greatly improved while costs for desktop models has continued

to decrease; there are quality desktop 3D-printers available for as little as $2000-4000 at this point in time.[14, 15] With 3D-printing, small lab-on-chip devices can easily be designed in CAD software, or designs or device components downloaded from libraries available online.[14, 16] The piece can then be printed and ready for use in a matter of hours, using only a few dollars' worth of material. This can be compared to traditional photolithography and soft lithography methods, which require hundreds of thousands of dollars of equipment and infrastructure, the use of costly and dangerous chemicals, a high degree of hands-on time and expertise to fabricate, and it generally takes weeks to months to manufacture microfluidic devices made this way when all steps are included.

Already, many microfluidics researchers have begun implementing 3D-printing in the manufacture of slightly larger-scale, millifluidic, devices for a variety of applications.[14-24] Microreactors have been 3D-printed and tested for multiple organic and inorganic reactions, and have even been designed to incorporate in-line testing to monitor formation of reaction products in real-time.[19, 20] Since achieving adequate mixing in microfluidic flow regimes can sometimes be difficult in small devices with such low Reynold's numbers, researchers have used 3D-printing to develop efficient 3D mixing geometries. Some examples include complex corkscrew shapes and grooved surfaces, which would be either impossible or extremely difficult to fabricate using traditional photolithography masters and soft lithography casting methods.[19] Even more complex 3D-printed devices have incorporated printed pneumatic valves to control flow configurations and automate flow.[25]

Despite these advancements in implementing 3D-printing technology in millifluidic research, a number of important issues need to be addressed to enable more widespread use in biological applications. Some primary concerns for biological applications include the poor

optical clarity and questionable biocompatibility of available printing materials. If these issues can be investigated and resolved by either improvements to material formulation or developing treatments for specific polymers, the advantages will likely outweigh the disadvantages for incorporating 3D-printing into biological assays and research. Some researchers have begun using 3D-printing for microdevices with biological purposes, primarily cell separation and screening assays. Sensing and screening applications include a device to remotely detect *Staphylococcus aureus* bacterial cells in environmental samples[26] and a sensor developed to detect cell growth in response to antibiotic administration and other stimuli.[27, 28] A 3D-printed device to sort cells within a flow stream has also been created.[29] In each of these applications, however, cells are only in contact with the 3D-printed polymer for a short period of time, and therefore adverse biotoxicity effects are minimized or unimportant to the application.

To date, only a handful of systematic biocompatibility tests have been conducted on 3D-printed resins, and they have only been tested with zebrafish embryos as model organisms.[30-32] The size scale of 3D-printed millifluidics may make them particularly useful tools for cell culture experiments requiring replication of cellular structures or microenvironments. Millifluidic devices could be printed that put different cell types in contact with each other on the same scale that they would interact in nature, and require a much smaller volume of cells, as compared to traditional bulk liquid or plate culturing methods. Therefore, a main focus of this dissertation project has been adapting 3D-printed millifluidic devices for long-term cellular culture of bacteria, which had not yet been accomplished or documented in the literature. This work has incorporated extensively testing the biocompatibility of a widely-used printer resin and treatment methods to decrease the biotoxicity of that material, with a proof-of-concept long-term microbial culture in a 3D-printed device. The specific application for this microbial culture testing is as

part of a National Science Foundation-funded grant aiming to recreate the termite digestive tract in a lab-on-a-chip device to study the complex interactions of the microbial community inhabiting the termite gut in nature.

Creating a synthetic termite gut will require a number of engineering solutions. Termites are able to very efficiently digest lignocellulose, the material that makes up the cell wall of woody plant materials; they are able to break down 77-99% of the cellulose and 65-87% of the hemicellulose components of the lignocellulose.[33, 34] The reason termites are able to so efficiently break down these woody feedstocks is because of the diverse community of microbes inhabiting their hindguts; lower termite species in particular include members from the Protista, Bacteria, and Archea kingdoms.[35] These microbes work symbiotically with the termite and each other to chemically break down the lignocellulose into acetate and hydrogen, both chemicals that can be utilized in biofuel production.[33, 35] If the microbial community of the lower termite can be cultured outside of the termite gut, these microbes could be utilized in breaking down the millions of tons of lignocellulosic agricultural waste generated from woody plant materials yearly world-wide, providing a carbon-neutral method for hydrogen and natural gas production.[36]

Each organism performs a different role in the digestion process in the termite gut[35] and we hypothesize that proximity is important for the interactions between microbial symbionts. Therefore, in the artificial termite gut, these microbes must be provided with a chemical microenvironment on the same size scale as in their natural habitat in the hindgut (approximately 1 mm diameter). The microbial community also must be contained within the microhabitat that is constructed. To solve these problems, we have developed a system of in-plane hydrogel barriers constructed between the microhabitat and nutrient supply flow channel. These hydrogel barriers

will constrain microbes within the desired region of the device and prevent washout of the microbial community into the outflow channel, while still allowing diffusive transport of nutrients and oxygen to the microhabitat.

As a result of the metabolic reactions required to break down the lignocellulose and the microbes inhabiting it, the hindgut of the termite is a major oxygen sink, as seen in Figure 1-1. Generally, the aerobic symbionts live and consume oxygen within the first 200 μm (radially) of the 1 mm diameter hindgut, and the rest of the hindgut is comprised of anaerobic microbes that thrive in anoxic (oxygen depleted) conditions.[35, 37] Recreating this oxygen concentration profile poses a significant engineering problem in the construction of the microfluidic termite gut; it requires providing a very low and controlled amount of oxygen to be delivered to the microhabitat region of the device. We proposed doing this by using oxygen-producing microelectrodes that have been fabricated *in situ*, within the supply flow channel. In theory changes in the electrical current supplied to the microelectrodes and the channel flow rate could be used to finely tune the amount of oxygen generated and delivered to the microhabitat, respectively. Other researchers in our group have also investigated additional methods for the delivery of oxygen to the microhabitat, including tunable mixing of oxygen and nitrogen saturated supply streams.

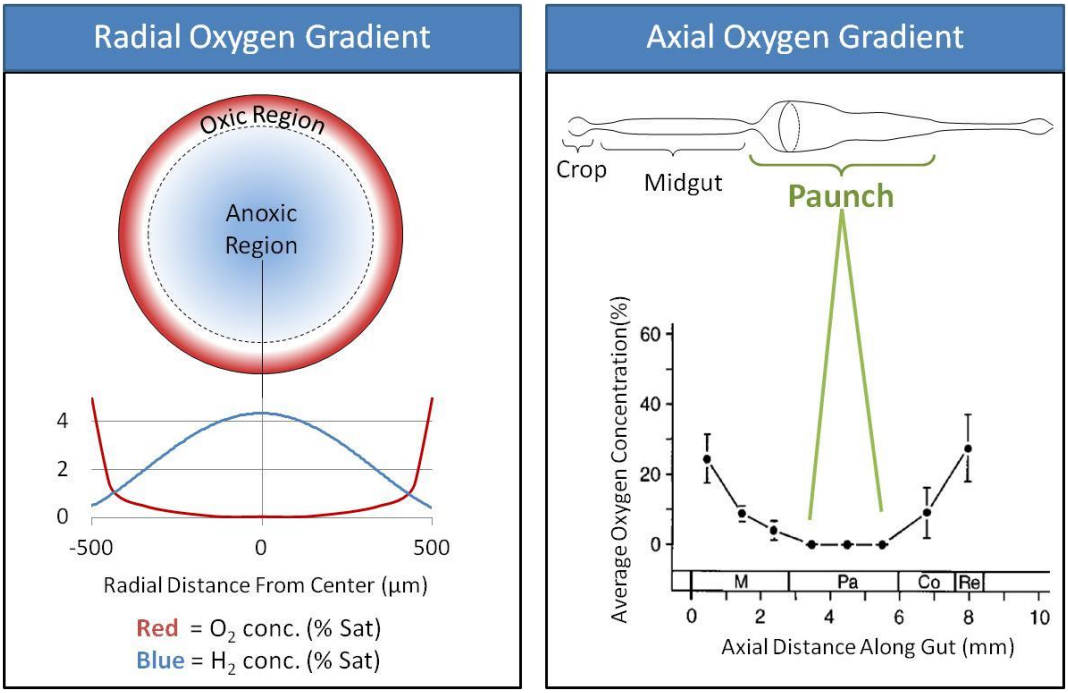

Figure 1-1: Diagram of radial and axial oxygen gradients in the hindgut of the lower termite *Reticulitermes flavipes*, adapted from Brune et al. [37]

1.2 Research Objectives

This work has focused on using advanced manufacturing techniques to enable microenvironment control of a microfluidic termite gut, incorporating a number of the points discussed in the Motivation section. The specific research objectives for this dissertation project are as follows:

1. Create a tunable oxygen delivery system to provide a slightly oxic gradient near the microenvironment boundary and an anoxic interior.
    a. Develop and optimize a method utilizing surface chemistry techniques to pattern gold microelectrodes *in situ* along the sidewalls within a microfluidic channel.
    b. Test the feasibility of these electrodes for generating a controlled concentration of oxygen within a microfluidic channel, for an eventual application of supplying the oxygen to cells within a culture device.

2. Investigate 3D-printing as a technology for fabricating a microdevices for long-term cell culture and use the knowledge gained to recommend methods for scaling up and accelerating manufacture of the hindgut-on-a-chip device.
    a. Employ rigorous biocompatibility testing of 3D-printed resin with bacteria cells, ranging from relatively robust cells to more sensitive strains, to help ensure success culturing the diverse termite microbial community in a 3D-printed device.
    b. Develop methods for improving the biocompatibility of 3D-printed resins for use in long-term contact with microbial cells.
3. Develop in-plane hydrogel barriers that both contain microbes and prevent wash out, while still allowing diffusive transport of oxygen, nutrients, and other important chemical species into the microhabitat.
    a. Design and fabricate a simple 3D-printed millifluidic device for cell culture that can be readily adapted for a variety of different cell types and communities.
    b. Develop a method to pattern hydrogel barriers *in situ* within 3D-printed channels.
    c. Characterize and simulate transport of tracer dye through hydrogel barriers so this information can be eventually used to calculate transport of oxygen, carbon substrates, and other important molecules to cells in the culture region of the device.
    d. Perform a proof-of-concept cell culture experiment in which a bacteria monoculture is grown inside a 3D-printed channel treated to improve biocompatibility and constructed with hydrogel barriers for substrate delivery.

The microfluidic and millifluidic systems described in this work will be used to further inform the study of the complex and dynamic interactions of the microbial community responsible for

efficient conversion of lignocellulose consumed by the termite. While these methods have been developed with the lab-on-chip termite gut as the immediate target application, the tools, techniques, and know-how created for this project will also be valuable to various small-scale cell culture applications in the broader microengineering, biotech, and biomedical research communities.

2 Selective deposition of chemically-bonded gold electrodes onto PDMS microchannel side walls[1]

2.1 Abstract

Many applications of microfluidic devices require the incorporation of electrodes. In this paper, we describe the simulation, fabrication, and performance of gold electrodes selectively deposited on the side walls of a microchannel. Electrode microfabrication methods typically pattern metal electrodes onto a flat substrate. However, when anode and cathode are both positioned on the bottom of a microfluidic channel, the electric field is not uniform with channel depth. Finite element modeling was used to characterize field distortion for conventional electrode placement versus side wall positioning for a range of microchannel geometries. These models showed that electrodes located on microchannel side walls created an electric field that was uniform with depth at all points within the channel, while electrodes deposited on the bottom substrate resulted in a 10-40% decrease in potential vertically along the microchannel side wall. This paper also demonstrates a new fabrication method to chemically bonded gold electrodes along opposing vertical side walls in a closed PDMS microchannel. Deposition of gold on the PDMS microchannel side walls was confirmed by SEM/EDX imaging and electrochemical analysis. Fabricated electrodes were electrochemically stable and resistant to shear.

[1] Published as: Kadilak, A. L.; Liu, Y.; Shrestha, S.; Bernard, J. R.; Mustain, W. E.; Shor, L. M., Selective deposition of chemically-bonded gold electrodes onto PDMS microchannel side walls. Journal of Electroanalytical Chemistry 2014, 727 (0), 141-147.

2.2 Introduction

Electrodes add functionality in many microfluidic applications. Microfluidic devices may incorporate electrodes for chemical or biological sensing,[38-44] for particle separations,[44-46] to drive electroosmotic flow,[47, 48] or for power generation in microfluidic fuel cells.[2, 3, 49-52] In a microfluidic system, electrodes must be fabricated to interface properly with other device features and functionalities. For example, electrode placement should not interfere with optical assays. Additionally, electrodes should be durably attached and materials often must be compatible with living cells and other reactive biological and chemical agents that pass through the device.

Gold is the most common material used in microfluidic electrodes due to its high electrical conductivity, chemical inertness, and good biocompatibility. Well-developed photolithography-based methods exist to pattern gold or other conductive materials onto flat surfaces, which can be used as the bottom substrate upon which microfluidic channels are bonded. The most commonly used techniques combine photolithograpy with either etching or lift off.[53, 54] In etching, the conductive material is deposited first, and then photoresist is applied on top and patterned, acting as a protective mask. Lift-off methods pattern the photoresist first and then use the photoresist as a stencil to pattern the metal. Additionally, surface modification via UV-initiated graft-polymerization and amination has been demonstrated to photopattern and chemically bond gold onto a flat polydimethyl siloxane (PDMS) substrate[55] and a flat polystyrene (PS) substrate.[44]

In the preceding examples, the electrodes are patterned on an open, flat surface. To incorporate such electrodes within a microfluidic device, the fluidic layer must be aligned with and bonded to the electrode-patterned substrate, which may be difficult to do with the required precision. Another important drawback to electrodes patterned on the bottom surface of the

channel is that the resulting electric field is not uniform with depth (Figure 1A). Thus, chemicals or cells experience different potentials at different depths in the microchannel, which can adversely affect performance in microfluidic applications such as electrophoretic separations.

In addition to photolithography combined with etching or lift-off, several other techniques have been used to incorporate electrodes in microfluidic devices. For example, silver wires have been introduced through guide channels, resulting in electrode wires laying along the bottom corners of the microfludic channels.[56] One possible difficulty with this approach is poor precision in the electrode placement, which can lead to misalignment with side walls, reduction in efficacy, and short-circuiting. Even if ideally positioned along the bottom corners of the channel, wire electrodes result in similarly distorted electric fields as pad-type electrodes (Figure 1B).

In contrast to the substrate-patterned and wire electrode examples discussed above, an ideal electrode configuration would result in a uniform potential gradient along the width and depth of the microfluidic channel. This ideal configuration can be achieved with electrodes fabricated along only the side walls of a microfluidic channel. Figure 1C illustrates the ideal electric field generated when electrodes are located along the vertical side walls of the microchannel, in contrast with the distorted electric field resulting from traditional pad or wire electrodes shown in Figures 1A and 1B. A more extensive theoretical basis and discussion on the advantages of side wall electrodes is provided in the Theory section.

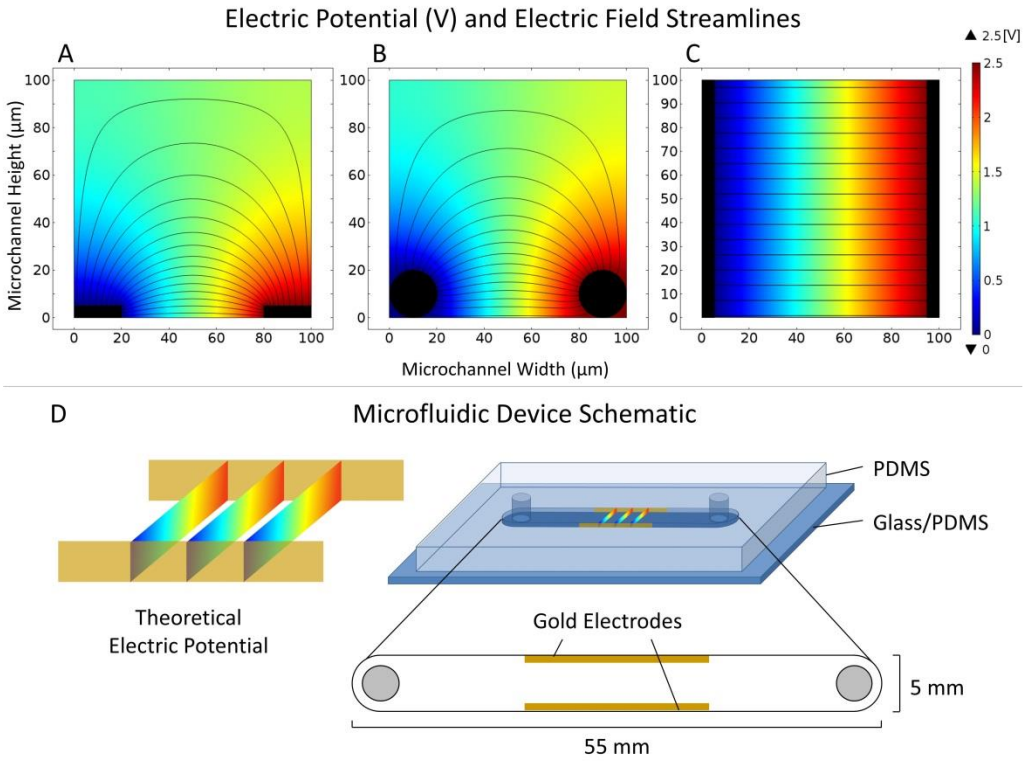

Figure 2-1. Panels A-C illustrate the potential (V) and electric field lines modeled using COMSOL Multiphysics 4.3b for a 100 × 100 µm cross-section of a microchannel where (A) represents electrode pads (5 × 20 µm), (B) represents wire electrodes (radius = 10 µm), and (C) represents an ideal, conformally-coated electrode on the side walls of the channel. Panel (D) is a schematic of the microfluidic device used in this paper (microchannel dimensions 5 mm wide × 55mm long × 100 µm high).

Other investigators have created electrodes along the inner surfaces of microfluidic channels. Mustin and Stoeber created electrodes in a microfluidic channel by casting PDMS devices with carbon black-rich patches.[57] In their report, electrodes were positioned within, not along the outer edge of, flow channels. Their method permits users without access to specialized microfabrication tools to implement a variety of 3D electrode geometries and to avoid alignment and bonding problems common for substrate-patterned pad electrodes. However, the conductivity of carbon black in PDMS is much lower than that of gold, especially at the low carbon black loadings needed for that method. Poor biocompatibility of carbon black may also be problematic for certain applications. In several reports, Arriaga and coworkers spray-coated a conductive "ink" along the side walls of millimeter-scale channels hot embossed into

poly(methyl methacrylate).[49-52] However, successful implementation of spray coating techniques into sealed microchannels may prove challenging. Further, realization of a working electrode requires additional microfabrication steps that may be difficult to implement inside a closed microfluidic channel. Finally, spray-coating may not be as resistant to shear as chemically-bonding gold uniformly on the interior side walls of a microdevice.

In this paper, we demonstrate a new method to create chemically bonded gold electrodes along vertical side walls of a PDMS microchannel (Figure 1D). PDMS is one of the most commonly used materials for biological applications of microfluidic devices because it is optically transparent, biocompatible, and is permeable to oxygen and carbon dioxide. Surface-directed graft polymerization and further surface chemistry modification to deposit gold on PDMS has been previously described by Hao et al.,[55] who patterned gold on a flat PDMS substrate. We describe a method to fabricate and pattern gold electrodes inside a closed PDMS microchannel. In this fabrication procedure, photopatterning initiated the selective formation of the gold electrode layer along only the side walls of the closed microfluidic channel. The presence of gold on the microchannel side walls was verified using SEM/EDX. The gold-patterned side walls functioned as electrodes as demonstrated by cyclic voltammetry performed both before and after gold deposition, and before and after shear resistance testing. This method relies on photolithography equipment, materials, and techniques that are already in wide use in microfabrication labs, making it readily adaptable to various microfluidic applications.

2.3 Materials and Methods

2.3.1 Chemicals

Sylgard 184 silicone elastomer kit (PDMS) was purchased from Dow Corning (Midland, MI). SU-8 2100 photoresist and SU-8 developer were obtained from Microchem (Newton, MA).

Benzophenone (99%), Acrylic acid (99%), ethylenediamine (≥ 99.5%), and N-(3-dimethylaminopropyl)-N′-ethylcarbodiimide hydrochloride (≥ 99.0%) were purchased from Sigma-Aldrich. Gold (III) chloride trihydrate, sodium sulfite, sodium thiosulfate (≥ 98.0%), potassium thiocyanate, ascorbic acid (99%), and sodium borohydride (≥ 98%) were purchased from Fisher Scientific. All chemicals were used as received. The electrical connects were conducting composites comprised of PDMS mixed with carbon black (CB) (Carbon black, Vulcan XC72-R, Cabot Corporation) and hexane (≥ 95%, Sigma-Aldrich). Deionized (DI) water (resistivity ≥ 18.2 MΩ cm) was produced from a Direct-Q 3 UV Millipore ultrapure water system.

2.3.2 Preparation of Microfluidic Flow Cell

A schematic for the microfluidic device described in this paper is presented in Figure 1D. The dimensions of the channel were 5 mm wide by 55 mm long and the height measured 96 ± 13 μm (Dektak surface profilometer Model 150, Veeco Instruments, Plainview NY). The channel contained two rows of posts measuring 200 μm in diameter. Microfluidic masters were created from SU-8 2100 (Microchem, Newton, MA) using photolithography as previously described.[58] Detailed fabrication parameters can be found in Table S-1. Mylar photomasks were purchased from Advanced Reproduction (Andover, MA) and silicon wafers from Nova Electronic Materials (test grade, Flower Mound, TX).

Replicate devices were cast from masters in PDMS using standard soft lithography methods.[59] Briefly, a 10:1 mixture of PDMS polymer base and curing agent was fully mixed, de-gassed, then poured over the masters and cured in place for 4 h at 60°C. Castings were peeled away from the master, access ports were punched with a biopsy punch, and each device was irreversibly bonded to either a glass microscope slide or a thin slab of PDMS by exposing both

surfaces to oxygen plasma (Plasma Cleaner model PDC-32G, Harrick Plasma, Ithaca, NY) for 30 s or 45 s, respectively. Deionized water was immediately added to the microchannel to maintain the hydrophilicity of the PDMS.[60]

2.3.3 Deposition of Carbon Black-PDMS Electrical Connects

To enable electrochemical characterization of the gold side wall electrodes, non-gold leads were needed to connect side wall electrodes with an external power source. Electrical connects comprised of a conductive CB-PDMS composite were fabricated on the substrate prior to microfluidic flow cell assembly. First, 0.2 g PDMS base, 0.02 g curing agent, 0.1 g CB, and 1 ml hexane were combined in a sealed glass vial containing a micro stir bar. Mixing was achieved by alternating 15 min of micromagnetic stirring with 15 min sonication. The CB-PDMS electrical connects were then patterned using a spray gun (Badger Air-Brush Co., Franklin Park, IL) to deposit the CB-PDMS over a masked glass substrate which was then cured for 4 h at 60°C. Before further treatment, the substrate was rinsed with isopropanol and dried with N_2 gas to remove impurities. The conductivity of this CB-PDMS layer averaged 40 ± 2 S m^{-1}.

To facilitate bonding the microfluidic flow cell to the CB-PDMS connects, a thin PDMS coating was spray-coated over most of the conducting strips by masking and spraying as before. The extreme inner edges of the CB-PDMS electrodes were masked prior to depositing the PDMS coating to ensure electrical contact with gold side wall electrodes in the completed device. The PDMS coating was comprised of a uniform mixture of 0.1 g PDMS base, 0.01 g curing agent, and 0.5 ml hexane. The PDMS coating was partially cured at room temperature for approximately 3 h prior to final assembly of the microfluidic device.

2.3.4 Fabrication of Gold Side Wall Electrodes

The selective deposition of chemically-bonded gold electrodes on the side walls of the PDMS device required several steps. The UV-induced graft polymerization of acrylic acid (AA) to polyacrylic acid (PAA) in the presence of the photoinitiator, benzophenone (BP), absorbed in PDMS was originally developed by the Allbritton[61, 62] and Tabeling[63, 64] groups, who established process parameters required for successful polymerization within a PDMS microchannel. Hao et al.[55] developed a method to combine this chemistry with amination and growth steps to photopattern a gold film on a flat PDMS substrate. The procedure described here combined and adapted these previous methods to a flowing system inside a PDMS microfluidic channel.

A custom photomask was used to selectively initiate graft polymerization of AA to PAA in the presence of BP, the photoinitiator. Prior to photopatterning, a solution of BP in acetone was flowed through the microchannel; the acetone solvent causes slight swelling in the PDMS device, allowing the BP to move into the cross-linked polymer network. Any remaining acetone was evaporated and then the channel was loaded with a de-aerated AA solution. At this point, the AA in the microchannel was only in contact with the BP photoinitiator at the interior PDMS channel surface. Photopatterning was achieved by aligning transparent regions of the photomask with the side walls of the filled PDMS microchannel. After polymerization, the PAA was surface-functionalized with an amine group to allow for the attachment of a gold seed layer. The final gold electrodes were then grown by electroless deposition. A schematic of the overall protocol is presented in Figure 2. Table S-2 lists the chemicals, concentrations, flow rates, and additional process parameters for each step including grafting of PAA, preparation of PAA graft for gold deposition, and formation of gold electrodes. Each step of the process is described in detail in the Supplemental Information.

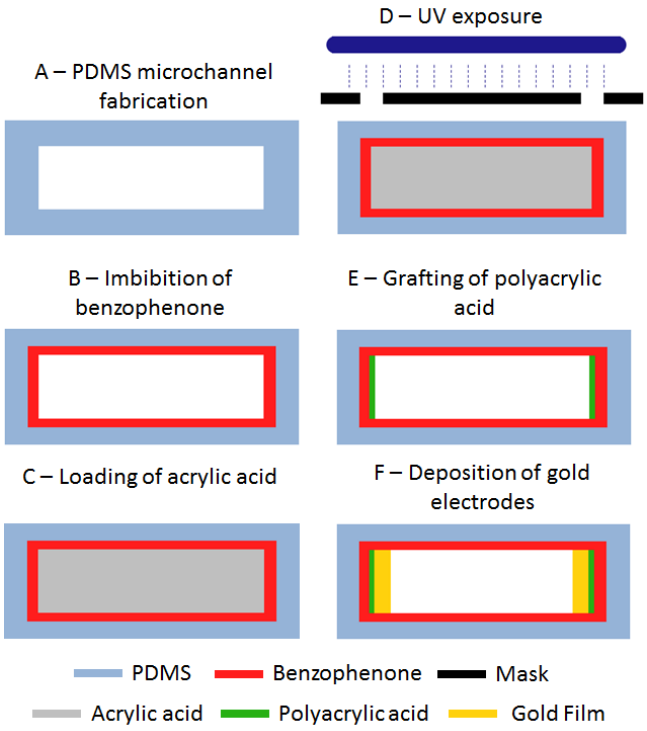

Figure 2-2. Schematic of fabrication of gold electrodes on the side walls of a PDMS microchannel. Each panel depicts a cross-section of the microfluidic channel, where into the page is in the direction of flow through the channel. (A) Initial cross-section of a PDMS microchannel (Light blue). (B) PDMS microchannel imbibed with benzophenone (Red). (C) The microchannel filled with acrylic acid (Gray). (D) Region-selective UV exposure (Blue) along the side walls only using a photomask (Black). (E) Polyacrylic acid (Green) grafted on the side walls. (F) Formation of gold film (Yellow) on the side walls after amination, nucleation, and growth of the gold film.

2.3.5 Confirming PDMS Surface Modification with ATR-FTIR

Polymerization of PAA along the PDMS side walls and surface chemistry modifications after the amination step were confirmed using attenuated total reflectance Fourier transform infrared (ATR-FTIR) spectroscopy (iS10 spectrometer, Thermo Scientific).

2.3.6 Confirming Gold Deposition with SEM/EDX

The Au layer formed along the PDMS microchannel side walls could be observed directly and was further characterized using a JEOL JSM-6330F scanning electron microscope (SEM) equipped with Thermo Noran System Six energy-dispersive X-ray spectroscopy (EDX) system. A thin transverse section of the coated microchannel was sectioned using a razor blade,

placed on a glass microscope coverslip, sputtered with carbon using an Edwards 306A vacuum evaporator, and then imaged.

2.3.7 Electrochemical Characterization of the PDMS Microdevice

All electrochemical experiments were carried out in N_2-saturated 0.1 M $HClO_4$ at room temperature using an Autolab PGSTAT302N potentiostat. The PDMS microdevice was connected to the potentiostat by two electrical clips connected to the CB-PDMS conducting strips. At least 5 cyclic voltammograms (CVs) were run between -2.0-2.0 V at 100 mV/s to condition the Au electrodes prior to data collection.

2.4 Theoretical Basis and Simulation of Electrode Performance

Steady-state electric fields within a microfluidic channel were simulated in COMSOL Multiphysics 4.3b using the Electrostatics physics package. Electrodes were modeled along the channel substrate in a configuration typical for microfabricated pad electrodes (20 × 5 μm, Figure 1A), wall-aligned wire electrodes (10 μm radius, Figure 1B), or as the ideal side wall configuration proposed here (5 × 100 μm, Figure 1C). For all simulations, the 2-D cross-section of the flow channel was modeled as a rectangle with a height of 100 μm. Simulations were conducted with four aspect ratios of height to width: 1:1, 1:2, 1:5, and 1:10; these ratios corresponded to microchannel widths of 100, 200, 500, and 1000 μm in the simulation. The device was assumed to be electrically insulated, and the microchannel was filled with water with an isotropic relative permittivity of 80. The potential difference between the two electrodes was 2.5 V in all simulations. For each aspect ratio and electrode configuration, the potential was evaluated as a function of height within the channel at various distances from the vertical side wall of the device: at the wall and at distances 10%, 20%, and 50% of the total channel width away from the wall.

Finite element simulations for the four aspect ratios clearly illustrated the advantages of electrodes located along the vertical side walls compared with electrodes located on the bottom surface. For microchannels in which the electrodes were located on the side walls, the potential was constant along the vertical axis (Figure 3). For ideal side wall electrodes, the magnitude of the potential at different positions across the channel differed slightly for different aspect ratios since the electric field in water is not perfectly linear. However, for microchannels with 5 × 20 μm pad and 10 μm radius wire electrodes, there were large variations in the potential along the vertical axis at nearly all distances from the wall. A sizeable reduction in potential along the side wall edge opposite a substrate-bonded electrode was observed for these electrode configurations. As shown in Figure 3, the variation in the electric field was greatest in microchannels with smaller aspect ratios (i.e., 1:1, and 1:2), and was greatest near the side walls. For example, in channels with a 1:1 aspect ratio, there was approximately a 45% reduction in potential along a vertical transect located 20 μm (20% transect) from the side of the 100 μm channel. Similarly, in channels with a 1:2 aspect ratio, there was approximately a 30% reduction in potential along a vertical transect located 20 μm (10% transect) from the side wall of the 200 μm channel. As the aspect ratio of the channel increased, the middle of the channel exhibited behavior closer to that of the ideal side wall deposited electrodes.

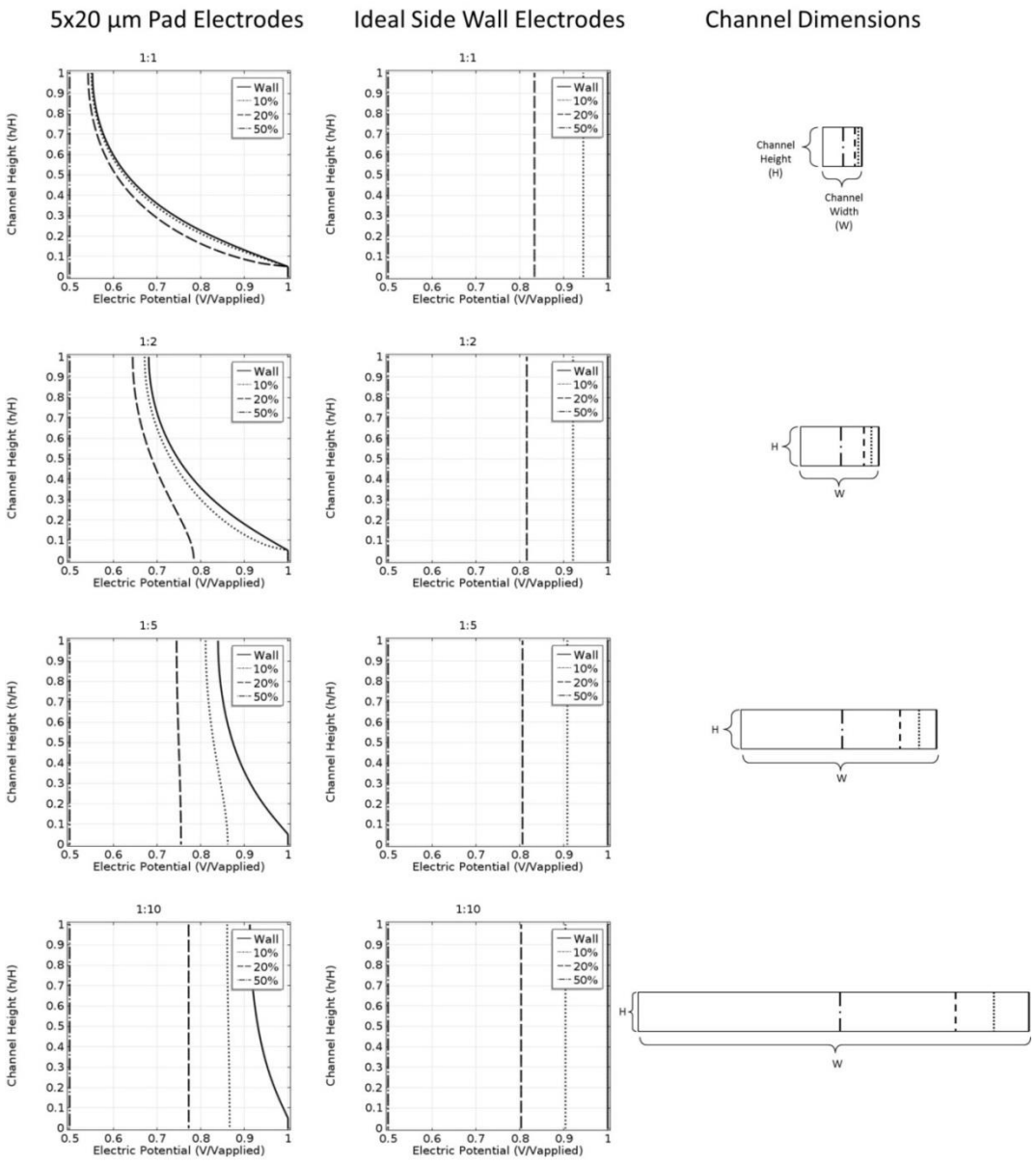

Figure 2-3. Electric potential along vertical transects of microchannels with aspect ratios (h:w) of 1:1, 1:2, 1:5, and 1:10 modeled in COMSOL Multiphysics 4.3b. Transects are located at the right side wall and distances 10, 20, and 50% of the total channel width from the wall, as illustrated on the right. For example, for a 100 µm wide channel, transects would be 10, 20, and 50 µm from the wall. These plots illustrate the disturbance in the potential in the vertical direction for pad electrodes deposited on the substrate on the bottom surface of the microchannel compared to the stability of the electrodes deposited on the side walls of the channel.

However, even in higher aspect ratio channels (i.e., 1:5 and 1:10), vertical inhomogeneity of the electric field could be observed 50 µm or more from the side wall for pad-type electrodes; this number is significant when compared to the size of microscopic species that may be

observed, separated, or otherwise subjected to the electric field. Thus, in a real device with pad or wire electrodes, the potential experienced by cells, ions or any other species, particularly those located near the side walls, could differ substantially with height within the microchannel. In contrast, electrodes positioned along the vertical side walls of a microfluidic channel result in a vertically consistent electric field, regardless of microchannel dimensions or position along the microchannel width. Vertical homogeneity in the electric field will allow for microfluidic devices with enhanced separations efficiency, more sensitive electrochemical sensing capabilities, and more uniform electro-osmotic flow.

One possible method for experimentally validating the vertical uniformity of the electrical field is by imaging the response of charged fluorescent tracers while applying a current to the electrodes.[65] Using a confocal microscope, one could image the distribution of the tracers in the channel at different points along the vertical axis for the two different electrode configurations (side wall vs. pad electrodes).

2.5 Results and Discussion

2.5.1 Confirmation of PDMS Surface Functionalization and Gold Deposition

ATR-FTIR spectra were collected on disassembled PDMS microchannels at interim steps of the side wall electrode fabrication and were compared with untreated samples. Results are shown in Figure S-2. The polymerization of AA to PAA after exposure to UV was shown by the broadening of the peak near 3000 cm^{-1}, which is indicative of carboxyl (-COOH) stretching. The sharp peak at 1700 cm^{-1} was consistent with carbonyl (-C=O) stretching. Both features were absent from the bare PDMS and UV-exposed untreated PDMS, confirming the formation of PAA in the treated sample. Peaks due to carbonyl stretching in an amide group were evident at 1550 cm^{-1} after amination. In addition, the broad peak at 3200 cm^{-1} was assigned to N-H

stretching. ATR-FTIR showed that the described procedure successfully functionalized the PDMS surface with amine groups.

The formation of the Au seed layer was visually apparent as dark lines along the sides of the microchannel (Figure S-3). Minimal deposition was observed on the substrate or the top of the microchannel. The localization along the side walls showed site-selective deposition of Au. Selective deposition of Au along the microchannel side wall was confirmed by SEM images and EDX of microchannel cross-sections (Figures 4 and S-3). A slight curvature in the PDMS side wall could be observed in the SEM image, and was likely an artifact from the cross-sectioning procedure or possibly caused by a slight vertical slant in the master mold for the microfluidic device. In the SEM image, the Au film could be clearly seen as a bright lining along the side wall of the microchannel. The presence of Au in this location was verified using EDX elemental mapping. As can be seen in Figure 4, silicon (Si) that makes up a portion of the PDMS polymer backbone was distributed throughout the entire microfluidic channel, as expected. Furthermore, the elemental mapping verified that the bright lining in the SEM image was not merely an edge effect, but was indeed an Au film, selectively deposited only along the vertical side wall (Figure 4). The measured thickness of the film was approximately 4 μm and consistent over the height of the channel in multiple cross-sections sampled from multiple devices. The electric field was modeled considering various possible defects in the side wall electrodes, including surface roughness, slanted electrodes, and electrodes with over-patterning on the channel top and bottom; even with these defects, the side wall electrodes demonstrated a uniform electric field compared to pad and wire electrodes (Figure S-4).

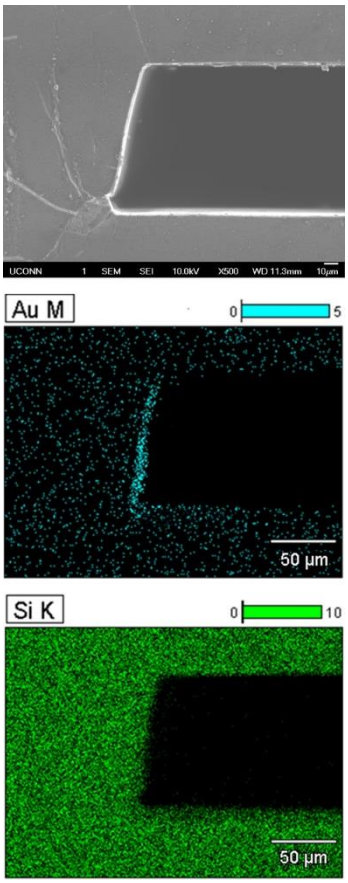

Figure 2-4. SEM image and EDX mapping showing a cross-section of a PDMS microchannel with the gold film deposited selectively at the side walls.

2.5.2 Electrochemical Characterization of the PDMS Microdevice

The electrochemical responses of the PDMS microdevices with and without deposited Au on the side walls were measured under flow of 0.1 M N_2-saturated $HClO_4$. Figure 5 shows cyclic voltammograms of freshly-prepared PDMS microdevices without (black) and with gold electrodes on the inner side walls (red). For electrodes without deposited Au, only a very small capacitive current was observed with a small amount of oxygen evolution starting around 1.5 V. This very small current was due to the presence of exposed carbon from the CB-PDMS connects. For microdevices with Au side wall electrodes, there were two obvious changes in the voltammogram. First, the capacitive current was increased, suggesting that the deposited Au had a high surface area, which was observed with the SEM images in Figure 4. The second

significant change in the voltammogram was a decrease in the onset potential for oxygen evolution to approximately 1.1V, confirming the activity of the deposited Au. One interesting aspect of the recorded CVs was the lack of characteristic oxidation peaks that are commonly observed for polycrystalline Au, which shows that the deposited Au was active despite being poorly crystallized.

To determine the physical stability of the deposited Au layer and its resistance to shear, DI water was flowed through the channel at 200 µL min^{-1} for 10 h. The cyclic voltammogram of the post-sheared device is shown as the blue curve in Figure 5, which is nearly the same as the freshly-prepared device (red).This showed that the chemically-bonded Au side wall electrodes were stable in the presence of shear.

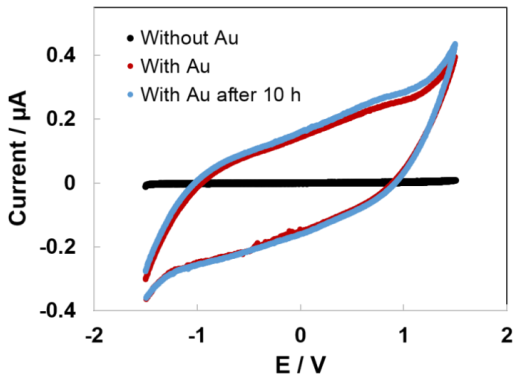

Figure 2-5. Cyclic voltammograms of the PDMS microdevice with CB-PDMS electrical connects but without gold side wall electrodes (black), with gold side wall electrodes (red), and with gold side wall electrodes after 10 h shear test (blue) in flowing 0.1 M N_2-saturated $HClO_4$. The scan rate used during cyclic voltammograms was 20 mV s^{-1} and the flow rate used for the shear test was 200 µL/min.

2.6 Conclusion

In this report, a method is described to fabricate chemically-bonded Au electrodes along only the side walls of a PMDS microfluidic device. CB-PDMS electrical contacts were used to connect the electrodes to the external circuit. We showed that the electrodes were electrochemically active and resistant to shear. Computer simulations proved that side wall

electrodes prevent the vertical inhomogeneity of the electric field that occurs with substrate-patterned electrodes. The homogeneous electric field enabled by the reported sidewalls can increase the sensitivity of microfluidic separations and enable more electroosmotic separations. These electrodes may also be beneficial for microfluidic fuel cells and electrosynthesis.

Certain limitations to this method exist, including the large size of the microchannel used. Such a wide channel was used to facilitate manual alignment of the photomask in the PAA photopolymerizing step, but is not representative of the scale used in many microfluiudic applications. Additionally, the lack of precision in the spray coating method used to deposit the CB electrical connects led to occasional issues in microchannel bonding and alignment. Future work will focus on refining the procedure for improved precision in smaller microfluidic channels; implementing photopatterned Au electrical connects for improved performance, biocompatibility, and streamlined assembly; and application-specific evaluation.

2.7 Supplemental Information

2.7.1 Detailed Electrode Fabrication Protocol

2.7.1.1 UV-initiated Selective Grafting of PAA

In the first step of the protocol, a solution of 10 wt % BP in acetone was flowed through the PDMS microchannel to prime the surface for graft polymerization. Imbibition of hydrophobic BP was enhanced by the polymer swelling that occurred in the presence of acetone. After the BP solution was flowed through the microchannel for 10 min, the acetone was removed from the channel and interstitial spaces in the polymer by pumping air through the channel, followed by vacuum treatment at -15 kPa for 10 min.

BP is a type-II photoinitiator and forms a triplet state upon excitation by UV light, which can be relaxed by abstracting a hydrogen atom from the AA monomer. Abstraction of hydrogen from AA generates AA radicals, which undergo rapid polymerization to form PAA. The UV-induced graft polymerization of AA to PAA in the presence of BP absorbed in PDMS was originally developed by the Allbritton[61, 62] and Tabeling[63, 64] groups, who established process parameters required for successful polymerization. Hao et al.[55] developed a method to combine this chemistry with amination and growth steps to photopattern a gold film on a PDMS substrate

Oxygen has been shown to inhibit the abstraction of hydrogen by the triplet state of BP,[66, 67] and PDMS is known to be permeable to oxygen.[68] However, this inhibition by oxygen can be overcome by deaerating the reaction precursors and allowing sufficient time for BP to permeate the PDMS walls.[64] BP quenches the oxygen present in the PDMS and helps to prevent oxygen from reaching the channel walls. Therefore, it is important to form a homogeneous layer of BP deeply absorbed into the PDMS polymer to act as an oxygen barrier. Atmospheric oxygen also inhibits the graft polymerization of PAA by reacting with the propagating radical of AA,

reducing the number of reactive radicals that are formed.[69] Here, oxygen was removed from the AA by placing the solution under vacuum at -15 kPa for a minimum of 1 h. As received AA had 180-200 ppm of hydroquinone monomethyl ether (MEHQ) to inhibit autopolymerization. However, MEHQ does not inhibit polymerization if oxygen is not present.[69] Therefore, it was not necessary to further purify the AA once the oxygen was removed.

Following the BP treatment and subsequent drying, the microchannel was loaded with a solution of the deaerated 20 wt % AA in water and the inlets were sealed with tape to further prevent exposure to air. Although BP in the PDMS matrix serves to scavenge excess oxygen, continued diffusion of BP into the PDMS matrix tends to decrease the concentration of BP at the surface, impacting subsequent graft polymerization.[63] As a result, the elapsed time between priming surfaces with BP and exposure to UV is important. Here, the side walls of the device were exposed to UV light within 30 min of BP priming. A custom Mylar photomask placed in a mask aligner was used to expose the side walls to 365 nm UV light at 40 mW cm^{-2} for 5 min. After UV exposure, the microchannel was flushed with ethanol and then water for 1 and 2 h, respectively, to remove unreacted AA.

2.7.1.2 Surface Functionalization and Gold Seeding Layer

Amine-functionalized surfaces are well-known for their ability to seed layers of gold nanoparticles.[70] Therefore, the next step in the process focused on converting the (-COOH) terminated PAA to a surface that was terminated with (-$CONH_2$) groups. The PAA graft was treated with 0.36 M ethylenediamine (EDA) in the presence of 50 mM N-(3-dimethylaminopropyl)-N′-ethylcarbodiimide hydrochloride (EDC). EDA was attached to the PAA through the formation of an amide linkage. Specifically, EDC activated the carboxylic (-COOH) group of AA to form an amide (-C(O)NH-) linkage with the amine (-NH_2) group of EDA.

Next, a gold seed layer was deposited on EDA by flowing 1 mM aqueous gold (III) chloride trihydrate adjusted to a pH of 3.5 with NaOH. The Au (III) ions were reduced with 0.1 M sodium borohydride. Here, Au (III) attached to the amine end of the linked EDA, most likely due to delocalization of N electrons in the amine group. After reduction of these Au (III) ions by sodium borohydride, the resulting nanoparticles acted as nucleation sites for growth of Au films in electroless deposition. Lastly, the microchannel was treated with 0.5 M KSCN to remove non-specifically formed oligomeric Au (III) chloro-hydroxy species that could result in over-plating upon reduction. After each chemical treatment, the microchannel was washed with DI water for 10 min at a flow rate of 200 μL min^{-1}.

2.7.1.3 Deposition of Contiguous Au Electrodes

Contiguous Au films were formed on the side walls of the microchannel by electroless gold deposition. A gold bath solution consisting of 0.01 M of gold (III) chloride trihydrate, 0.1 M of sodium sulfite, 0.1 M of sodium thiosulfate, 0.1 M of potassium thiocyanate, and 0.1 M of ascorbic acid was prepared and adjusted to pH 6.0 with NaOH. The solution was then heated to 50 °C and flowed through the microchannel for 1 h. After washing with DI water, the microfluidic device was dried in air at room temperature.

Table S2-1. Microfluidic master fabrication parameters.

Fabrication Step	**Process Details**
Spincoating Photoresist	Spincoat SU-8 2100 Photoresist at 2000 RPM for 35s
Pre-baking	Bake on hot plate at 65°C for 1 h, then 95°C for 3 h
UV Exposure	Expose to UV at intensity of 40 mW cm^{-2} for 6.0 s
Post-baking	Bake on hot plate at 95°C for 10 min, cool at 23°C for 20 min
Developing	Immerse in SU-8 Developer for 20 min with gentle agitation
Cleaning	Clean wafer with isopropanol, then dry with ultrapure N_2

Table S2-2. Concentration of chemicals with their flow rate and duration of flow during the grafting of poly(acrylic acid) (PAA), amination of PAA, nucleation with gold monolayer, and growth of gold electrodes. All concentrations listed are for solutions in DI water unless otherwise noted.

Chemical	**Concentration**	**Flow rate (µL/min)**	**Duration (min)**
Benzophenone (BP)	10 wt % in acetone	200	5
Acrylic acid (AA)	20 wt %	0	0
Ethylene diamine (EDA)	0.36 M	200	60
Gold (III) chloride trihydrate	1 mM	200	60
Sodium borohydride	0.1 M	200	5
Potassium thiocyanate	0.5 M	20	18 h
Gold (III) chloride trihydrate	0.01 M	200	60

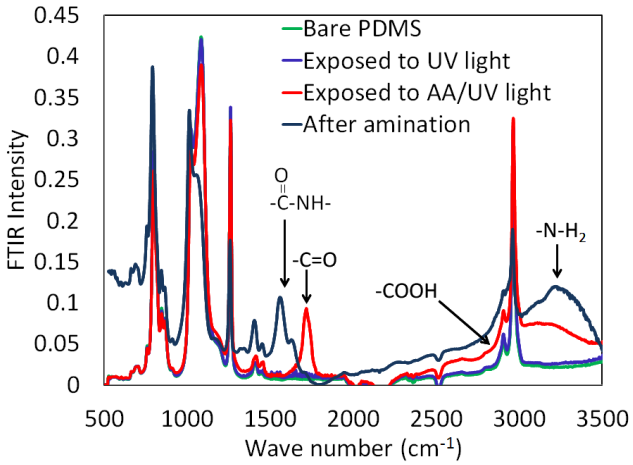

Figure 2-6 (S2-1). ATR-FTIR spectra of PDMS surface after different treatments. Spectra were taken from 500 to 3500 cm^{-1} at a resolution of 4 cm^{-1}. Peaks for carboxylic group were absent on bare PDMS and bare PDMS exposed to UV light. After grafting of polyacrylic acid, peaks due to stretching in carboxyl acid could be clearly observed. These peaks due to stretching in carboxylic acid disappear and peaks indicating carbonyl stretching in the amide bond and N-H stretching appear following amination.

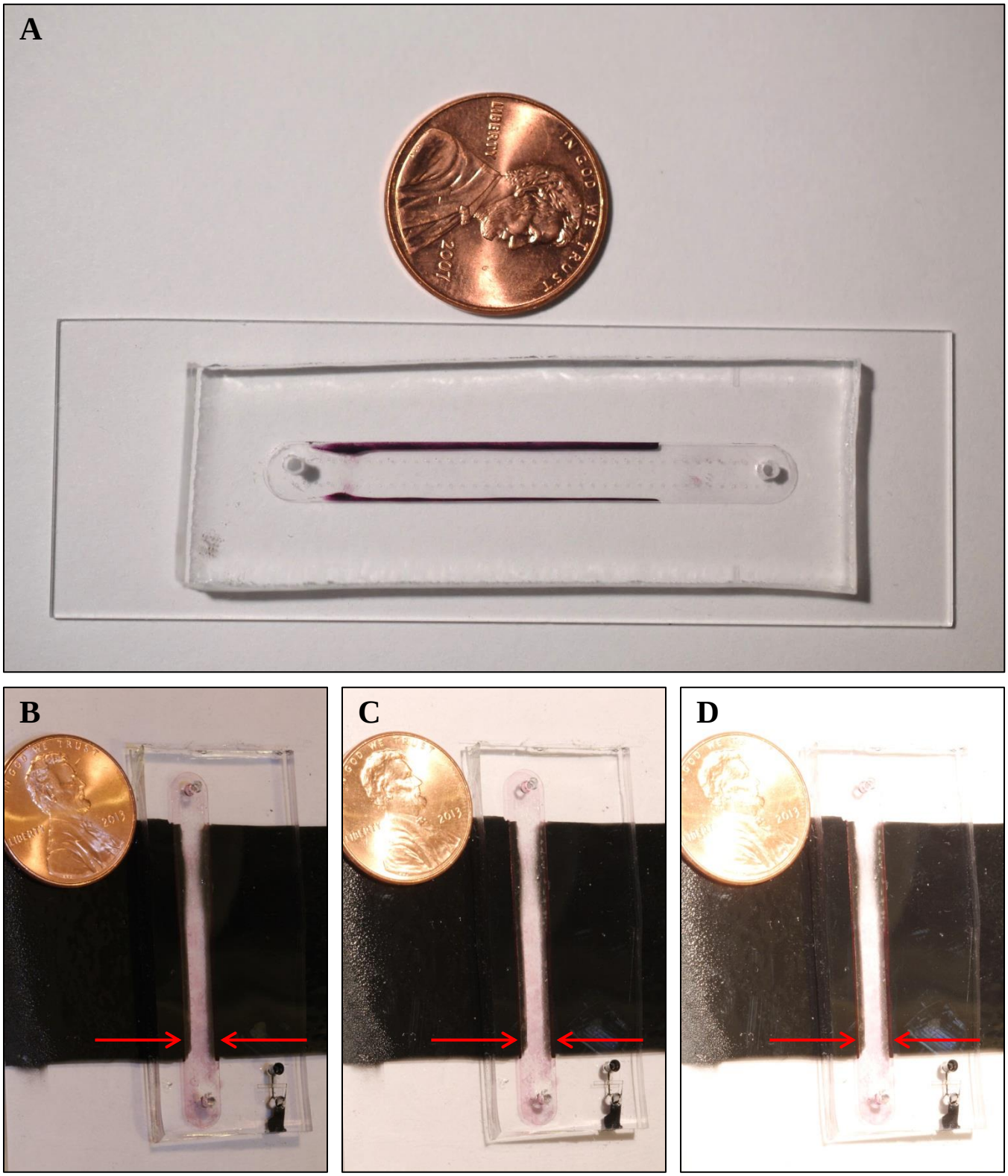

Figure 2-7 (S2-2). A: photograph of a PDMS microfluidic device with gold (dark lines) deposited on the sidewalls of the microchannel. B-D: photographs of a PDMS microfluidic device with CB-PDMS electrical connects and gold deposited on the sidewalls of the microchannel; exposure was increased with each photograph to make the gold electrodes more easily visible.

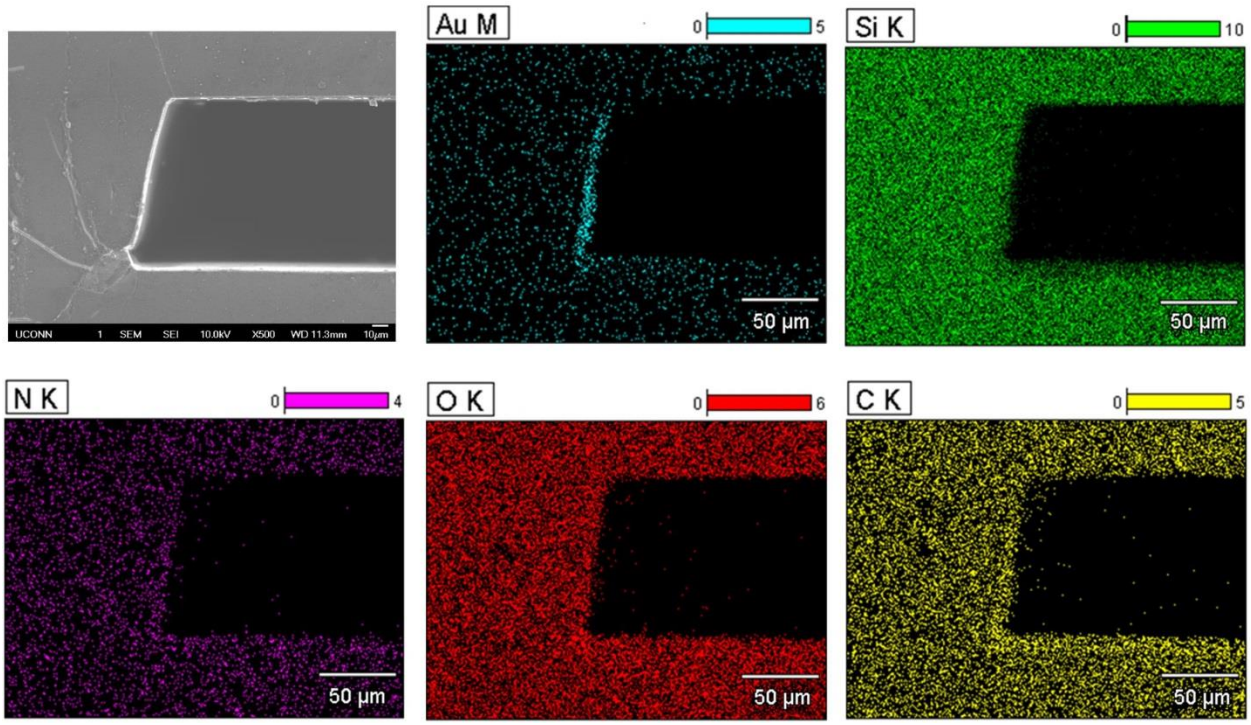

Figure 2-8 (S2-3). SEM image showing a cross-section of a PDMS microchannel with the gold film deposited selectively at the side walls. The SEM/EDX elemental mapping was done at 10 kV for 10 min.

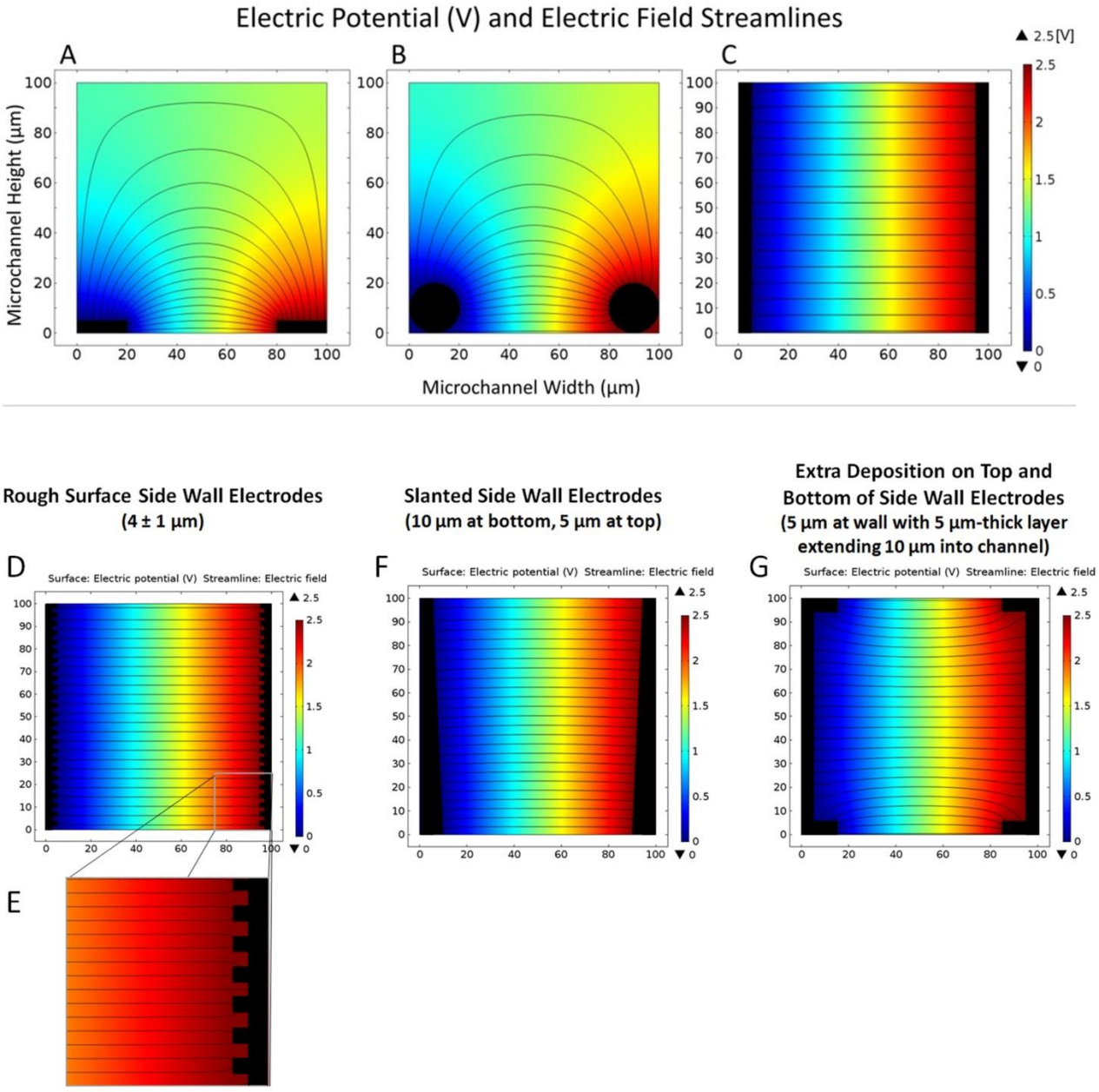

Figure 2-9 (S2-4). Top, **Panels A-C:** electric potential (V) and electric field lines for different ideal electrode configurations simulated using COMSOL Multiphysics 4.3b (as shown in the manuscript, in Figure 1). For comparison, electric potential (V) and electric field lines for side wall electrodes with various geometrical defects. **Panel D:** saw tooth-patterned surface with 4 ±1 □m surface roughness with detail (**Panel E**) to show how field lines emanate from the rough surface. **Panel F**: slanted side wall electrode with smooth variation in electrode thickness from 5 to 10 μm. **Panel G:** "C"-shaped electrode with over-patterning along channel top and bottom.

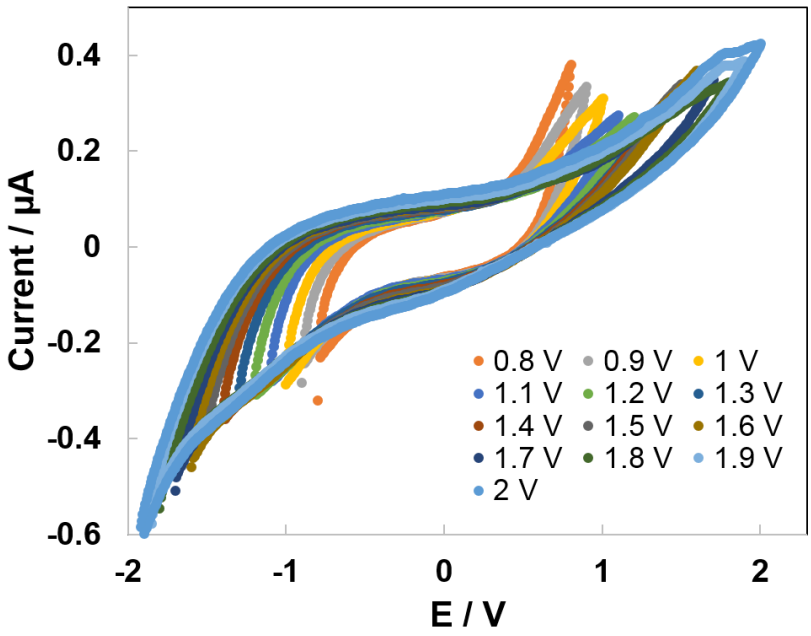

Figure 2-10 (S2-5). Window opening experiments to show the oxygen evolution onset voltage in the microdevice. Shown are cyclic voltammetry curves for freshly-prepared PDMS microdevice with gold side wall electrodes under window opening potentials ranging from 0.8 V to 2.0 V in 0.1 M N_2-saturated $HClO_4$ flow. A scan rate of 20 mV s^{-1} was used. Based on this plot, 1.5V was selected for the voltammetry work shown in the main document Figure 5.

3 Methods to Quantify and Improve Microbial Biocompatibility of Stereolithography 3D-Printed Resin[2]

3.1 Abstract:

In recent years, improving capabilities of 3D-printing have made it a viable option for quickly and cheaply manufacturing micro- and millifluidic channels with complex, enclosed geometries. Stereolithography (STL) printers work by cross-linking photoactive polymers using high intensity lasers and are able to achieve resolutions on the order of tens to hundreds of microns. However, biocompatibility of STL 3D-printed resins may limit adoption of the material, especially for cell culture applications. This paper describes resin treatment methods that mitigate, or eliminate, STL resin biotoxicity. We describe simple-to-adopt assays for measuring microbial cell response to native 3D-printed resin and treatments of 3D-printed resin. One assay measures changes in growth rates using a plate reader format, while the other quantifies lethal effects in a dose-dependent fashion. As a proof-of-concept, growth and cell death of both *Escherichia coli* XL1B, a genetically manipulated and sensitive lab strain, and *Pseudomonas putida* KT2440, a robust soil bacterium known to tolerate and biodegrade organic contaminants, were tested with exposure to native and treated Formlabs Clear Resin as printed using a Form 2 STL printer. Resin treatments included water leaching, thermal treatment, and UV crosslinking. *P. putida* KT2440 displayed limited adverse effects from exposure to 3D-printed resins, even without subsequent treatment. However, *E. coli* XL1B was much more sensitive to resin

[2] In preparation as: Kadilak, A. L.; Harrington, C.; Bridges, C. M.; Gage D. J.; Shor, L. M., Methods to quantify and improve microbial biocompatibility of stereolithography 3D-printed resin.

exposure and cell doubling times during active growth were increased by 2-4x when comparing controls with cells exposed to resin. Toxicity assays for *E. coli* showed 1-3 log reduction in viable cells counts with increasing resin dose. Resin treatments including 24 h leaching in DI water, thermal treatment at 60 °C, and UV exposure drastically improved *E. coli* cell viability counts, such that they were statistically indistinguishable from controls with no resin. The range of cellular responses to 3D-printed resin vary, but adverse effects can be reduced by treatments designed to remove labile polymers and crosslinking agent. These assays can be used to determine the responses of other untested cell types to a variety of 3D-printed resins under a wide range of growth conditions and material pre-treatments.

3.2 Introduction

In recent years, 3D-printing has become a promising technology for scaling up and simplifying manufacture of microfluidic devices.[14, 16, 18-22] Like microfluidic devices in general, 3D printed devices enable more faithful replication of natural microbial habitats and permit real-time, *in situ* observation of cellular responses to complex microenvironment conditions.[71] 3D printed devices offer several advantages including reduced equipment cost and superior complex geometry fabrication capabilities, with libraries for complex shapes and specialized fittings (i.e. LuerLock fittings).[14, 16] Most importantly, 3D printing offers ease of use and increased production speed with affordable spatial resolution on the order of 100-200 μm.[14]

Additive manufacturing techniques are much simpler to use when constructing 3D geometries than conventional microfluidic fabrication methods. Traditionally, fabricating a 3D shape would require either a multi-layered master, which can be very complicated to fabricate using photolithography, or multiple layers of PDMS bonded on top of one another, which can be difficult to align properly. Even using these methods, layers would have to be orthogonal to each

other in a semi-2D geometry, but with a 3D-printer, complex 3D shapes such as corkscrews or spirals can be fabricated in a single step.[14, 19, 29]

The speed with which devices can be produced using additive manufacturing, as opposed to traditional microfabrication techniques, is an important benefit. 3D-printing techniques can decrease the time between design iterations during prototype development or scaling up production of devices. Generally, it takes weeks to fabricate a microfluidic master using photolithography techniques. Large-volume commercial methods are available for mass production of microfluidic devices using injection molding, but the molds and other equipment are very costly and not a realistic option for smaller companies or academic research.[14] With a desktop 3D printer, the entire process from design to finished product can take from just a few hours to a day.[20]

A number of researchers have taken advantage of the capabilities of 3D-printing to design and manufacture devices with a variety of microfluidic applications. Some groups have created 3D-printed devices that serve as microreactors for multiple organic and inorganic reactions, with the ability to incorporate in-line testing of reaction products.[19, 20] Other researchers have used 3D-printing to develop efficient 3D mixing geometries,[19] which would be too complex or difficult to fabricate using traditional soft lithography methods, and integrated 3D-printed pneumatic valves to allow for automated flow control in printed microchannels.[25] Additionally, microreactors and mixing elements have been created that can be combined as modular pieces like building blocks to be adapted for a variety of applications.[72, 73]

Devices have also been fabricated using 3D-printing for biological applications. On a larger scale, 3D-printers have been used for tissue scaffolding[74, 75] or even printing cell

suspensions directly,[76] surgical prep devices,[77] and drug delivery.[78] At the microfluidic scale, 3D-printing has mainly been utilized for cell separation and screening assays. Some examples include remote detection of *Staphylococcus aureus* from environmental samples,[26] microbial fuel cells for on-line measurement of water quality,[79] cell sorting in a flow stream,[29] and sensors for cell growth in response to a variety of antibiotics and other stimuli.[27, 28] Biological applications where cells are in contact with devices for an extended time are typically made from acrylonitrile butadiene styrene (ABS) or a combination of ABS[26] with either polycarbonate[79] or polypropylene,[27] all classified as a biocompatible materials. To print with ABS, a Fused Deposition Modeling (FDM) printer is generally employed, which extrudes a filament of the polymer onto the build platform to create the part.[15, 24]

Resolutions that can be achieved with FDM printers are often significantly lower than stereolithography (STL) printers, which use two focused UV lasers to solidify photo-curable polymer resins, generally acrylate or methacrylate-based polymers. Unfortunately, photo-curable resins used for STL 3D-printing have been shown to be toxic to cells, possibly due to labile photoinitiators or uncross-linked monomers and oligomers, which can leach out of the resin.[15, 23, 24] While a number of studies have utilized STL printers to make microchannels or other devices that come in contact with cells, most are used for sensing applications[26] or cell sorters,[29] where cells are in contact with the 3D-printed resin for only short time periods. Other applications that require long term survival of cells within the device have used membranes or other barriers to prevent direct contact between cells and the acrylate resins.[28] One study tested various 3D-printed resins with different treatments to mitigate biotoxicity to zebrafish, where the percent of eggs that hatched and deformities in the fish were monitored over the course of several days. The authors found that most untreated STL resins resulted in lower hatching rates and were linked

with deformities in the fish embryos, but resin treatments including additional UV exposure or washing in water or ethanol were able to mitigate some of the toxic effects.[30-32]

However, little is known about the effects of these 3D-printed resins on other organisms or cells of interest to the microfluidic community, and over longer exposure durations. Many researchers have noted that much more biocompatibility testing of 3D-printed resins is needed.[15, 23, 24] In this paper, we describe a simple assay designed to measure change in bacterial growth rates in a micro-well plate design and quantify dose-dependent cell death with exposure to treated and untreated STL resin disks. We report microbial response of *Pseudomonas putida* KT2440 and *Escherichia coli* XL1B to the 3D-printed resins tested over periods of 1-2 d. Based on these findings, we suggest treatment methods that drastically improved biocompatibility of the STL 3D-printed resin used in this study. CAD designs for a modular well plate and printed disks are available so other researchers can adopt these assays for other cell types.

3.3 Experimental Materials and Methods

3.3.1 Chemicals

Clear Resin GPCL02 (Formlabs, Somerville, MA) was used for all studies. Lysogeny broth (LB) (granular powder), agar (granular powder), phosphate buffered saline (PBS) (1× powder concentrate), and isopropanol (histological grade) were all purchased from Fisher Scientific and used as received. Deionized (DI) water (resistivity $\geq$ 18.2 MΩ cm^{-1}) was produced from a Direct-Q 3 UV Millipore ultrapure water system.

3.3.2 Bacteria strains, plasmids, and culture media

Plasmids pCMB34 and pCMB55 were used to express *sfGFP*, a gene for production of green fluorescent protein (GFP), from the strong, constitutive promoter *Ptrc* in *Escherichia coli* XL1-Blue MRF' Km^r (Stratagene, CA) and *Pseudomonas putida* KT2440 (kindly provided by Victor de Lorenzo of the Spanish National Center for Biotechnology, Madrid, Spain), respectively. Plasmid pCMB34 uses a modified RSF1010 origin of replication, and pCMB55 uses the pBBR1 origin; both plasmids confer tetracycline resistance. Strains were grown in Lysogeny Broth (LB; 10 g/L tryptone, 5 g/L yeast extract, 10 g/L NaCl) for routine maintenance, 1X PBS (81% sodium chloride, 14% sodium phosphate dibasic, 3% sodium phosphate monobasic, 2 % potassium chloride) for resin biotoxicity experiments. All broth cultures and microfluidic device inocula contained tetracycline (0.01 mg/mL) for plasmid maintenance.

3.3.3 Preparation of 3D-printed disks and wells

3-D printed disks were designed using Solidworks 2015, a CAD software, imported into PreForm software, and then printed on a Form 2 stereolithography printer (Formlabs, Inc., Somerville, MA) at a resolution of 0.025 mm. Disks were designed with a 9.5 mm diameter so they would fit into a flat-bottomed 48-well plate and with a 0.5 mm thickness to minimize added opacity in plate reader experiments. CAD images and 3D-printed disks can be seen in Figure 1. After printing, disks were soaked in isopropanol (IPA) for approximately 20 min to remove any un-crosslinked resin, rinsed with fresh IPA, and allowed to dry in air and ambient room lighting for a minimum of 16 hours, per manufacturer instructions. Once an appropriate amount of drying time had been allowed, scaffolding supports were removed. Disk edges were then sanded using a minimum of 3200 grit sandpaper and quickly rinsed in MilliQ water; this was done to remove

rough edges left by supports, which would prevent the disks from properly fitting into the wells of the 48-well plate if left intact.

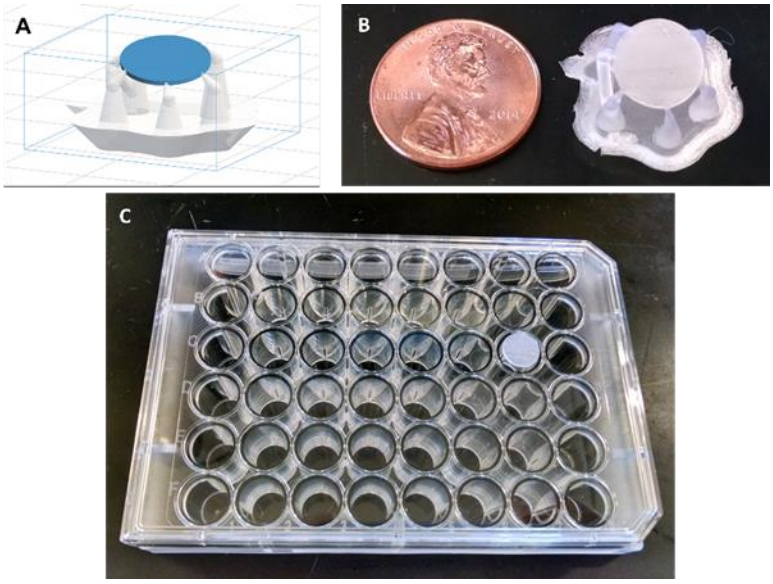

Figure 3-1. (A) CAD drawing of 9.5 mm diameter, 0.5 mm thickness disk with support scaffolding as showing in Preform software; (B) printed disk before removal of supports; and (C) disk with supports removed and edges sanded placed on top of a 48-well plate for scale.

3.3.4 Microbial growth curve assay

Growth curves were conducted in LB media using *E. coli* XL1B and *P. putida* KT2440 bacteria strains to test the effect of 3D-printed resin on their growth and determine whether certain treatments could be performed on the resin to improve biocompatibility with these particular strains. These growth curves were performed in commercially available 48-well plates with 3D-printed disks added to the bottom of the wells.

First, disks were printed and prepared as described in section 2.4. The disks were then separated and given the following treatments: (1) no treatment (disks were covered with aluminum foil to prevent further ultraviolet (UV) light exposure); (2) 24 h water rinse, where disks were added to 10 mL of MilliQ DI water per disk in a sterile culture tube and shaken at

approximately 120 RPM at 30 °C for 24 h, then dried in a 60 °C oven for 5 min; (3) UV light exposure for 4 min at approximately 30 mW/cm^2 intensity using an ELC-500 UV curing chamber (Electro-Lite Corp., Bethel, CT) ; (4) 24 h water rinse, dried in 60 °C oven for 5 min, followed by 4 min UV light exposure at 30 mW/cm^2; and (5) 24 h in 60 °C oven. These treatments were selected as a result of recommendations from Formlabs[80] and from the more successful treatments used with zebrafish by other researchers.[30-32] In the 48-well plate, treated and untreated disks were added to wells, with each treatment being performed in triplicate, so disks with treatments (1)-(5) were added to three wells each. Additionally, untreated disks were added to three separate wells to serve as blanks. Six wells were left empty: three to serve as media blanks and three to serve as positive controls for bacteria growth. The remaining perimeter wells were filled with 1 mL each of sterile MilliQ DI water to help prevent evaporation from the culture wells over the course of the experiment. Figure 2 illustrates the layout of the 48-well plate with the different disk treatments, blanks, and controls.

An overnight culture of the preferred strain of bacteria was started by inoculating 3 mL of LB media plus 0.01 mg/mL tetracycline in a 15 mL culture tube with bacteria cells from long term freezer stock or a plate. Prior to being placed in the shaker incubator, caps of the culture tubes were loosened to allow adequate oxygen exchange for cell growth. Cells were then grown at 30 °C and 120 RPM in a shaker incubator until reaching stationary phase, which was approximately 18-20 h for *P. putida* KT2440 and 22-24 h for *E. coli* XL1B. After the required time to reach stationary phase, culture tubes were removed from the incubator and 1 mL of cell culture was pelleted by centrifuging at 21,000 RCF for 1.5 min. The supernatant was removed and cells were resuspended in fresh LB with 0.01 mg/mL tetracycline. The optical density at 600

nm(OD 600) of 200 µL of washed cell culture was read using a Synergy HT plate reader (BioTek, Winooski, VT) and the cell culture was diluted to an OD 600 of ~0.1.

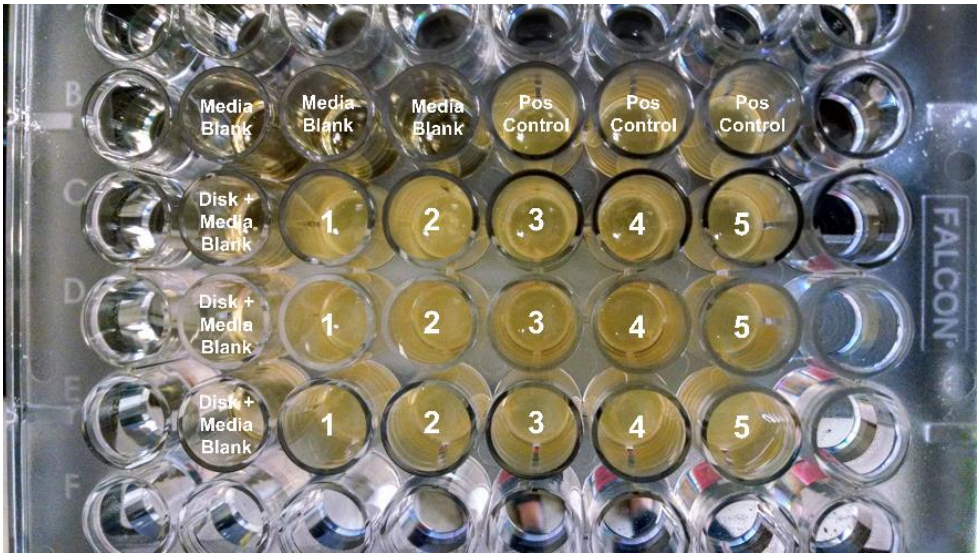

Figure 3-2. Annotated photograph of a 48-well plate within which the growth curve assay has been conducted. All perimeter wells have been filled with water to prevent excess evaporation during data collection in the plate reader. Media blanks (LB) and blanks with LB + a disk were included in triplicate as indicated above. Positive controls were also conducted in triplicate with just bacteria growing in LB media, but no disk. Treatments 1-5 were conducted in the wells indicated, where the treatments are as follows: (1) no further treatment (disks were covered with aluminum foil to prevent further ultraviolet (UV) light exposure); (2) 24 h water rinse with 10 mL MilliQ DI water per disk, shaken at approximately 120 RPM at 30 °C for 24 h, then dried in a 60 °C oven for 5 min; (3) UV light exposure for 4 min at approximately 30 mW/cm^2 intensity; (4) 24 h water rinse, dried in 60 °C oven for 5 min, followed by 4 min UV light exposure at 30 mW/cm^2; and (5) 24 h in 60 °C oven.

After disks were added to the 48-well plate as discussed above, 200 µL of LB media with 0.01 mg/mL tetracycline was pipetted into the blank wells where no cells would be added (3 wells with disks, 3 wells with no disks). To wells where bacteria growth curves were to be conducted, 190 µL of LB with 0.01 mg/mL tetracycline was added, and the well was inoculated with 10 µL of washed cells at ~0.1 OD 600.

Growth curves for *P. putida* KT2440 were conducted at 30 °C with medium shaking for approximately 48 h in the plate reader. Growth curves for *E. coli* XL1B were conducted at 37 °C with medium shaking for approximately 48 h. Every 10 minutes, OD 600 was measured to

determine the cell density and fluorescence intensity (485 nm excitation, 528 nm emission) was measured to quantify the GFP production by cells.

3.3.5 Microbial dose-dependent toxicity assay

In order to determine the effect of increasing doses of 3D-printed resin on liquid bacterial cultures, an assay was developed in which bacteria cells were incubated in PBS solution with varying numbers of 3D-printed disks for 24 h and viable cells counted.

3D-printed disks printed and prepared as detailed in section 2.4 were separated into two groups: treated and untreated. Both groups were allowed to dry overnight after the IPA soak following printing. Untreated disks were then covered with aluminum foil to prevent any additional UV exposure from overhead lights. Treated disks were rinsed in water for 24 h, adding 10 mL of MilliQ DI water per disk in a sterile bottle, and shaken at approximately 120 RPM at 30 °C for 24 h. The treated disks were then dried in a 60 °C oven for 5 min and exposed to UV light for 4 min at approximately 30 mW/cm^2 intensity using an ELC-500 UV curing chamber (Electro-Lite Corp., Bethel, CT).

The day prior to starting the incubation, an overnight culture of the preferred strain of bacteria was started using the same method detailed in section 2.5. Similarly, after the required time to reach stationary phase, culture tubes were removed from the incubator and cells were pelleted, resuspended in 1× PBS solution, and adjusted to OD 600 = 0.2 (Synergy HT plate reader, BioTek, Winooski, VT). A large volume of OD 600 = 0.2 cells in PBS was prepared and used for all treatments to ensure consistency.

From the master mix of cells in PBS + tetracycline at an OD 600 of 0.2, 500 µL was added to 2500 µL of PBS with 0.01 mg/mL tetracycline, for a total of 3 mL of cells in PBS

diluted to an OD of approximately 0.03 in a sterile 15 mL culture tube. For each bacteria strain, two culture tubes were assembled for each of the following numbers of 3D-printed disks added, one set with treated disks and one set with untreated disks: 0 disks (negative control), 5 disks, 10 disks, and 15 disks. The top of the tube was slightly loosened to allow for oxygen exchange, and the PBS-cell dilution was incubated and shaken with the desired number of 3D-printed disks for 24 hours at 30 °C for *P. putida* and 37 °C for *E. coli*.

After 24 h, 200 µL samples were taken from each of the tubes and pipetted into a 96-well plate, and a serial dilution performed to dilution factor of 10^{-6}. From the wells for dilutions ranging from 10^{-1} to 10^{-6}, 5 µL spots were pipetted, in triplicate, onto an LB agar plate with 0.01 mg/mL tetracycline. Plates were then incubated at 30-35 °C until colonies were visible. An example of the serial dilution spots can be viewed in Figure 3. Photographs of the spots were then taken and colonies were counted for further analysis. Average viable cell concentrations were calculated by dividing average cell counts by the spot volume of 5 µL, converting to cells/mL, and then dividing by the dilution factor for the spot counted. For each condition and bacteria strain, this average value was calculated from triplicate spots from two separate tubes, so from a total of 6 spot counts.

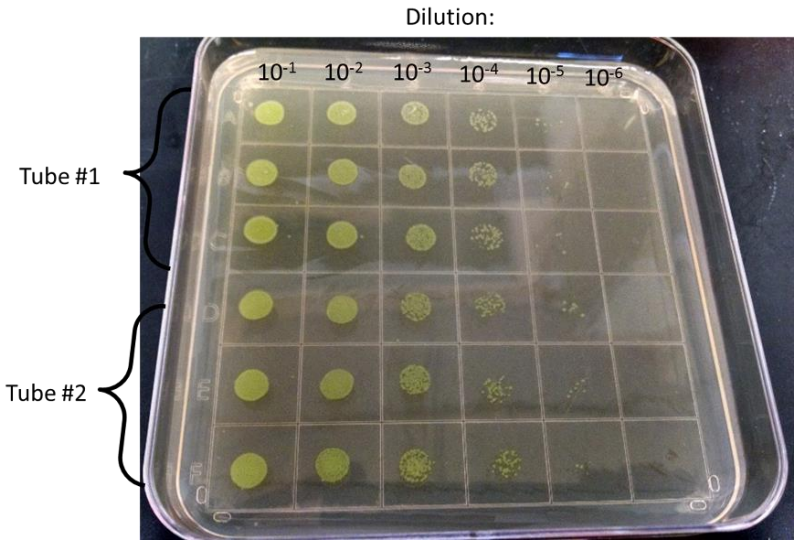

Figure 3-3. . Example of a dilution series spot plate of bacteria with dilution factor indicated above (10^{-1} to 10^{-6}). Each spot is 5 µL in volume and dilutions are made from each of two culture tubes containing bacteria diluted in PBS with a given number of treated or untreated 3D-printed disks after 24 h incubation; each dilution is spotted in triplicate.

3.4 Results and Discussion

3.4.1 Resin treatments overview

The resin used in STL 3D-printers is photocured with UV lasers and must therefore contain photoactive groups and a photoinitiator for crosslinking. While the exact formulation of Formlabs Clear Resin (GPCL02) used in these assays is proprietary, the safety data sheet states that the uncross-linked resin is composed of methacrylated oligomers, methacrylated monomer, and photoinitiator(s).[81] It is likely that the photoinitatior, when excited by the high intensity UV light from the focused lasers in the STL printer, causes cross-linking between the reactive methacrylate groups in the oligomers and monomers, resulted in a cross-linked polymer network that behaves as a hard plastic.[82] As stated in the experimental section, the manufacturer instructs that after printing is complete, finished pieces should be soaked in IPA for 15-30 min, depending on the printed piece size. The IPA swells the polymer and helps to dissolve any uncross-linked monomers and oligomers (and possibly photoinitiator) and remove them from the polymer

matrix. However, it is possible that not all uncross-linked resin and unused photoinitiator is removed during this step, and these toxic compounds could leach from resin into cell culture if further steps are not taken.[15, 23, 24]

Therefore, 3D-printed pieces without additional treatment beyond the IPA soak were compared to pieces with additional steps taken to try and remove any uncross-linked resin and photoinitiator. The manufacturer recommends an additional post-curing UV exposure step at 60 °C after the piece has fully dried from the IPA soak to help improve mechanical stability;[80] it is possible that thermal and/or UV treatment may promote cross-linking of any remaining monomer or oligomer. Therefore, additional treatment steps incorporating heating at 60 °C and additional UV exposure were tested, along with extended water rinses to leach labile materials, as described with beneficial effect by other researchers using zebrafish embryos.[30-32] Ethanol soak steps were also tested initially, but had adverse effects on the mechanical properties of the resin and the optical clarity of the printed disks, so were not included in the final study.

3.4.2 Bacterial strain selection

For both assays designed to test the biotoxicity of STL 3D-printed resin described in this paper, the bacteria strains used were *Escherichia coli* XL1B and *Pseudomonas putida* KT2440. These bacteria were chosen for this study because they are both commonly used in genetic research, so are representative of typical strains that biological researchers would be using. Additionally, both are non-pathogenic strains, and are therefore biosafety level (BSL) 1 and can be grown in a range of temperatures from 30-37 °C, so are accessible to many labs and researchers who would wish to test these bacteria with other resins or other culture media formulations. The particular strains used here also include plasmids, pCMB34 and pCMB55 for *E. coli* XL1B and *P. putida* KT2440 respectively, that encode for continuous or constitutive

production of green fluorescent protein (GFP) and incur tetracycline resistance. This enabled easier visualization of cells *in situ* within a microfluidic device and also allowed protein production of GFP to be measured while growth curves were collected on a microplate reader. Additionally, the tetracycline resistance allowed incorporation of this antibiotic in the culture media and saline solutions used during these assays; this may help prevent contamination from bacteria found in the laboratory environment since autoclaving the STL resin used in this study may affect its mechanical properties.

Additionally, *E.coli* XL1B and *P. putida* KT2440 represent different points along the spectrum of robustness for bacteria strains used in the laboratory. *E. coli* XL1B is a cloning strain that is frequently used to determine whether or not the desired genes or DNA have been incorporated into a cloning vector using a blue-white screen. In order for this screen to work correctly, the cells must have a deletion of the *lacZ* gene, which is a part of the *lac* operon that acts to help the cell to break down lactose. Deletion of this important gene and several other mutations in *E. coli* XL1B can negatively affect cell metabolism, making this strain of bacteria slower growing and sensitive to environmental disruptions. This can be contrasted with *P. putida* KT2440, a plant root symbiont,[83] which has been shown to be quite versatile in what carbon sources it can break down, including toxic organic compounds, making it a strain commonly used in bioremediation applications.[84, 85] Therefore, these two strains were chosen to represent both a lab strain that may be more sensitive to low levels of uncross-linked resin leaching into culture media and a bacteria strain that may be able to withstand certain levels of remaining oligomer, monomer, or photoinitiator.

3.4.3 Microbial growth curve assay results

Growth curves were conducted for cells in contact with 3D-printed disks that underwent the various treatments detailed in Section 2.5 and compared to control cells without any contact with 3D-printed resin. An example of the experimental setup in a 48-well plate layout is shown in Figure 2. Each condition was repeated in triplicate, as were blanks with and without disks. Growth curves were conducted over a period of 48 h in a microplate reader at 37°C for *E. coli* XL1B and 30°C for *P. putida* KT2440. In each well, a total of 200 µL was cultured and shaken continuously to help prevent cell clumping and maintain adequate aeration in the liquid phase. Growth curves were conducted on two separate occasions for each bacteria strain.

Figure 4 shows representative growth curves for both *E. coli* XL1B (A-C) and *P. putida* KT2440 (D-F). Plots A and D show OD 600 measurements, proportional to cell density, over the first 36 h of growth; B and E show fluorescence intensity measurements, proportional to GFP concentration, at an excitation of 485 nm and emission of 528 nm; C and F show specific fluorescence, or fluorescence intensity at a given time divided by the OD 600 for that same time, to determine approximately how much GFP is produced per cell for the different conditions tested. Each point shown is the average of the three triplicate wells for that condition with the average blank value subtracted. Error bars are not shown in these plots so the various conditions can be more easily observed visually, but are included in Supplemental Figure S-1.

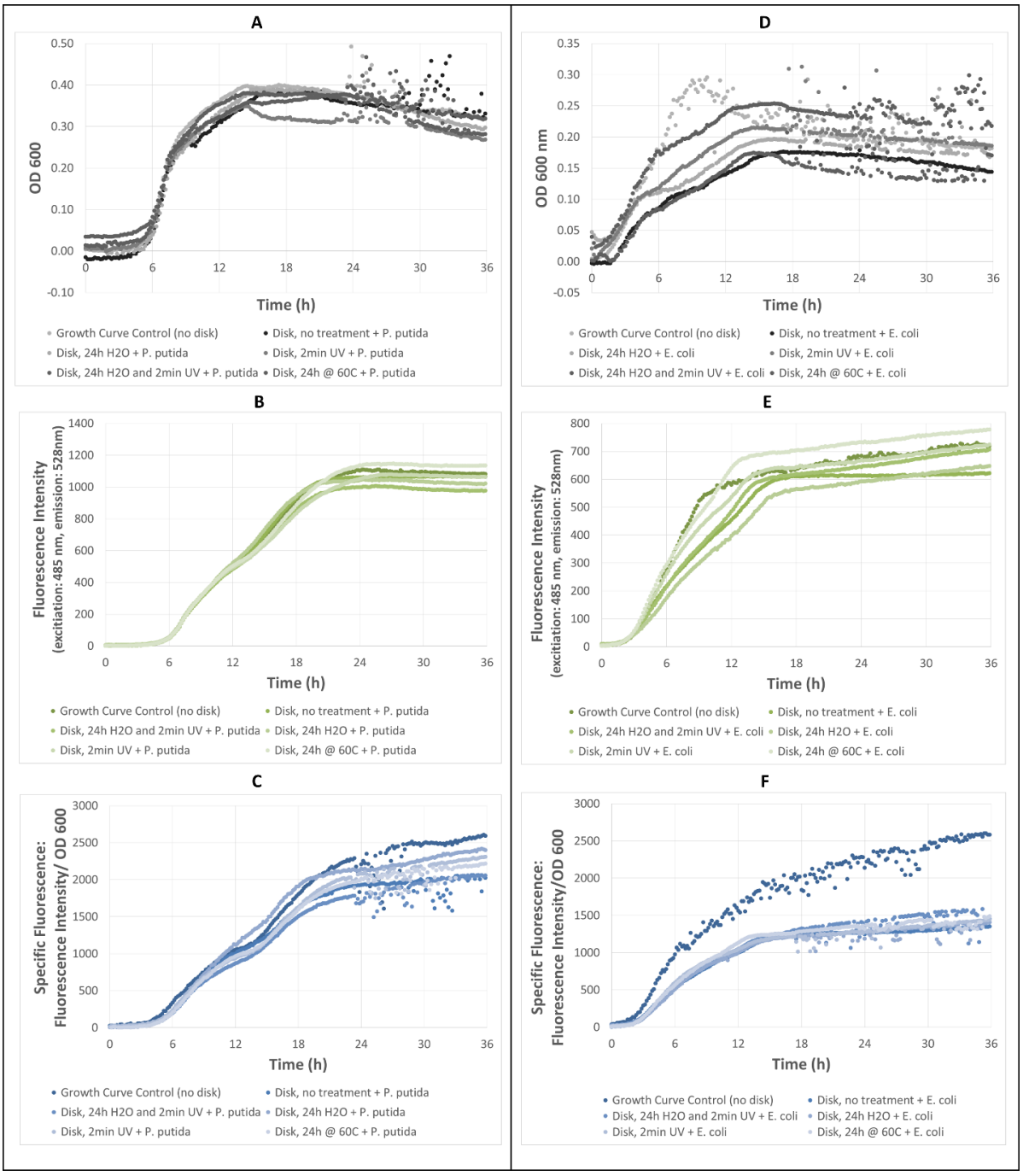

Figure 3-4. Microbial growth curve assay results for (A-C) *P. putida* KT2440 and (D-F) *E. coli* XL1B. Plots A and D are the OD 600 readings from the plate reader measuring cell density; B and E are fluorescence intensity readings with an excitation wavelength of 485 nm and a emission wavelength of 528 nm to measure GFP production by cells; C and F are specific fluorescence, calculated by dividing the OD 600 values by the fluorescence intensity, to allow comparisons of the relative fluorescence output per cell. Measurements were taken by the plate reader every 10 min for 48 h total. Points plotted are averages of three replicates for each condition, with blank averages subtracted. It is likely that noisy data in stationary phase is caused by cells clumping at high concentrations – cell clumps were often observed when well plates were removed from the reader after 48 h. Error bars were not included to allow for improved plot clarity, but are shown on plots in supplemental information.

3.4.3.1 Optical density growth curve results

These plots indicate that for *P. putida* KT2440, there was little difference between the growth pattern of the bacteria in the control, which had no exposure to 3D-printed resin, and any of the bacteria grown in the presence of 3D-printed disks. This was noted for disks with and without further treatment. However, for *E. coli* XL1B, a significant change in the growth pattern rate was observed between the control and all of the conditions where cells were in contact with 3D-printed disks. This was very evident in the OD 600 measurements. Without exposure to resin, cell density increased steeply from approximately 2-9 h. However, for each of the other conditions where cells were grown in the presence of a 3D-printed disk, there appeared to be two sub-phases of exponential growth between lag and stationary growth; initially, from approximately 2-4 h, cells grew at a rate similar to the control, but after 4 h until about 12 h, cells grew at a significantly slower rate.

Linear approximations for these two sub-phases of exponential growth calculated for *E. coli* XL1B are shown in Table 1. These values show a marked decrease in the slopes for the linear fit approximation in exponential phase 1 (2-4 h) compared to exponential phase 2 (4-9 h for control, 4-12 h for all others), such that the slope in phase 2 was approximately 60% less than the slope in phase 1 for all but the control. For *P. putida* KT2440, a longer lag phase was observed, and all conditions, control included, show a similar change in slopes of the linear fit approximations

While there are differences in the absolute values of the OD 600 and some differences in the values at which cells reach stationary growth when comparing the different treatment methods, the error bars were large for each of the curves; because of this, it is difficult to definitively conclude that specific treatments reduced resin toxicity more than others. Variation

in optical clarity of the printed disk, including small defects on the surface, could have contributed to the variability in optical density results. Improved clarity or uniformity between disks could improve this aspect of the assay.

Table 3-1. Approximated linear slopes for average OD 600 over time during exponential growth phases of growth curve assay, showing two phases of growth before stationary phase is reached, rather than a simple exponential growth formula as described by theoretical equations 3.1-3.3. *P. putida* KT2440 has a longer lag phase than *E. coli* XL1B under the conditions used in these experiments, which is why the timing varies.

Bacteria Strain	Growth Curve Condition	Growth Phase	Line Slope (OD/h)
E. coli XL1B	Control (no disk)	Exp 1 (2-4h)	0.0424
		Exp 2 (4-9h)	0.0364
	Disk, no treatment	Exp 1 (2-4h)	0.0286
		Exp 2 (4-12h)	0.0095
	24h H2O + 2min UV	Exp 1 (2-4h)	0.0244
		Exp 2 (4-12h)	0.0106
	2min UV	Exp 1 (2-4h)	0.0295
		Exp 2 (4-12h)	0.0126
	24h H2O	Exp 1 (2-4h)	0.0252
		Exp 2 (4-12h)	0.0087
	24h @ 60°C	Exp 1 (2-4h)	0.0354
		Exp 2 (4-12h)	0.0124
P. putida KT2440	Control (no disk)	Exp 1 (6-8h)	0.1049
		Exp 2 (8-14h)	0.0212
	Disk, no treatment	Exp 1 (6-8h)	0.0993
		Exp 2 (8-14h)	0.0191
	24h H2O + 2min UV	Exp 1 (6-8h)	0.0919
		Exp 2 (8-14h)	0.0214
	2min UV	Exp 1 (6-8h)	0.0963
		Exp 2 (8-14h)	0.0180
	24h H2O	Exp 1 (6-8h)	0.1005
		Exp 2 (8-14h)	0.0245
	24h @ 60°C	Exp 1 (6-8h)	0.0962
		Exp 2 (8-14h)	0.0169

3.4.3.2 Fluorescence intensity and specific fluorescence curves

Similar to the OD 600 data, fluorescence intensity and specific fluorescence curves show little difference in growth rate for *P. putida* KT2440 between the control and treatments where cells were grown in the presence of 3D-printed disks. For *E. coli* XL1B, when the specific fluorescence was calculated, all of the curves for the various disk treatments converged, while the specific fluorescence for the control where cells did not have any contact with 3D-printed resin was markedly higher. This result suggests that the *E. coli* XL1B cells in contact with 3D-printed resin were producing less GFP per cell than the control, regardless of resin treatment. This result suggests more subtle effects to cell health must be determined in future work, in addition to cell growth and cell death.

3.4.3.3 Quantifying doubling time and specific growth rate

Differences in cell growth were quantified in terms of the doubling time, τ_d, and the specific growth rate, μ. However, for both bacteria strains and for all conditions save possibly the control for *E. coli* XL1B, cells did not exhibit an ideal theoretical exponential growth pattern. This can be more easily observed when plots were viewed with the y-axis on a log scale, as seen in Supplemental Figure S-2. Ideally, the entire exponential phase should appear linear on a semilog plot, and then level out with a minimal transition period into stationary phase. If this is the case, theoretically, the growth rate during the exponential phase is first order and is expressed as follows:[86]

$$\frac{dX}{dt} = \mu X \tag{3.1}$$

Initial conditions are set such that $X = X_0$ when $t=0$, where t is time and X is cell concentration and is assumed to be proportional to OD600 measurements. An integration can be performed to

reach the following algebraic equation that can be used to calculate the cell concentration at any given time during exponential phase:

$$X = X_0 e^{\mu t} \tag{3.2}$$

If an exponential fit is made to the linear section of the growth curve plotted on the log scale for *X* or OD 600, the overall coefficient is the initial value for cell concentration and the coefficient to t in the exponent is the specific growth rate, μ. The doubling time is then defined as follows:

$$\tau_d = \frac{ln2}{\mu} \tag{3.3}$$

Deviations from ideal behavior can occur when cells are grown in a complex media where there are multiple substrates for the bacteria to consume, and growth rates can change when cells switch from a preferential source to a secondary source. Also, in the case of *E. coli* XL1B cells grown in the presence of 3D-printed disks, which exhibit a very different growth pattern compared to the control, cells may have experienced adverse effects of the 3D-printed resin and may have altered their metabolic rate in response. In either case, the specific growth rate and thus doubling time cannot be determined theoretically by fitting the data. Instead, the doubling time was measured empirically and the specific growth rate calculated by manipulating equation 3.3. For consistency, the doubling time was measured for cell growth between 37.5% and 75% of the approximate OD 600 at stationary phase. The OD 600 at stationary phase was assumed to be 0.2 for *E. coli* XL1B, so the doubling time was measured between 0.075 and 0.15 OD 600; for *P. putida* KT2440, the stationary phase OD 600 occurred at approximately 0.4, so the doubling time was measured between 0.15 and 0.3 OD 600. Table 2 lists these empirically measured doubling times (τ_d, in h) and the specific growth rates (μ, in h^{-1}) for each growth curve condition for both bacteria strains. For *P. putida* KT2440, there is a slight increase in doubling

time, and therefore decrease in the specific growth rate, when comparing the control to the growth conditions with 3D-printed disks present. However, for *E. coli* XL1B there was a sizeable increase in doubling time and decrease in specific growth rate when comparing the control to all conditions with 3D-printed disks.

Table 3-2. Table of doubling time, τ_d, measured for cell growth from 37.5% to 75% of approximate OD at stationary phase and the specific growth rate, μ, calculated from the empirical doubling time for each bacteria strain. Doubling time from 0.075 to 0.15 OD 600 was used for *E. coli* XL1B, which had an OD 600 of approximately 0.2 at stationary phase; doubling time from 0.15 to 0.3 OD 600 was used for *P. putida* KT2440, which had an OD 600 of approximately 0.4 at stationary phase. These doubling time measurements were made from the average OD 600 curve for each strain and growth condition.

Bacteria Strain	Growth Curve Condition	Empirical/Measured Doubling Time, τ_d (h)	Calculated Specific Growth Rate, μ (h^{-1})
E. coli XL1B	Control (no disk)	1.67	0.42
	Disk, no treatment	8.33	0.08
	24h H2O + 2min UV	6.83	0.10
	2min UV	7.00	0.10
	24h H2O	4.67	0.15
	24h @ 60°C	2.17	0.32
P. putida KT2440	Control (no disk)	2.33	0.30
	Disk, no treatment	4.33	0.16
	24h H2O + 2min UV	2.83	0.24
	2min UV	3.50	0.20
	24h H2O	3.67	0.19
	24h @ 60°C	3.67	0.19

3.4.3.4 Summary of growth curve results and relevance

All of the analysis methods used to quantify the differences between average growth curves for cells grown with 3D-printed disks that have undergone various treatment methods compared to the control case where cells were grown without exposure to STL 3D-printed resin appeared to tell a similar story. Specifically, it appeared the effect of 3D-printed disks, no matter the treatment, on the more robust *P. putida* KT2440 cells was minimal, at these dosages. However, the *E. coli* XL1B cells appeared to be more sensitive to the presence of the 3D-printed disks,

even those treated with additional methods to remove uncross-linked monomer or oligomer and photoinitiators. Decreases in growth rates and changes in growth pattern compared to the control were observed with this *E. coli* XL1B strain, but it is important to note that they were still able to grow in the presence of even 3D-printed resin at this dose, which was a concern at the beginning of this study.

3.4.4 Microbial dose-dependent response assay results

The cell death response of stationary phase *P. putida* KT2440 and *E. coli* XL1B was measured as a function of varying doses of 3D-printed resin. Varying numbers of STL 3D-printed disks (9.5 mm diameter, 0.5 mm thickness) were added to cells in liquid culture, suspended in PBS solution, and viable colonies counted after 24 h of exposure. Each disk had a surface area of approximately 1.6 cm^2, and therefore in 3 mL of culture media, the surface area:volume (SA:V) ratio for each condition tested is shown in Table 3, where it can be compared to values for microchannels of varying dimensions. As this table shows, increasing numbers of disks result in higher SA:V ratios, but they only begin to approach the ratios found in millifluidic channels, while typical microfluidic channels have much higher SA:V values. Therefore, any trends observed for the SA:V levels tested in this assay would likely be further amplified by the SA:V ratio found in actual 3D printed channels.

Table 3-3. Table of calculated surface area to volume (SA:V) ratios for the surface area of a given number of 9.5 mm diameter, 0.5 mm thickness 3D-printed disks in contact with 3 mL of cell culture. Below are indicated the SA:V for microchannels of a range of sizes. Surface area of a single disk was approximately 1.6 cm^2.

# Disks in 3 mL of cell culture	SA:V(cm^{-1})
5	2.6
10	5.2
15	7.8

SA:V for 100 µm x 30 µm channel ≈ 870 cm^{-1}
SA:V for 2 mm x 1 mm channel ≈ 30 cm^{-1}
SA:V for 5 mm x 5 mm channel ≈ 9 cm^{-1}

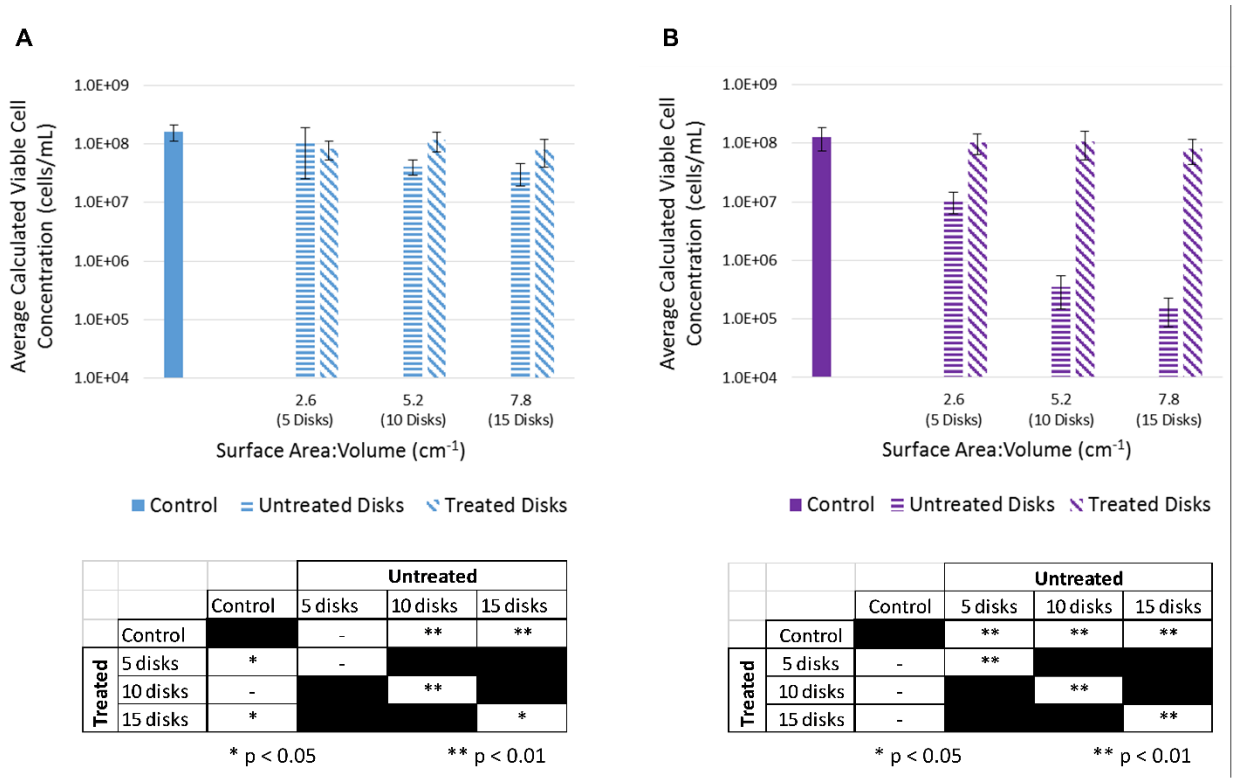

		Untreated			
		Control	5 disks	10 disks	15 disks
	Control		-	**	**
Treated	5 disks	*	-		
	10 disks	-		**	
	15 disks	*			*

* p < 0.05 ** p < 0.01

		Untreated			
		Control	5 disks	10 disks	15 disks
	Control		**	**	**
Treated	5 disks	-	**		
	10 disks	-		**	
	15 disks	-			**

* p < 0.05 ** p < 0.01

Figure 3-5. Microbial dose-response assay results. Plots show average calculated viable cell concentration after 24 h exposure to 3D-printed disks for (A) *P. putida* KT2440 and (B) *E. coli* XL1B. Averages were calculated from six colony counts total (triplicate spots from each of two tubes for the given condition); error bars are one standard deviation in the positive and negative directions. Tables indicate p-values calculated for the two conditions/treatments indicated by the intersection of the column and row labels. P-values were calculated with a 2-tail t-test with two samples for the viable cell concentrations calculated from all six spot colony counts, assuming unequal variance; the null hypothesis tested against was $H_0 = 0$, or that there was no difference between the two sets of samples examined.

Figure 5 shows results for average calculated viable cell concentration in cells/mL, determined from average colony counts for both *P. putida* KT2440 (A) and *E. coli* XL1B (B). Each average was calculated from colony counts from a total of six 5 µL spots plated from dilutions of the cells in PBS after 24 h incubation with or without disks; error bars show one standard deviation. The tables shown below the plots list p-values calculated for the two conditions/treatments indicated by the intersection of the column and row labels. P-values were calculated using a 2-tail t-test with two samples for the viable cell concentrations calculated from all six spot colony counts, assuming unequal variance.

3.4.4.1 Cell dose-dependent response observed with untreated resin

For both *P. putida* KT2440 and *E. coli* XLIB, there was a lower average concentration of viable cells for all numbers of untreated 3D-printed disks compared to the control, which had no disks added. For all but the 5 untreated disks condition for *P. putida*, this comparison between the viable cell concentrations for untreated disks vs. the control was statistically significant ($p < 0.01$). Additionally, a dose-dependent response was evident, with decreasing viable cell concentrations for higher SA:V values for resin exposure. This was particularly pronounced in *E. coli*, where a reduction of an order of magnitude was observed at the lowest addition of untreated disks compared with the control, and a decrease of three orders of magnitude for the highest exposure condition for untreated disks vs. the control.

3.4.4.2 Quantifiable improvement in cell viability with treated resin

Furthermore, these results show the effectiveness of the treatment methods used on the 3D-printed resin. The treated 3D-printed disks were rinsed in an excess of DI water for 24 h in a shaker incubator, dried at 60 °C for 5 min, and then exposed to additional UV. This treatment was selected after successful results during the growth curve assay, and because it would provide a chance for un-crosslinked oligomer, monomer, and photoinitiator to leach out of the polymer matrix into the water, and the elevated temperature and additional UV would allow for any final cross-linking of remaining components to occur. As shown in Figure 5, average viable cell concentrations for *P. putida* were equivalent for treated and untreated conditions for 5 disks, but for 10 and 15 disk counts, a statistically significant improvement could be seen with the treated disks. Again, this improvement was even more pronounced in the *E. coli* cultures, where the average cell concentrations were improved from one to three orders of magnitude reductions for

untreated 3D-printed disks, to values that were statistically the same as the control for all amounts of treated disks.

3.4.4.3 Summary of dose-dependent response assay results and relevance

More robust cells such as *P. putida* KT2440 may be minimally affected by the presence of untreated 3D-printed resin at lower SA:V ratios. There may however be evidence of a dose-dependent response, so higher exposure at SA:V levels found in micro or milli-fluidic channels may be detrimental. More sensitive strains such as *E. coli* XL1B may be severely impacted at even relatively low SA:V levels if 3D printer resin is untreated, and likely would not be able to grow at all in a microchannel with a very high SA:V value. Treatments designed to leach labile monomer, oligomer, and photoinitiator and/or reduce their mobility by further cross-linking resulted in cell viability improvements for both bacteria strains.

3.5 Conclusion

Developments in 3D-printing technology in the past few years have recently made it an attractive option for producing micro- and millifluidic devices with complex geometries. Stereolithography printers are commonly used in this burgeoning field because they able to achieve relatively high resolutions, on the order of tens to hundreds of microns, while being able to easily manufacture enclosed channels of printed resin. However, issues still exist with improving optical clarity and, very importantly, biocompatibility of the proprietary photoactive STL resins and the photoinitiators they require to form a cross-linked solid has not been thoroughly tested.

This research reports biocompatibility of the Formlabs Clear Resin printed using the Form 2 STL printer using two bacteria strains of varying robustness. In addition to testing two specific cell types with this particular resin, this work aimed to adapt an assay developed for testing

biocompatibility of zebrafish with 3D-printed resins[30-32] to a 48-well plate format that could be used to measure cells in active growth in a microplate reader along with another dose-response assay for cells in stationary phase.

The results from these assays with the two strains of bacteria tested here, *P. putida* KT2440, a soil microbe able to digest complex and even toxic carbon compounds, and *E. coli* XL1B, a lab strain that has been genetically manipulated and is therefore slower growing and more sensitive to environmental perturbations, suggest that more robust cells may be minimally affected by even untreated 3D-printed resins at low concentrations. More sensitive cells, like the *E. coli* used here, may experience changes in growth patterns even at very low concentrations, and exhibit strong dose-responses to untreated resin. However, data from the dose-response assay suggest that additional water rinse steps and UV treatment applied to 3D-printed resin to remove uncross-linked monomer, oligomer, or photoinitiator and fully cross-link any remaining materials may greatly improve outcomes.

In future work, this assay could be used for screening interactions between different cell types or growth media with 3D-printed resins. Additionally, 3D-printed well-plates or wells could be implemented to increase the SA:V ratio for growth curve assays so that conditions more accurately model exposure in a 3D-printed microchannel. Improved resolution and optical clarity of resins would also be beneficial for improving reproducibility of plate reader experiments.

3.6 Supplemental Information

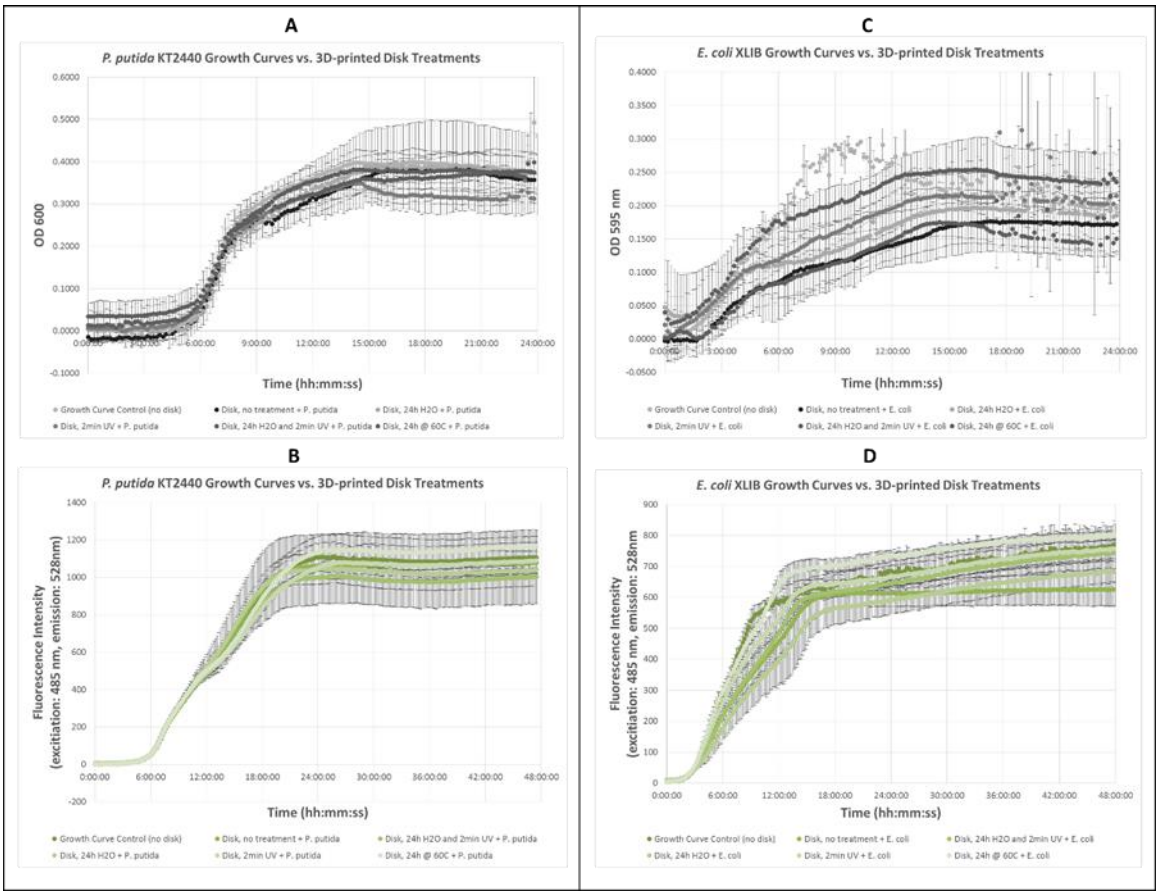

Figure 3-6(S-1). Growth curves including error bars.

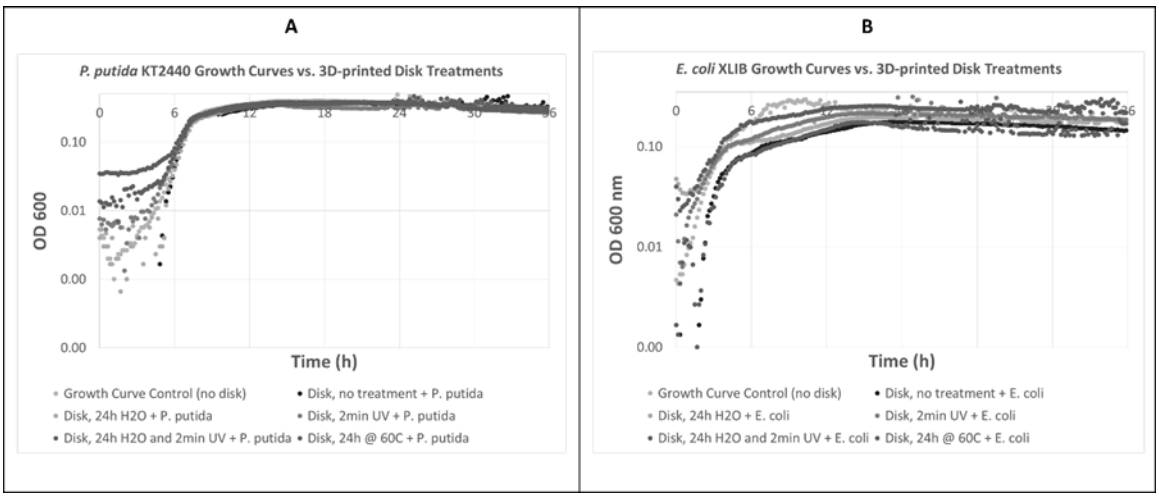

Figure 3-7(S-2). Growth curve 0D 600 on a semilog plot for (A) *P. putida* KT2440 and (B) *E. coli* XL1B.

4 A 3D-Printed Microbial Cell Culture Device with in situ PEGDA Hydrogel Barriers for Substrate Delivery[3]

4.1 Abstract:

Widespread adoption of microfluidic technologies in the biological fields had been hindered by the level of expertise needed to design and fabricate lab-on-chip devices using conventional techniques. However, the growing field of 3D-printing may now provide a solution to this problem, enabling simpler, faster, and cheaper production of millifluidic devices at a resolution approaching 100-200 μm. At this resolution, cell culture devices can be constructed that more accurately replicate natural environments in scale and geometry, compared to bulk volume culturing techniques. A number of microfluidics researchers have begun incorporating additive manufacturing into their work, using 3D-printed devices in a wide array of chemical, fluidic, and even some biological applications. However, the biocompatibility for proprietary 3D-printed resins, particularly those used in stereolithography (STL) printing, is a main concern. Because of the potential biotoxicy, STL 3D-printed devices have been largely avoided for long-term cell culture applications. However, preliminary results from a handful of studies suggest that certain treatment methods, such as extended water or ethanol rinses and additional UV exposure may help mitigate negative effects of resin in contact with organisms. Here, we describe a 3D-printed cell culture platform that was able to successfully culture *Psedudomonas putida* KT2440 bacteria for 44 h. We developed a method to pattern PEGDA hydrogel barriers *in situ* within a 3D-printed

[3] In preparation as: In preparation as: Kadilak, A. L.; Rehaag J.; Harrington, C.; Shor, L. M., A 3D-printed microbial cell culture device with *in situ* PEGDA hydrogel barriers for substrate delivery.

channel and characterized transport properties of the tracer dye toluidine blue through the hydrogel. These barriers were incorporated in a proof-of-concept device that was treated with extended water rinses and UV exposure to reduce leaching from 3D-printed resin and then cultured with *P. putida* KT2440. Growth media and oxygen were delivered to cells in the culture region via diffusive transport through the PEGDA from adjacent media and saline perfusion channels. *P. putida* KT2440 were engineered with a green fluorescent protein (GFP) plasmid, allowing cell density and localization within the channel to be visualized over the course of the experiment using fluorescence microscopy. Cells were observed clustering near the boundaries of PEGDA barriers where fresh substrate and oxygen were being delivered to the culture chamber via diffusive transport through the hydrogel. The cell culture device described here provides a flexible platform that can be simply fabricated for a wide variety of biological applications.

4.2 Introduction

In the past few decades since its development, the field of microfluidics has been used for many biological applications. These technologies have primarily been developed by engineering groups with years of experience in photolithography and soft lithography methods. Because of this, there has been a pre-requisite for a high technical level in the fabrication of these devices that may be difficult to attain for biologists interested in utilizing microfluidics in their research.[87] 3D-printing capabilities and costs have improved greatly in the past few years and this may provide a point-of-entry for many biologists into micro- and millifluidics. Already it has been shown to be a promising technology for scaling up and simplifying manufacture of millifluidic devices.[14-24] However, many issues need to be addressed concerning the still growing 3D-printing field to enable wide adoption in biological research. Particular concerns for

biological applications include the optical clarity, resolution, and biocompatibility of available printing materials. If these issues can be resolved, the advantages will likely outweigh the disadvantages for 3D-printing. In particular, the size scale of 3D-printed millifluidics may make them a good fit for cell culture experiments. Devices can be printed that grow different cell types in contact with each other on the same size scale in which they interact naturally, as compared to traditional bulk volume techniques such as culturing in flasks or on agar plates. Additional benefits of using additive manufacturing in producing these devices include ease of use, significantly lower equipment costs, faster production times, and the ability to fabricate devices with complex 3D geometries.

Producing millifluidics via 3D-printing is much simpler than the photolithography and soft lithography techniques typically used to fabricate microfluidic devices. Devices can be designed using a 3D CAD software, such as AutoCAD Inventor or Solidworks, and although it may seem prohibitive to have to learn this software, there are libraries and online resources available for importing many complex shapes and specialized fittings, i.e. LuerLock fittings.[14, 16] This allows researchers to import these CAD components into the software to use on their own or combine with their designs for the final device. As for actually printing the devices, there are a variety of options available. The technology has improved greatly in recent years, with reliable printing resolution now available on the order of 100-200 μm. Relatively inexpensive desktop stereolithography (STL) 3D-printers are now available anywhere between $2000-12,000.[14, 15] Alternatively, designs can be sent to an outside company, which will then print the device to the required specifications and mail out the finished product.[14] If this approach is taken, then the lab does not have to purchase its own printer. These outside companies possess expertise in device

production using more advanced machines with better resolution than desktop models, so this may be an attractive option for some labs.

3D-printed devices can be produced much faster than microfluidics made using traditional microfabrication techniques. Using photolithography methods to fabricate a microfluidic master can take several weeks and is an expensive and time consuming process. While techniques such as injection molding can be used to mass produce some microfluidics, this is not a technology readily accessible to startups or academic research laboratories.[14] Using additive manufacturing, researchers can design a CAD device, 3D-print the device, and prepare it for use all in a matter of hours.[20] This fast production time is the reason 3D-printers are widely used in industry for prototype production. To further decrease the time needed to design and manufacture a millifluidic device several researchers have utilized 3D-printed modules that can be fit together to form any number of channel configurations.[72, 73] Using these modular building blocks could enable adoption by groups without as much microfluidic development experience, as they could simply fit together components with the desired features to create their own custom device.

Lastly, it is much more straightforward to produce channels in complex geometries using 3D-printing. The closest one can get to a truly 3D-geometry using photolithography techniques and soft lithography casting is still just aligning multiple layers of semi-2D channels, and even this is complicated to fabricate. With a 3D-printer, even corkscrew-shaped channels, which would not be possible to make using conventional methods, can be fabricated simply.[14, 19] This capability may be very useful in trying to replicate natural systems on-chip, since cells exist and interact in 3D geometries, not flat planes, in their native environments.

For these reasons, many microfluidic researchers have begun incorporating 3D-printing into their work. 3D-printed microreactors with in-line product-testing have been developed for both organic and inorganic reactions.[19, 20] Length scales for these reactors are on the order of hundreds of micrometers to millimeters, and reactor volumes are typically on the order of microliters. 3D-printing has also been used to improve mixing by using 3D geometries such as corkscrew shapes and grooved surfaces in channel designs.[19] Recently, even more complex 3D-printed devices have incorporated printed pneumatic valves to control flow configurations.[25] As these various applications show, the technical capabilities and boundaries of 3D-printing are constantly being tested in the realm of micro- and millifluidics. Researchers have also begun using 3D-printing for microdevices with biological purposes, primarily cell separation and screening assays. For example, sensor devices have been developed to detect *Staphylococcus aureus* bacterial cells in environmental samples[26] and for detecting changes in cell growth with antibiotic administration.[27, 28] Additionally, a 3D-printed microbial fuel cell has been designed to measure water quality,[79] and a device has been developed to sort cells within a flow stream.[29]

Stereolithography (STL) printers are often used in these applications because they can achieve higher resolutions than Fused Deposition Modeling (FDM) printers and are more easily able to make fully enclosed channels. This is because FDM printers work by extruding and layering filaments of melted polymer or plastic onto the build platform; the resolution is determined by the size of the extruded filament and the melted polymer requires some time to solidify, making unsupported "ceilings" of an enclosed channel prone to collapse.[10, 11] Meanwhile, STL printers work by focusing UV lasers point by point in the desired pattern to solidify photo-curable acrylate or methacrylate-based polymer resins.[10, 11, 81] This process is repeated for each layer, and the resolution is determined by the size of the laser point and the

molecular weight of the polymer. Because the polymer cures and solidifies immediately upon UV exposure with the laser, enclosed channel structures printed using STL are more mechanically stable.

However, one major drawback of STL 3D-printers is that the photocurable methacrylate resins and photoinitiators may be toxic to cells.[15, 23, 24] A number of the biological applications listed previously have utilized STL printers to make devices, but for sensing applications[26] or cell sorters[29], cells were not in contact with the STL resin for an extended period of time, and other devices have incorporated membranes or other barriers to prevent direct contact between cells and the acrylate resins.[28] Otherwise, microdevices were printed using FDM printers, which can print biocompatible materials such as acrylonitrile butadiene styrene (ABS) or a combination of ABS[26] with either polycarbonate[79] or polypropylene.[27]

Since 3D-printing is a relatively new field, much is still unknown about the effects of 3D-printed polymers on organisms or cells in contact with them for an extended time period.[15, 23, 24] Some testing has been conducted on the effects of various 3D-printed resins on developing zebrafish embryos with promising results. Researchers found that while most untreated STL resins resulted in lower hatching rates and often caused deformities in the fish embryos, certain treatments, such as additional UV exposure or washing in water or ethanol, were able to help reduce biotoxicity issues.[30-32] The authors of this paper have recently worked to adapt and expand upon the assays used with zebrafish, to instead test the microbial biocompatibility of Formlabs Clear Resin printed using a Form 2 STL printer. We found that rinsing in excess DI water to remove uncross-linked methacrylate monomers and oligomers in addition to photoinitiator contained within the resin,[81] followed by heating to 60°C and additional UV treatment as recommended by the manufacturer,[80] significantly improved survival of bacteria

over 24-48 h. In this previous work two strains of bacteria were tested, one being a sensitive lab strain of *Escherichia coli* and the other a more robust strain of *Pseudomonas putida* frequently used in bioremediation applications due to its ability to consume otherwise toxic carbon compounds as substrates.[84, 85] For the robust *P. putida* KT2440, there were minimal effects caused by the 3D printed resin, even at higher doses. Therefore, with the proper treatment and with sufficiently robust cells, we hypothesized that it may be possible to successfully culture certain organisms within a 3D-printed channel over an extended period of time.

The simplest and most common microfluidic cell culture systems incorporate a chamber or channel in which where cells are confined and cultured, which is then connected to one or more perfusion channels that supply the immobilized cell population with substrates or nutrients and remove waste products. This connection between the culture area and the supply channels can also be used to expose cells to signaling molecules, other cells, stimulants, or any other behavior modifier of interest. Variations on this basic microfluidic design have been employed in various cell culture applications, including culture of stem cells,[8] cancer cells,[9, 88] immune cells,[9] epithelial cells,[10] white blood cells,[89] and bacteria.[90] In some cases, cells are immobilized so that flow from the perfusion channels does not flush out the culture chamber and/or motile cells do not exit the culture chamber. In other cases, very small capillary-sized channels connect the cell culture chamber to the perfusion channels. However, some applications require non-immobilized cell populations, and microchannels smaller than bacterial cells cannot be constructed using current 3D-printing techniques. Here, perfusion of fresh culture media to liquid bacterial cultures is achieved within low-cost 3D-printed (STL) devices using PEGDA hydrogel barriers photopatterned *in situ* within selected regions of the channel.

Hydrogels are hydrophilic polymers that form a cross-linked network and are able to absorb large quantities of water, often many times their own volume.[91-93] They exhibit elastic behavior that further increases their resistance to flow compared to a liquid, but still have diffusive transport properties similar to liquid water. Their highly hydrated state allows frequent transport of molecules across the polymer boundaries and within the gel.[94] The strong cross-linkages of the polymer network prevent hydrogels from being soluble in water, and allow them to retain a more stable physical structure.[92, 94] Due to these properties, synthetic and biopolymer-based hydrogels are widely used in biomedical[11, 95], biomolecular[96], microbiological[97-101], and drug delivery[91, 102] applications. Additionally, many microfluidic devices exist that utilize the diffusive properties of biocompatible hydrogels to develop stable concentration gradients in cell culture applications.[12, 90, 103-108] Hydrogels commonly used in the field of microfluidics for biological applications include synthetic polymers such as polyethylene glycol (PEG) and polyacrylamide. Naturally-derived hydrogel polymers such as the polysaccharides agar, agarose, and alginate, in addition to protein-based gelatin and collagen, are also widely utilized in microfluidic devices.

Among biocompatible hydrogels, many are easy to fabricate *in situ* because they can be thermally cross-linked, like agar or agarose, or polymerized when UV light is applied to the specified area, such as with photocross-linked PEG.[98, 99, 109-115] With photoactive PEG species such as polyethylene glycol methacrylate (PEGMA) and polyethylene glycol diacrylate (PEGDA), the active acrylate and methacrylate groups interact with one another to form a cross-linked network. The extent of cross-linking or polymerization can be varied to control diffusive properties of the hydrogel via size exclusion from the networked mesh, or via side chain properties, while resisting convective mixing within a microfluidic system.[97]

Previously, Saadi et al. [116] constructed a "ladder" device that consisted of microfluidic capillaries filled with collagen hydrogel to study the chemotaxis of red blood cells when exposed to a chemical gradient. However, the capillaries used were very narrow, only 3-10 μm, and their height was very small compared to the main channel, so diffusive flux was very low and the system took a long time to equilibrate. Additionally, fabrication of both the capillaries and main channels together required a two-layer master mold.

Here we describe the construction of robust PEGDA barriers within a 3D-printed channel for differential perfusion of culture media to non-immobilized cell populations. Our approach provides for higher flux, faster equilibration, and simpler fabrication than prior reports. We detail a method to selectively photophattern PEGDA barriers *in situ* inside a 3D-printed device. The transport properties of the PEGDA barrier were characterized by measuring experimental diffusion of a tracer dye and with computational fluid dynamics (CFD) simulations. Finally, the utility of our approach was illustrated using growth of *P. putida* KT2440 bacteria in a media and oxygen gradient. As a proof-of-concept, a 3D-printed device was constructed with *in situ* PEGDA barriers between perfusion and cell culture channels, treated to reduce leaching of toxic resin components, and substrates from constantly flowing perfusion channels were delivered to cells through PEGDA barriers. In this device, *P. putida* KT2440 bacteria were successfully grown in the culture region for 44 h.

4.3 Experimental Materials and Methods

4.3.1 Chemicals

Clear Resin GPCL02 (Formlabs, Somerville, MA) was used for all devices. Phosphate buffered saline (PBS) (1× powder concentrate) and isopropanol (histological grade) were purchased from Fisher Scientific. Polyethylene glycol diacrylate (PEGDA, molecular weight:

700), polyethylene glycol methacrylate (PEGMA, molecular weight: 360), toluidine blue tracer dye (for microscopy, histological grade), and 2-Hydroxy-2-methylpropiophenone (HMPP, 97%) water soluble photoinitiator were purchased from Sigma-Aldrich. For microfluidic devices fabricated using soft lithography techniques, Sylgard 184 silicone elastomer kit (PDMS) was purchased from Dow Corning (Midland, MI). For manufacturing silicon master molds using photolithography methods, SU-8 2025 photoresist and SU-8 developer were obtained from Microchem (Newton, MA). Deionized (DI) water (resistivity ≥ 18.2 MX cm) was produced from a Direct-Q 3 UV Millipore ultrapure water system.

4.3.2 Bacteria strains and culture media

Plasmid pCMB55 was used to express *sfGFP* from the strong, constitutive promoter *Ptrc* in *Pseudomonas putida* KT2440 (kindly provided by Victor de Lorenzo of the Spanish National Center for Biotechnology, Madrid, Spain). Plasmid pCMB55 uses the pBBR1 origin and confers tetracycline resistance. Strains were grown in Lysogeny Broth (LB; 10 g/L tryptone, 5 g/L yeast extract, 10 g/L NaCl) for routine maintenance, and 21C Medium[117] at a 1× strength was used for overnight culture preparations of cells and for the substrate supplied for the long-term bacterial growth experiment. Saline solution 1× PBS (81% sodium chloride, 14% sodium phosphate dibasic, 3% sodium phosphate monobasic, 2 % potassium chloride) was used for washing and resuspending cells for the bacterial growth experiment. All broth cultures and microfluidic device inocula contained tetracycline (0.01 mg/mL) for plasmid maintenance and to help prevent contamination from any wild-type bacteria present in the laboratory environment.

4.3.3 Microdevice design and 3D-printing

3D-printed devices were designed using Solidworks 2015, a CAD software, then imported into PreForm software, and printed on a Form 2 stereolithography printer (Formlabs, Inc.,

Somerville, MA) at a resolution of 0.025 mm. The devices were printed upside-down at a 30° angle to allow uncured resin to drain from the hollow channel over the course of the print. CAD images and a photograph of a 3D-printed cell culture device can be seen in Figure 1. Flow channels within the device were designed with dimensions of 2 mm wide and 2 mm tall and devices also included barbed fittings designed to fit snugly with 1/8 inch tubing. The thickness for the solid cross-linked resin between the bottom of the open channel and the bottom of the device through which the cell culture region could be viewed on an inverted microscope was 0.5 mm to minimize added opacity in plate reader experiments. After printing, finished devices were placed in isopropanol (IPA) and each of the channels were cleared of uncross-linked resin by rinsing thoroughly with IPA using a wash bottle. Devices were then soaked in the IPA bath for approximately 30 min to remove any un-crosslinked resin, and then rinsed with fresh IPA within channels and on the exterior of the device, per manufacturer instructions. Devices were then allowed to dry in air and ambient room lighting for a minimum of 16 hours. Once an appropriate amount of drying time had been allowed, scaffolding supports were removed. If any remaining uncross-linked resin was observed after this step, channel interiors were once again rinsed with fresh IPA and devices were allowed to dry thoroughly in a chemical fume hood. The bottom viewing surfaces of the devices were wet sanded with 3200, 4000, 6000 and finally 12000 grit sandpaper and rinsed with MilliQ water. Acrylic cleaner was then sprayed on a piece of cork and the bottom viewing face of the device was polished on this surface; cleaning of the device was finished with a microfiber cloth. Any other rough edges left by supports on other portions of the device were sanded as needed.

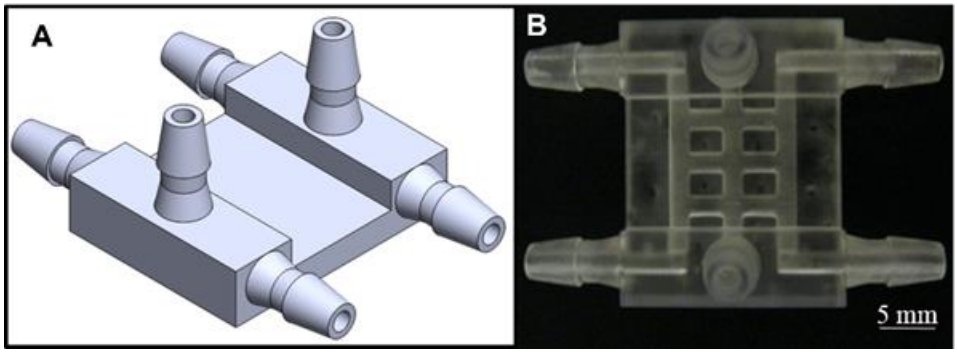

Figure 4-1. (A) CAD design of 3D-printed culture channel device and (B) photograph of printed device.

4.3.4 PEGDA barrier *in situ* photopatterning

PEGDA barriers were cross-linked and photopatterned *in situ* within a 3D-printed channel using methods adapted from techniques used to cross-link PEGDA within polydimethylsiloxane (PDMS) microfluidic channels.[98, 99, 112] A 20% v/v solution of PEGDA (MW 700) in water was prepared, and then the water soluble photoinitiator HMPP was added to a final concentration of 0.5% v/v. The PEGDA + HMPP solution was then vortexed to mix thoroughly. Plugs were prepared by fitting Tygon PVC tubing (1/8 inch internal diameter) with nylon barbed plug fittings which were used to cap each of the channel outlets. A cleaned and polished 3D-printed channel device was prepared as detailed in Section 2.3, and the empty device was placed in a plasma cleaner (Model PDC-32G, Harrick Plasma, Ithaca, NY) and exposed to oxygen plasma for 45 s; this process makes the interior channel surfaces hydrophilic to aid in filling the channels with the PEGDA solution. After plasma exposure, the channels were immediately filled with the 20% v/v PEGDA solution with 0.5% v/v HMPP by snugly fitting a 1 mL micropipettor tip into one of the middle channel outlets and pipetting in approximately 300-400 µL of solution. Preparation of the PEGDA solution and filling the device were both

completed inside a chemical fume hood because the PEGDA and HMPP chemicals are both somewhat volatile.

The prepared caps were then added to each of the channel outlet barbs and a photomask aligned on the flat bottom face of the device such that it would block UV light from reaching the flow channels and central culture channel, while allowing light to reach the cross-channels connecting them. The device was then exposed to high intensity UV light for 120 s using an Omnicure S2000 spot curing system (Excelitas Technologies, Mississauga, Ontario, Candada) set to 1 W/cm^2 and fitted with a collimating adapter to make the output intensity approximately 40 mW/cm^2. Both center plugs were removed and a 1 mL micropipettor was used to remove uncross-linked PEGDA from the center channel while filling it with air. The center plugs were replaced and this procedure was repeated with the left channel and then the right channel until PEGDA only remained in the cross-channels, with all other channels filled with air. To ensure all PEGDA was fully cross-linked, the device was once again exposed to UV light using the Omnicure at the same settings as above for 120s. After this final UV exposure, ultrapure water was pipetted into each of the previously air-filled channels.

4.3.5 Experimental and simulated tracer dye diffusion in water and hydrogel

In order to characterize and quantify the transport properties of the *in situ* photopatterned PEGDA barrier, the diffusivity of a tracer dye, toluidine blue, was measured through water-filled microfluidic channels and through PEGDA barriers patterned within a 3D-printed channel device.

4.3.5.1 Toluidine blue diffusion in water-filled microfluidic channel

PDMS microfluidic channels were fabricated using soft lithography casting techniques and master molds were constructed using photolithography methods, both of which have been describe in detail previously.[118] Briefly, a microfluidic master was fabricated on top of a silicon master using a negative photoresist, which is cross-linked in the desired microfluidic pattern using UV light and remaining photoresist removed. The optically transparent polymer PDMS was mixed with a cross-linking agent at a ratio of 10:1 polymer base to cross-linker and was poured over the master mold. The PDMS was cured at 60 °C and after 2-4 h the PDMS device was removed from the silicon master. This device was bonded to a clean glass slide by 45 s of oxygen plasma exposure and immediately filled with ultrapure DI water. This microfluidic device was designed to have three parallel main flow channels with dimensions of 100 µm wide and approximately 34 µm tall, connected by an array of smaller channels that were 20 µm wide by 200 µm long and 34 µm tall.

Two syringes were prepared, one filled with ultrapure water and the second filled with 1 mg/mL (or approximately 2.67 mM) toluidine blue (373.97 g/mol) and connected using tubing and barbed nylon fittings, one to each of the main flow channels on either side of the central channel. Outlet fittings and tubing were also attached to these left and right channels, and nylon plug fittings applied to the central channel outlets. These syringes were attached to separate syringe pumps (but the same model syringe pumps, to try and avoid any possible differences in flow settings), and the microfluidic device was placed on the observations stage of an inverted microscope (Zeiss AXIO-observer Z1 with AxioCamMRmRev.3 camera, Carl Zeiss Inc., Germany). Water was then flowed through the right flow channel at a rate of 20 µL/min and toluidine blue solution flowed through the left channel at a rate of 20 µL/min. The concentration

gradient of tracer dye was allowed to stabilize for 5-10 min, and an image was taken with the camera attached to the microscope, using brightfield imaging and a magnification of 5×. This procedure was repeated keeping the flow of water through the right channel constant, but decreasing the flow of toluidine blue solution in the left channel stepwise at the following flow rates: 18, 16, 14, 12, and 10 µL/min. These images were processed using ImageJ (version 1.50i, National Institutes of Health, USA) and results were compared to computational fluid dynamics (CFD) simulations of imported device channel geometries using COMSOL Multiphysics 5.2 (Burlington, MA).

4.3.5.2 Toluidine blue diffusion in patterned PEGDA barrier

Diffusivity results for toluidine blue in water obtained from the PDMS microfluidic channel were compared to transport of toluidine blue dye through PEGDA barriers photopatterned within a 3D-printed channel. The same device and preparation protocol was employed for this experiment as detailed in Sections 2.3 and 2.4. Figure 2(A) contains a schematic for the experimental set up. After PEGDA barriers were constructed within cross-channels and the device filled with water, right and left channel inlets were attached via Tygon PVC tubing to syringes filled with ultrapure DI water and 1 mg/mL toluidine blue solution in water respectively; the central channel inlets and outlets remained capped. Using two syringe pumps, for this portion of the experiment the flow rate of toluidine blue solution in the left channel was 100 µL/min and the flow rate of water in the right channel was 100 µL/min. A Dino-Lite Edge 5MP AM7115 Series Digital Microscope (BigC, Torrance, CA) equipped with a diffuser cap was used to capture time-lapse images of toluidine blue diffusing through the PEGDA during the testing period. These images were processed using ImageJ and results were compared to CFD simulations of imported device channel geometries using COMSOL Multiphysics 5.2.

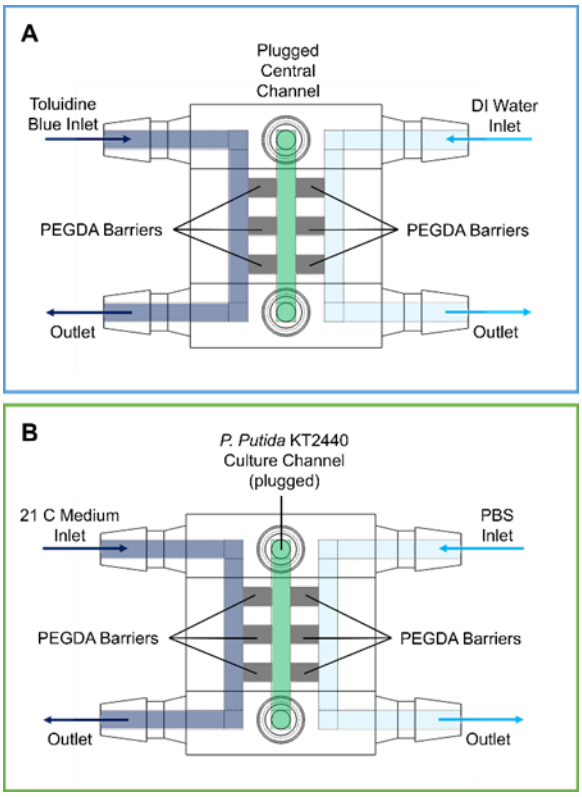

Figure 4-2. Schematics of 3D-printed channel device, illustrating where PEGDA barriers were constructed *in situ* in cross-channels connecting the flow and culture channels. (A) Schematic of setup for toluidine blue tracer dye transport experiment detailed in Materials and Methods Section 2.6 and Results and Discussion Section 3.3. (B) Schematic of setup for long-term cell growth experiment detailed in Materials and Methods Section 2.7 and Results and Discussion Section 3.4.

4.3.6 Image analysis for toluidine blue concentration

For each of the experimental images obtained using the procedures described in Section 2.6, relative toluidine blue concentrations were calculated by analyzing photographs using ImageJ software. First, each photograph was converted as needed from a color JPEG into an 8-bit greyscale image, where the grey value could be correlated to toluidine blue concentration. In order to normalize the image, the grey value was measured at five points in the channel where there was no toluidine blue present (this was done in the opposite PEGDA barrier for the 3D-printed device, since the PEGDA hydrogel was slightly lighter than water-filled channels) to determine the value for a concentration of 0, and in the toluidine blue flow channel to find the

maximum concentration value. Next, cross-sectional lines were drawn in ImageJ across the region of interest, and the grey values were plotted along the length of this line. These values were then normalized using the minimum and maximum values obtained previously. Additionally, scale bars or channel features with a known length were measured in ImageJ to enable conversion from pixels to microns.

4.3.7 Bacterial culture preparation

Stationary phase *P. putida* KT2440 cultures were prepared by combining 3 mL of 1× strength 21C Medium plus 0.01 mg/mL tetracycline and a freezer stock inoculate or individual colony from a plate in a 15 mL loosely-capped culture tube; these cultures were incubated an orbital incubator at 30 °C and 120 RPM for approximately 20-24 h. 21C Medium was chosen for this application because exhibits markedly lower autofluorescence when compared with complex media such as LB or Tryptic Soy Broth. After the allotted time, culture tubes were removed from the incubator, thoroughly vortexed, and 1 mL of cell culture was washed three times (21,000 RCF for 1.5 min) and resuspended in 1× PBS saline solution with 0.01 mg/mL tetracycline. Washed cultures were adjusted to an OD 600 of ~0.05 (Synergy HT plate reader, BioTek, Winooski, VT).

4.3.8 Long-term cell culture perfusion experiments

Two identical devices with in-plane PEGDA membranes were prepared as described above, then pre-treated to minimize biotoxicity. Perfusion channels and the central culture chambers were flushed with ultrapure DI water for 16 h at a flow rate of 50 µL/min to leach labile resin and photoinitiator from the printed resin. Inlets and outlets were capped and the water-filled device was exposed to 30 mW/cm^2 UV light for 120 s in an ELC-500 UV curing chamber (Electro-Lite Corp., Bethel, CT) to promote further resin cross-linking.

Figure 2(B) is a schematic of the experimental set up and perfusion flow scheme described below. After the device was exposed to UV, the water was removed from all channels using a 1 mL micropipettor and replaced with PBS containing 0.01 mg/mL tetracycline in left and right perfusion channels. Inlets and outlets of the perfusion channels were then capped. The central culture chamber of one device was loaded with 200 µL stationary-phase *P. putida* KT2440 prepared in PBS as described previously. No cells were added to the central well of the second device, and instead the central chamber was filled with PBS + tetracycline. Inlets and outlets of the central chamber were capped, and both devices were mounted to a glass slide with added microscope immersion oil to improve clarity, and placed within a control chamber on an inverted microscope. For each device, one channel was perfused at 10 µL/min with 21C media + 0.01 mg/mL tetracycline and the other perfused at 10 µL/min with PBS + 0.01 mg/mL tetracycline via syringe pump in a single-pass configuration for 44 h.

4.4 Results and Discussion

4.4.1 Confirming diffusivity of tracer dye in water phase

To eventually characterize transport of toluidine blue tracer dye through the PEGDA barrier, the diffusivity of the dye in water was first confirmed by comparing experimental data in a liquid-filled microfluidic channel with COMSOL Multiphysics CFD simulations. Toluidine blue dye was chosen because at a molecular weight of approximately 373 g/mol, it is on the same order of magnitude as glucose at approximately 180 g/mol. Glucose and other similarly-sized sugars are common carbon substrates that would need to diffuse through the PEGDA barrier for delivery to cells in a variety of culture applications; if diffusion of toluidine blue can be characterized through the PEGDA barrier, this can be used to model and predict diffusive delivery of other similar molecules. Additionally, toluidine blue can be viewed without

fluorescence microscopy in the larger 3D-printed channel and is dark enough to be visible inside smaller microfluidic channels at low concentrations where Fickian diffusion assumptions can be made.

A diffusion coefficient of 1.42 x 10^{-5} cm^2/s was obtained from literature, where it was calculated theoretically using the Stokes-Einstein equation.[119] This value was input into the COMSOL Multiphysics model using the microfluidic geometry as shown in Figure 3, with channel measurements detailed in Section 2.6; a 3D-geometry was chosen for this simulation to best model the no-slip conditions and other characteristics of microfluidic flow. Water was flowed through the right channel of the device at 20 µL/min and a solution of 1 mg/mL toluidine blue (or approximately 2.67 mM) was flowed through the left channel at 20, 18, 16, 14, 12, and 10 µL/min in COMSOL simulations and in experiments.

Toluidine blue concentration as observed in experimental bright field microscope images is compared with images of COMSOL simulation outputs in Figure 3 (A,B) for the condition of 20 µL/min flow on both sides. All other flow rate combinations are shown in Supplemental Figure S-1. In part (C) of Figure 3, a plot is shown for experimental data processed using ImageJ with COMSOL simulation concentrations at each of the cross-sections indicated in part (A). By comparing simulated versus measured concentrations (Fig 3C), we conclude the model adequately represents the data and that a diffusivity of 1.42 x 10^{-5} cm^2/s is appropriate.

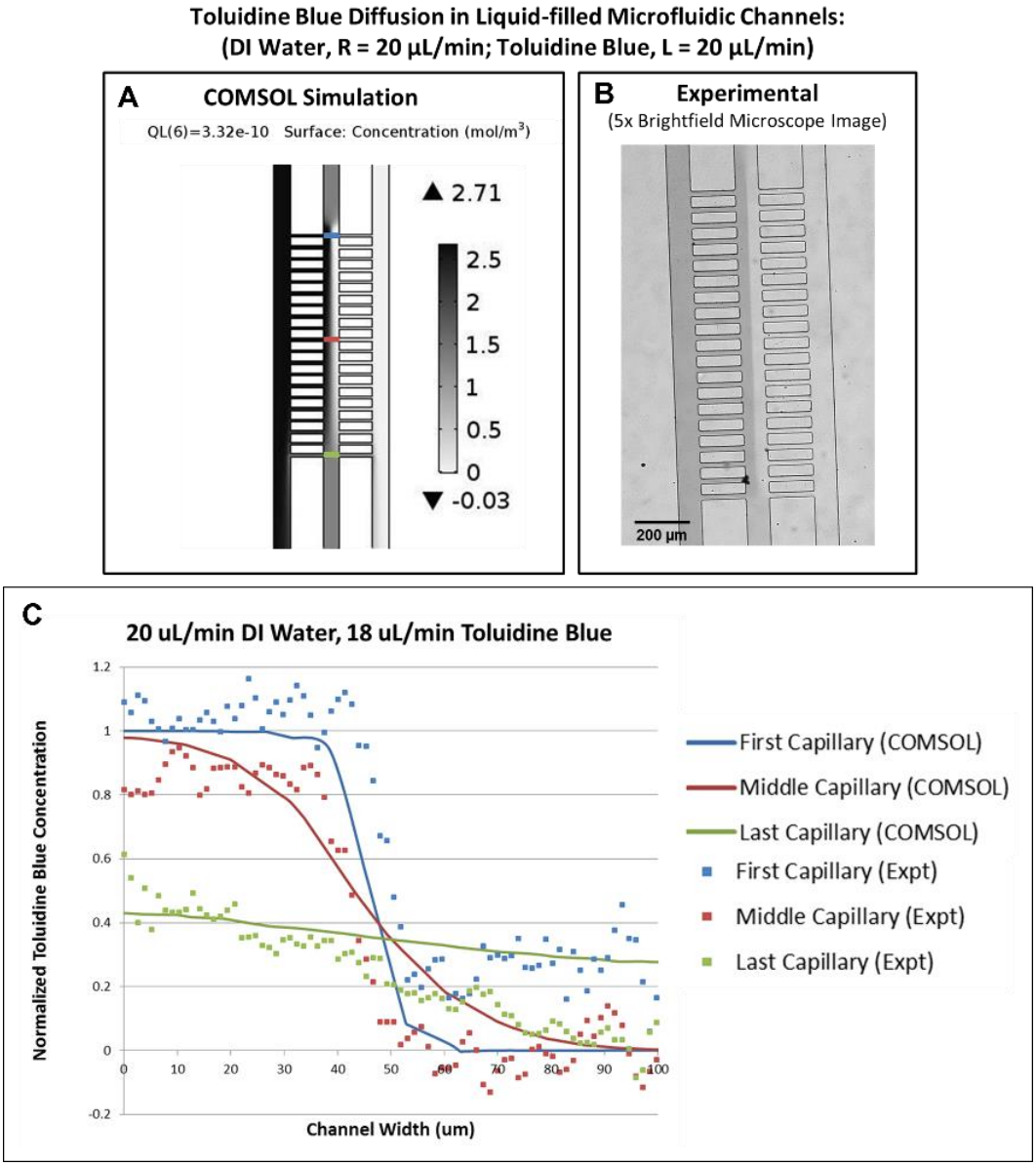

Figure 4-3. (A) COMSOL Multiphysics 5.2 CFD simulation of toluidine blue diffusion, assuming Stokes-Einstein Equation calculated value for diffusivity of 1.42 x 10^{-5} cm^2/s, compared to (B) experimental image at the same combination of flow rates with 20 µL/min flow in both left and right channels. Blue, red, and green line locations in (A) correspond with plot in (C), showing the fit between the experimental image analysis data with COMSOL predictions for a flow condition of 20 µL/min DI water on the right with 18 µL/min 1 mg/mL toluidine blue solution flowing on the left.

4.4.2 Using tracer dye to characterize PEGDA barrier transport properties

The diffusivity of toluidine blue in liquid water was next compared to the effective diffusivity of the dye through PEGDA barriers photopatterned within a 3D-printed channel device.

4.4.2.1 Experimentally-measured diffusivity of toluidine blue in PEGDA barriers

The PEGDA barriers were constructed in the 3D-printed channel and the flow configuration was set such that 2.67 mM toluidine blue solution was flowed through the left channel and DI water was flowed through the right channel, both at a rate of 100 µL/min; the center channel was plugged to prevent flow. Time-lapse photographs were taken over the course of 4 hours and experimental images were analyzed in ImageJ using the method described previously. From this analysis, normalized toluidine blue concentration could be plotted relative to position along the PEGDA barrier.

In Figure 4, part (A) shows experimental photographs of the toluidine blue diffusing through the PEGDA barriers. In these images, flow inlets are at the top of the picture and outlets are at the bottom. The PEGDA barriers can be clearly seen as the more opaque and whiter regions in the cross-channels. With increasing time, the toluidine blue tracer dye advances across the PEGDA barrier until it reaches the central cell culture channel between 3 and 4 h.

By inspection, it appears that this diffusion occurs uniformly within each of the barriers and also occurs uniformly when comparing the first, middle, and last cross-channels. In the liquid-filled microfluidic channels of Figure 3, flow occurred through the cross-channels and into the center channel (Supplemental Figure S-2), which caused different concentration gradients along the length of the center channel. Since this does not occur in the 3D-printed device with PEGDA barriers, this suggests that the hydrogel impedes flow between the culture chamber and the perfusion channels. This was next confirmed by comparing experimental values to theoretical values calculated assuming no flow and later to simulated toluidine blue concentrations with and without flow through the barrier regions.

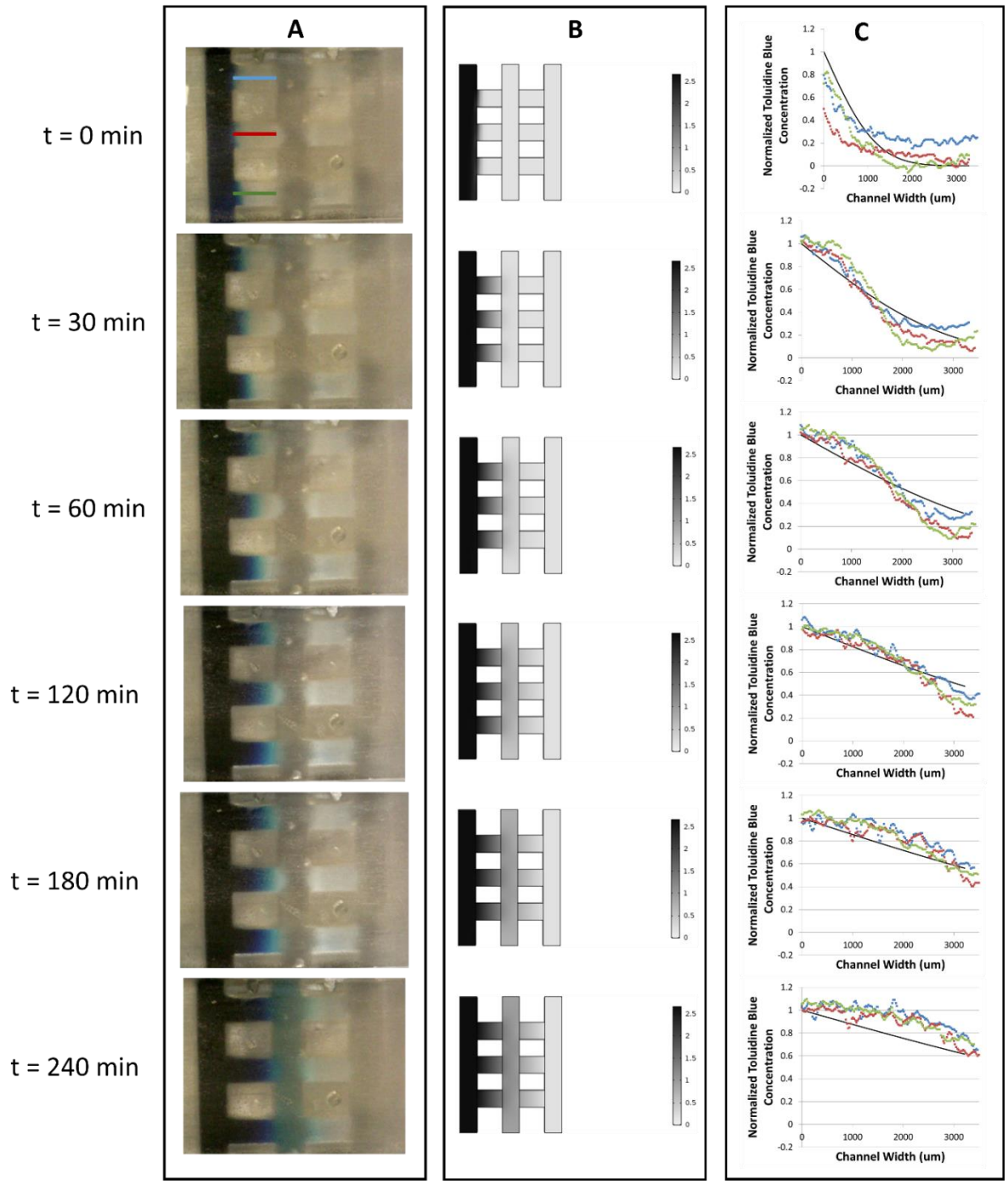

Figure 4-4. Images of (A) toluidine blue tracer dye diffusing through PEGDA hydrogel barriers cross-linked *in situ* within the 3D-printed channel device at various time points with flow rates of 100 µL/min of both toluidine blue (left) and DI water (right); (B) toluidine blue concentration outputs for COMSOL simulations the same inlet flow values as the experiment, assuming no flow occurs in the PEGDA barrier and that the diffusivity of toluidine blue is 1.42 x 10^{-5} cm^2/s throughout; and (C) plots of normalized concentration values from images in (A) analyzed using ImageJ software, where the colors of the points correspond with the cross-sections shown in the top device in (A), and the theoretical calculated normalized concentration, assuming 1D-unsteady state Fickian diffusion.

4.4.2.2 Theoretical model of 1D toluidine blue diffusion in water approximates experimental data values at PEGDA boundaries

We first compared the experimental data to the theoretical values calculated assuming toluidine blue transport through PEGDA barriers could be modeled as unsteady 1D Fickian diffusion. The differential equations that describe this behavior and their solution is described in Cussler.[120] First, beginning with Fick's second law such that:

$$\frac{\partial c}{\partial t} = D\frac{\partial^2 c}{\partial z^2}$$

Where c is toluidine blue concentration, t is time, z is distance along the PEGDA barrier, and D is the diffusivity of toluidine blue, which was assumed to be independent of concentration. The boundary conditions are defined as follows:

At $t = 0$, for all z, $c = c_\infty$

At all $t > 0$, at $z = 0$, $c = c_0$ and at $z = \infty$, $c = c_\infty$

We assume $z = 0$ at the initial left-side boundary of the PEGDA barrier, that the normalized $c_0 = 1$ (maximum toluidine blue), and that the normalized $c_\infty = 0$ (no toluidine blue).

This secondary differential equation is solved by combination of variables, so z and t are combined into the following variable:

$$\xi = \frac{z}{\sqrt{4Dt}}$$

Next, the differential equation is rewritten in respect to this combined variable, and can be integrated twice using the previously determined boundary conditions to arrive at the final solution:

$$\frac{c - c_0}{c_\infty - c_0} = erf\xi$$

Where erfξ is the error function of the combined variable. This equation was then solved for c to get a calculated toluidine blue concentration for a given time and location, with an assumed diffusivity value, and compared to the experimental normalized concentrations.

Part (C) of Figure 4 plots experimental data with theoretical calculations for the various time points listed. The blue, red, and green data points are the experimental values of normalized toluidine blue concentration along the length of the PEGDA barrier cross-section. The locations of these cross-sections correspond with lines shown in the annotated picture in part (A). The black line is the theoretically calculated value assuming the same diffusivity of toluidine blue in PEGDA as liquid water, 1.42 x 10^{-5} cm^2/s. Comparing these experimental and theoretical plots, one can observe that the assumption of 1D Fickian diffusion with no flow is a relatively accurate prediction for the experimental toluidine blue concentration values at the boundaries of the PEGDA barrier.

It is useful to know that the same toluidine blue diffusivity in water can be used to approximate transport in PEGDA barriers. It is likely this is the result of the hydrogel structure; since the cross-linked matrix is still primarily water, molecules smaller than the cross-linked mesh size are able to diffuse through the hydrogel relatively unimpeded. Therefore, transport of other smaller molecules through the PEGDA barrier could be calculated using theoretical 1D Fickian diffusion equations and assuming diffusivities equivalent to those in liquid water. Using this method, delivery of sugars, salts, or oxygen to cells near the PEGDA boundary could be predicted in a cell culture application.

However, there is a slight difference in the trends of the experimental and theoretical concentration gradients within the PEGDA barrier. A possible inflection point is observed in the experimental data, but is not present in the theoretically calculated line.

4.4.2.3 COMSOL simulations suggest PEGDA barriers impede fluid flow

The differences in the experimental and theoretical concentration gradients may have been caused by a very small amount of flow through the PEGDA barrier from the perfusion channels next to it. This may result in a system with facilitated diffusion, rather than passive diffusion of toluidine blue through the PEGDA.

To investigate this, COMSOL CFD simulations were conducted both with and without flow in the cross-channels. For the COMSOL Multiphysics simulations, similar to the liquid-filled microfluidic device described previously, the geometry of the 3D-printed channel was constructed in the software, where laminar flow and dilute species transport assumptions were made. COMSOL simulations with flow in the PEGDA barriers did not agree at all with the experimental data, showing a much shorter time for the toluidine blue to reach the central culture channel, under 15 min for the top barrier region, and uneven transport through the first, middle, and last barrier regions (see Supplemental Figure S-3A).

COMSOL simulations where no flow was allowed in the PEGDA barrier region much more closely resembled experimental data. COMSOL simulation results showing the toluidine blue concentration from a cross-section in the middle of the channel can be seen in part (B) of Figure 4. The scale shown is such that black = 2.67 mM, or the maximum toluidine blue concentration, and white is a toluidine blue concentration of 0 mM. When comparing the simulation and experimental results side-by-side, a slight difference can be observed, such that

the concentration gradient along the front of advancing dye appears to be steeper experimentally than it is in the simulation. Simulation values closely matched the 1D-diffusion theoretical calculations when plotted, so it is believable that there is some difference observed between the experimental images and COMSOL simulations (see Supplemental Figure S-3B). Therefore, while it is possible that a small amount of flow may occur within the PEGDA barrier as evidenced by the slight inflection points observed in the experimental plots, COMSOL simulations suggest that this flow is very minute, if present at all.

4.4.2.4 Summary of experimental transport vs. calculated and simulated values

Comparing the experimental data to theoretical calculations and COMSOL Multiphysics CFD simulations, it can be concluded that an effective diffusivity of 1.42×10^{-5} cm^2/s, or the same value for toluidine blue in water, can be used to approximate unsteady-state diffusion through PEGDA barriers. Any small amount of flow that may be present in the hydrogel does not appear to greatly affect either the time it takes for toluidine blue to reach the far boundary of PEGDA and deliver it to the culture channel (Figures 4A and 4B) or the values at that boundary (Figure 4C). Simulating flow through a visco-elastic material like a PEGDA hydrogel in COMSOL would be very complicated. If the transport of such molecules through PEGDA can be fairly accurately calculated using much simpler 1D diffusion equations with no flow, that is a significant conservation of time and effort. These findings suggest it could also be assumed that molecules up to the size of toluidine blue have effective diffusivities comparable to their values in water. This is likely because the hydrogel is still primarily water and the pore size between cross-linkages is large enough that it doesn't impede smaller molecules. If this is valid, one can fairly accurately predict the transport of a whole range of molecules through the PEGDA barrier to cells in the center culture channel.

4.4.3 Long-term cell culture in 3D-printed channels

Lastly, a proof-of-concept was conducted to test whether a substrate could be delivered through a PEGDA hydrogel barrier within a 3D-printed device to sustain cells in the center culture channel for multiple days.

Robust *P. putida* KT2440 bacteria were chosen for this application. This bacterial strain is able to withstand exposure to carbon compounds that may be toxic to more sensitive cells in bioremediation applications, [84, 85] so we reasoned they would best be able to withstand any possible leaching of monomer, oligomer, or photoinitiator from the 3D-printed device.[84, 85] Nonetheless, steps were taken to thoroughly rinse the device and expose it to additional UV light prior to adding bacteria to mitigate as much leaching as possible.

This device was loaded with bacteria in the center culture chamber and 21C Medium was flowed through one of the perfusion channels to serve as a substrate source for the cells (Figure 2B). PBS saline solution was flowed through the opposite perfusion channel to act as a diffusive sink; this served as the driving force for diffusive flux of substrate and removal of certain cell waste products. Both media and saline solutions were perfused at a flow rate of 10 µL/min, enough to completely refresh that particular flow channel approximately 1× every 6 min. The GFP-producing *P. putida* KT2440 bacteria fluoresced green and were imaged using fluorescence microscopy over approximately 44 h. Additionally, a control with no bacteria was conducted in an otherwise identical device with the same flow configuration and imaged concurrently.

Figure 5 shows results from this testing at the various time points. The images in part (A) show a zoomed-in view, indicated by the white dotted boxes in the larger views below, from 0-44 h. The increasing fluorescence intensity over time in the device containing bacteria cells can

be observed in the top row. Meanwhile, fluorescence intensity of the liquid in the control remained constant over the whole 44 h. Larger views in part (B) further illustrate this point, confirming that fluorescence in the central channel is not being caused by the culture medium or PBS saline solution. The PEGDA barriers can also be observed in these images, as they seem to fluoresce slightly more than the liquid streams as well. It should be noted that the 3D-printed resin does autofluoresce to a certain degree, so that is why the region around the channels is not entirely dark.

Locations of higher fluorescence intensity, and therefore higher bacteria cell concentration, can be observed at the PEGDA boundaries on the side of the media perfusion channel, as indicated by the white arrow. This is the point at which the substrate concentration in the cell culture chamber is the highest and oxygen is also able to diffuse through the barrier from the media perfusion channel. Cells likely congregate at this boundary because fresh substrate and oxygen is constantly being supplied at this boundary. Furthermore, the fluorescence intensity of the cells at the left PEGDA barrier boundaries increases between 22 and 44 h, indicating the cells are still growing and producing GFP during this extended time period. A dimmer band can be seen on the opposite (right) side of the cell culture channel, at the boundary of the PEGDA barrier; the cells may be localized at this region because of the oxygen diffusing from the freshly flowing saline perfusion channel, but are dimmer because substrate concentration is not as high as on the media perfusion channel side. Lastly, no cells are seen infiltrating the PEGDA hydrogel, so it would appear this barrier is able to successfully limit motility and keep cells within the center channel.

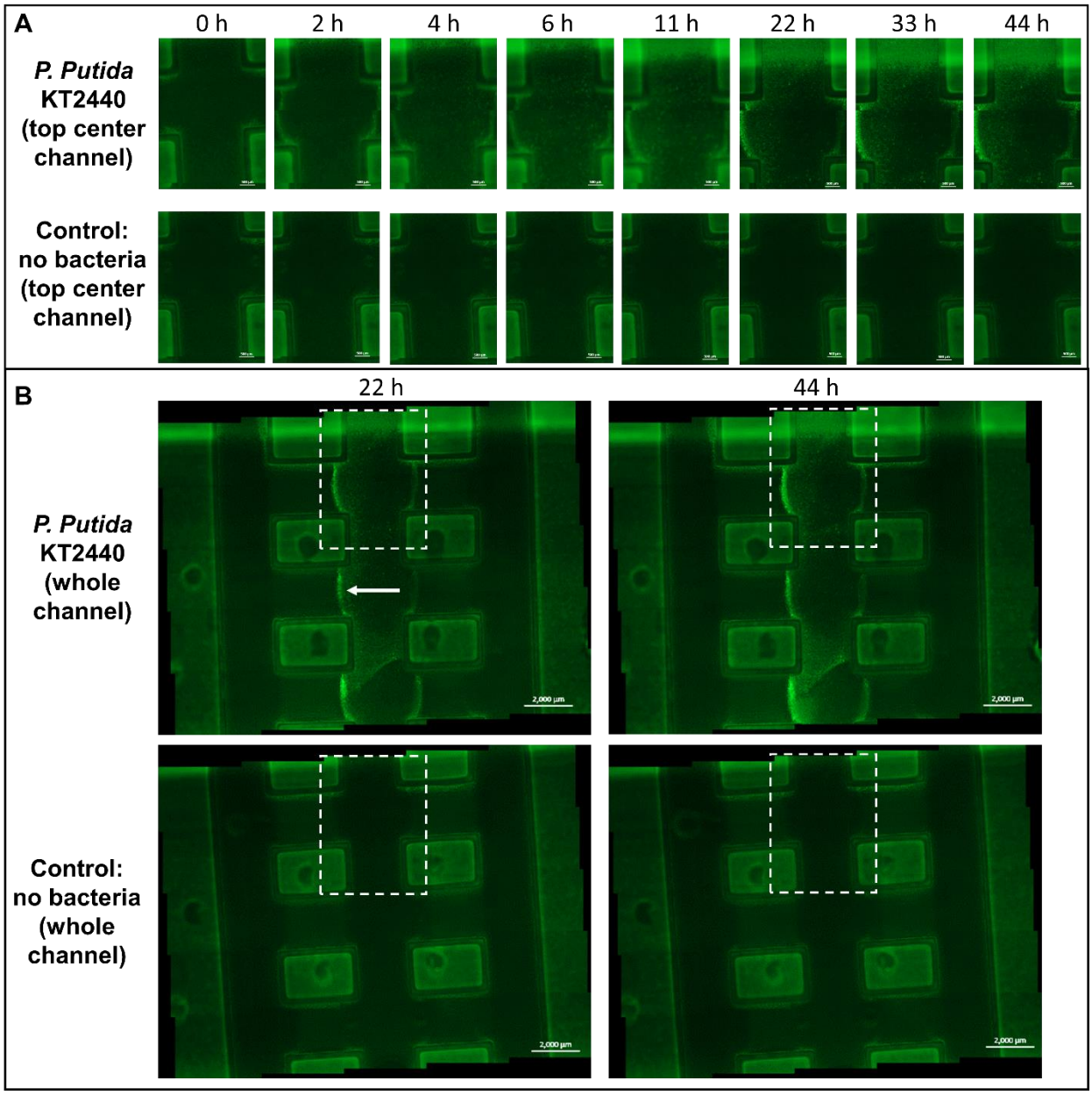

Figure 4-5. Images of cell culture channels with *P. putida* KT2440 growing within the central channel of the device and a control device with no bacteria over a time period of 44 h. White boxes in (B) indicate the approximate zoomed-in area shown in (A). The PEGDA hydrogel barriers can be observed as a slightly brighter section in the cross channels, as opposed the flow and culture channels. The white arrow indicates high concentrations of the *P. putida* KT2440 at the PEGDA boundaries where the components of the 21C media along with oxygen are diffusing through to the culture region. As mentioned previously, this bacteria expresses a GFP plasmid, allowing it to be visualized using fluorescence microscopy. These are tiled images taken at 2.5x magnification with 470 nm excitation at a 1000 ms exposure time; all channel widths are 2 mm with a height of 1 mm, and the scale bars at the lower right in the whole channel pictures are 2 mm. For the images of the entire channel, individual image tiles were automatically aligned in Zen processing software.

4.5 Conclusion

In this work, PEGDA hydrogel barriers have been fabricated *in situ* within an STL 3D-printed channel and used to successfully deliver substrates to maintain bacteria cells over an extended culture time. To the authors' knowledge, this has not been demonstrated previously in literature. With steps taken to rinse and further cross-link any monomer, oligomer, or photoinitiator that may not have been fully removed from the printed device after production, these bacteria were able to survive and grow over the course of 44 h. Additionally, with adequate polishing and by viewing the channel through immersion oil, these fluorescent bacteria were able to be imaged with a high enough resolution that localization of cells at hydrogel boundaries could be observed. Although there is much improvement to be made with microscopy in 3D-printed channels, this incremental step may be useful considering how this has been a limiting factor for many biological imaging applications. Lastly, cells were observed congregating near PEGDA boundaries where substrate and fresh oxygen were delivered to the culture channel, which suggests that these hydrogels were able to successfully transport the molecules of interest to cells.

Transport of the tracer dye toluidine blue could be approximated using theoretical 1D unsteady Fickian diffusion equations and could be simulated in COMSOL Mutiphysics, a CFD software. We found that the effective diffusivity of this tracer dye was the same as it was in water, which is likely because the hydrogel matrix is still primarily water and the pore size between cross-linked polymers is large enough that the toluidine blue molecule is not hindered. This could be useful for predicting delivery of other small molecules through similarly constructed PEGDA barriers. Additionally, methods for characterizing the transport properties of this PEGDA barrier could be repeated with larger tracer dye molecules to better understand the

diffusive behavior of proteins or with hydrogels with different cross-link densities to develop barriers with a range of delivery capabilities.

Ultimately, as Figure 6 shows, to have a better response time and allow faster diffusive transport, decreasing the length of the barrier while increasing the cross-sectional area over which molecules can diffuse would be needed. Additional work can be done to investigate and further characterize the interactions between the PEGDA and 3D-printed resin, and surface-modified PEGDA could be incorporated the strength of the bond if needed.

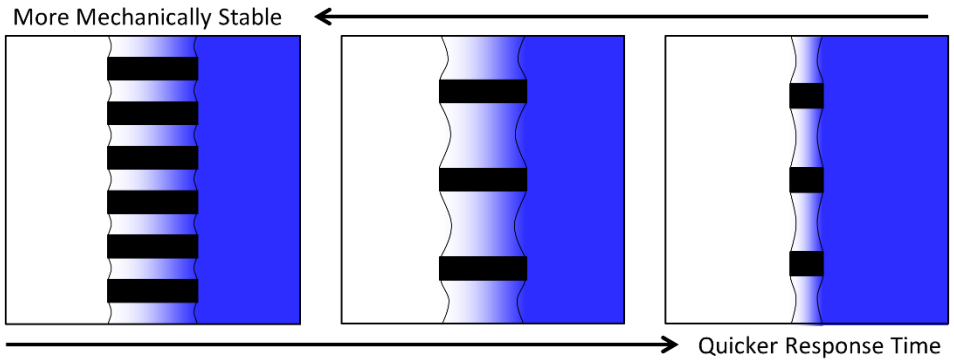

Figure 4-6. Schematic illustrating the advantages of having thinner hydrogel barriers for quicker response time to changing stimuli, in addition to taking less time to establish a stable gradient across the hydrogel barrier. Larger spaces between post supports also allow for a larger cross-sectional area for diffusive flux of species that can be delivered to cells.

4.6 Supplemental Information

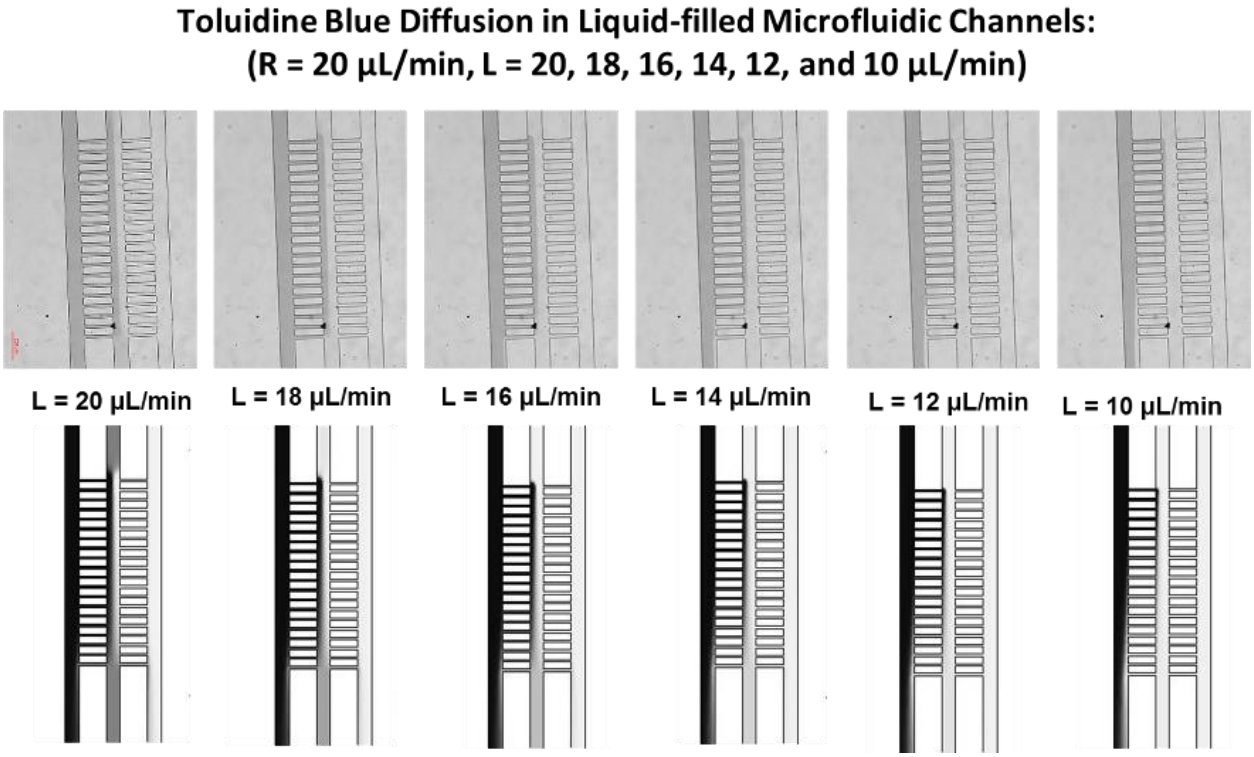

Figure 4-7(S-1). Comparison of experimental images of toluidine blue diffusion experiment (top row) with the corresponding COMSOL model outputs (bottom row).

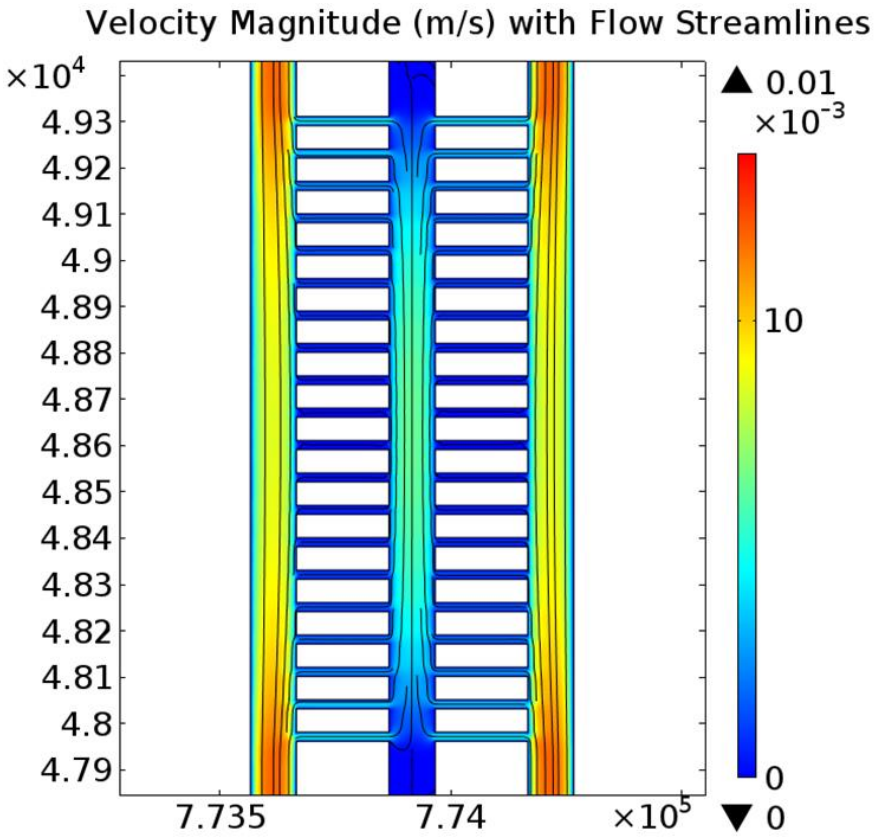

Figure 4-8(S-2). Velocity profile in liquid-filled microfluidic flow channel for toluidine blue diffusion. The color scale indicates the velocity magnitude in m/s and the lines are flow streamlines. This image is from the COMSOL simulation with 20 µL/min flowing in each of the left and right channels.

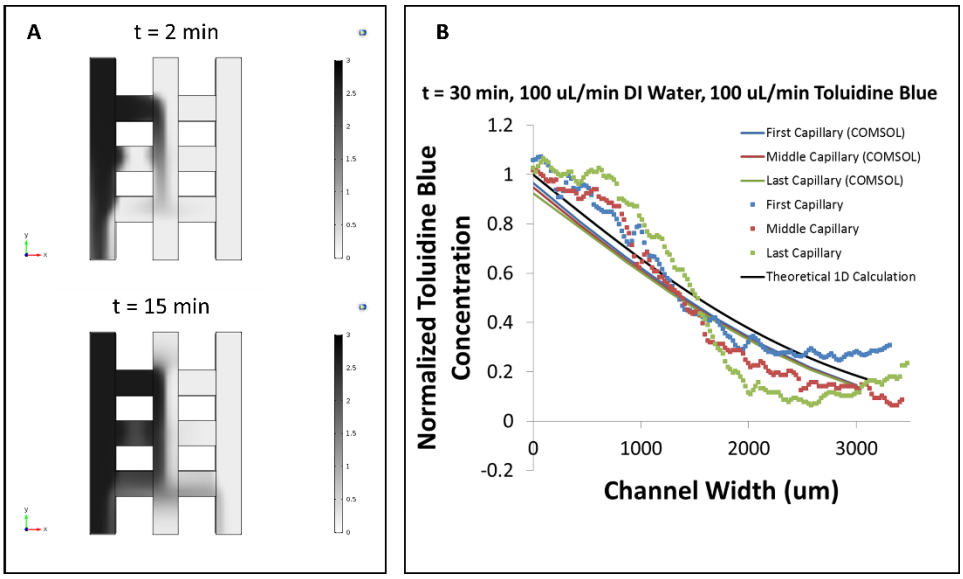

Figure 4-9(S-3). (A) Simulated toluidine blue concentration (COMSOL Multiplysics) if flow is allowed in the cross-channel regions. (B) Experimental, theoretical, and simulated values for normalized toluidine blue concentration in top, middle, and last cross-channels, showing COMSOL simulations closely match theoretical calculations.

5 Conclusion

5.1 Dissertation Overview

In this dissertation, several novel advanced manufacturing and microfabrication methods were developed to improve control of microenvironments for microbial cell culture. The goal was to develop these techniques so they could be used to create a synthetic hindgut-on-a-chip device. This device would replicate the conditions found within the digestive tracts of termites to culture the symbiotic microbial community inside. The microbiome inhabiting the termite gut enables the insect to very efficiently break down lignocellulosic materials into chemicals such as acetate and hydrogen.[33, 35] Therefore, if this microbiome could be successfully cultured outside of a living termite and eventually scaled up, it could be useful in converting woody agricultural wastes into carbon-neutral biofuels like acetate, hydrogen, and methane.[36]

However, many hurdles existed for reproducing the microenvironment found within the termite gut. The lower termite *Reticulitermes flavipes* has been investigated in the large interdisciplinary National Science Foundation project funding this dissertation work in large part because it contains one of the more diverse microbiomes out of the many termite species. Microbes from Bacteria, Protista, and, Archea kingdoms are all represented in the guts of *R. flavipes*, where each species performs a particular role in the metabolic degradation of the lignocellulose.[35] Furthermore, the microbiome contains both facultative aerobes that can utilize oxygen, and anaerobes that cannot survive even in low oxygen concentrations. In the termite hindgut, this results in an oxic region extending approximately 200 μm into the hindgut from the exterior wall where aerobic microbes are localized and an anoxic interior with little to no oxygen occupied by anaerobes.[35, 37]

Faithfully reproducing this oxygen gradient in a synthetic device is not trivial. One portion of this dissertation work focuses on a method to fabricate gold microelectrodes *in situ* within a microfluidic channel. At the surface of these electrodes, water could be split to produce oxygen that could then be delivered to microbes in a hindgut-on-a-chip device. A novel technique incorporating surface chemistry and photopolymerization was developed to pattern the gold electrodes along the side-walls of the microfluidic channel. However, this procedure was relatively time-consuming and complicated, and presented difficulties during integration with fluorescent oxygen-sensing films that would be used to measure microoxygen concentrations. Because of these issues, a simpler method was developed to use oxygen and nitrogen saturated liquid water streams to establish an oxygen gradient for termite microbes in initial test devices.

Additional advancements were made in culturing microbial cells within a 3D-printed millifluidic channel. While there are many advantages to performing lab-on-chip testing in traditionally-used polydimethylsiloxane (PDMS) channels, the photolithography and soft lithography techniques required to fabricate devices this way require a high degree of expertise and expensive clean room equipment. These disadvantages make the use of microfluidics in many biological applications cost-prohibitive, and many biologists who would be the end users of such technology do not have the engineering experience to fabricate devices themselves. Therefore, using 3D-printing to manufacture cell culture devices was investigated as an option for making micro- and millifluidic technology more accessible to users with a wide range of backgrounds.

The work detailed in this portion of the dissertation first focused on testing and improving the biocompatibility for a commonly-used stereolithography 3D-printer resin with bacteria cells, which had not been done previously. An adverse dose response of bacteria to increasing levels of

untreated 3D-printed resin was observed. Therefore, treatment methods were developed to rinse out and further cross-link in place oligomer, monomer, and photoinitiator that remained in the resin piece after printing. Significant improvements in cell survival were observed with this treatment method. These findings were incorporated into a proof-of-concept device constructed to culture bacteria cells over an extended period of time. Additionally, a hydrogel barrier was developed that could be photopatterned *in situ* within the 3D-printed cell culture device. This semi-permeable barrier allowed diffusive delivery of oxygen and carbon substrates from flowing perfusion channels to cells in a no-flow liquid culture. This cell culture device was treated to reduce chemical leaching from the 3D-printed resin and constructed with hydrogel diffusion barriers. Bacteria cells were successfully grown inside the device for 44 h, which had not been previously accomplished in the published literature.

5.2 Summary of Findings

In Chapter 1, a discussion of the motivation provides a larger context for this dissertation project and detailed research objectives are listed.

Chapter 2 introduces a method to selectively pattern gold microelectrodes on the sidewalls of a PDMS microchannel. The aim of the microelectrodes was to supply oxygen at tunable microoxic concentrations to cells within a cell culture device. Although this method was ultimately not used for oxygen generation in current iterations of hindgut-on-a-chip devices, this work still made relevant advancements in fabrication techniques available to microfluidics researchers. The following are the major contributions and key findings of Chapter 2:

1. Development of a novel method for combining surface chemistry techniques with photopatterning to selectively bond gold onto vertical side walls of a PDMS

microchannel, rather than just on the bottom surface of the channel as researchers had previously accomplished.

   a. ATR-FTIR analysis determined gold was being chemically bonded to the PDMS surface, unlike other physical patterning methods such as sputtering or etching.
   b. Deposition of gold on the PDMS microchannel side walls was confirmed by SEM/EDX imaging and electrochemical analysis.

2. Development of a COMSOL Multiphysics simulation investigating the effect of microelectrode geometry on the electric potential gradient.
   a. According to simulations, electrodes located on microchannel side walls created an electric field that was uniform with depth at all points within the channel.
   b. Simulated electrodes deposited on the bottom substrate resulted in a 10-40% decrease in electric potential vertically along the microchannel side wall.

Chapter 3 details experiments conducted to both test and improve the biocompatibility of a proprietary 3D-printed resin formulation used by Formlabs stereolithography printers. While we had identified 3D-printing as a promising technology for producing the cell culture channels for the termite microbiome, much was still unknown about the effect of 3D-printed resins on microbes. This work sought to quantify any biotoxicity effects of 3D-printed resin on the model bacteria chosen. The species chosen were the sensitive lab strain *E. coli* XL1B and a more robust strain of bacteria used in bioremediation applications, *P. putida* KT2440. The following are the major contributions and key findings of Chapter 3:

1. Two adaptable assays were developed to test the effect of 3D-printed resins on cell growth and viability.
    a. Growth curves were conducted in a 48-well plate format to enable real time measurements of cell growth and 3D-printed disks were fit into the bottoms of wells to test cell responses.
    b. A dose-response assay was designed to quantify the number of viable cells remaining at different doses of 3D-printed resin and different resin treatment methods.
2. A spectrum of biotoxicity effects were caused by contact with untreated 3D-printed resin during active cell growth.
    a. *P. putida* KT2440 exhibited few adverse effects to the 3D-printed resin, no matter the treatment, in active growth experiments.
    b. *E. coli* XL1B was much more sensitive to 3D-printed resin, and doubling times were increased 2-4x when comparing cells exposed to resin with all treatment types to control cells that had no resin exposure.
3. A dose response was observed to untreated resin for both *P. putida* and *E. coli*; again this was more pronounced in the *E.coli* cells, which experienced 1-3 orders of magnitude reduction in viable cells after 24 h of exposure to resin with increasing resin dose.
4. Methods were developed that were able to significantly reduce the biotoxicity of the 3D-printed resin at a variety of doses by removing or further cross-linking monomer, oligomer, and photoinitiator in the polymer matrix of the printed resin. Washing printed resin in water, drying at 60 °C, and additional UV exposure was

able to improve *E. coli* cell viability counts in the dose-response assay, such that they were statistically indistinguishable from control cells with no resin exposure.

Chapter 4 takes the knowledge obtained from the biocompatibility testing of Chapter 3 and uses this to construct a 3D-printed cell culture device to grow bacteria over an extended period of time. The more robust bacteria from Chapter 3, *P. putida* KT2440, was selected for this portion of the dissertation because it had a lower adverse response to higher doses of resin; the surface area to volume ratio in the 3D-printed channel would be much higher than it was in either of the assays described previously, so this bacteria was chosen to minimize the risk of the bacteria failing to survive at all. The 3D-printed channel was treated with an extended water rinse and extra UV exposure, since these treatment methods were successful in improving cell viability previously. Additionally, a hydrogel barrier membrane was incorporated to allow for diffusive transport of carbon substrates, oxygen, and other relevant molecules. The following are the major contributions and key findings of Chapter 4:

1. A simple 3D-printed millifluidic device was designed for microbial cell culture such that it could be readily adapted for a variety of different cell types and communities.
2. A novel method was developed to pattern PEGDA hydrogel barriers *in situ* within 3D-printed channels made of acrylate and methacrylate polymers, using UV-initiated free-radical polymerization to cross-link the PEGDA.
3. Diffusion of toluidine blue tracer dye through hydrogel barriers was measured experimentally and compared to theoretical calculations and COMSOL Multiphysics simulations to better characterize the transport properties of the PEGDA barrier.

a. COMSOL simulations and theoretical calculations suggest that diffusion of toluidine blue tracer dye under the given conditions can be accurately approximated using 1D unsteady-state Fickian diffusion assumptions.
b. The effective diffusivity of toluidine blue through the PEGDA barrier was the same as through liquid water, so it is likely the toluidine blue molecule is small enough that it is able to pass through the water pores at this cross-link density.

4. A proof-of-concept cell culture experiment showed that *P. putida* KT2440 bacteria successfully grew inside a 3D-printed channel over a period of 44 h.
    a. GFP-producing cells could be visualized through a polished device with immersion oil using fluorescence microscopy.
    b. Clusters of cells could be observed as areas of localized high fluorescence intensity near the PEGDA barrier on the side of the media supply channel, where fresh oxygen and substrate were being supplied via diffusive transport through the hydrogel.
    c. Fluorescence intensity of cell clusters increased between images taken at 22 h and 44 h, indicating cells were still alive and actively producing GFP during this time period.

5.3 Significance and Applications

Each of the microfabrication methods developed over the course of this dissertation research can thus be employed for designing and controlling microhabitat devices for use in cell culture applications.

While the microelectrodes discussed in Chapter 2 were not chosen as the method for producing oxygen in initial termite testing, this new method for selectively and chemically bonding gold to PDMS vertical sidewalls could be useful in a variety of other applications within microfluidics. Since these microelectrodes are chemically bonded, they may be more resistant to flow or surface degradation than physically deposited electrodes. This could be useful in applications like microfluidic Coulter counters, which measure changes in resistance as a cell flows across the electrodes, or in microfluidic fuel cells which would ideally operate over an extended period of time.

The biocompatibility testing performed in Chapter 3 may be the first of its kind demonstrated for microbial cells. Only a minimal amount of biocompatibility testing has been performed on 3D-printed resins with model organisms and to date, the only published studies examine zebrafish embryos, not bacteria. Therefore, the results showing that there is in fact a dose-response to resin for bacteria cells, and that treatments can be performed on the polymer to drastically reduce biotoxicity may be important in expanding the use of STL 3D-printers in biological applications. Additionally, the assays described here were designed to be widely adaptable for a variety of different cells and organisms.

The proof-of-concept device described in Chapter 4 demonstrated that a bacteria monoculture could be successfully grown and observed using fluorescence microscopy over an extended period of time. To the author's knowledge, this has not been previously shown in the literature. This may demonstrate the capabilities of additive manufacturing for cell culture applications, when these fabrication methods had previously been avoided due to biocompatibility and optical clarity issues. Furthermore, the PEGDA barriers and the patterning

methods developed to construct them may be useful to many applications where controllable diffusive transport is required in a microfluidic or millifluidic design.

This array of engineering tools may be useful in advancing the field of gradient bioengineering and promoting microenvironment control for culturing the termite microbiome and a wide array of other complex cell communities from diverse natural systems.

5.4 Future Work

Even though other methods are being used to deliver oxygen in the current version of termite culture devices, it is possible that future versions could include upstream oxygen generation using microelectrodes. However, problems with bubble nucleation at the microelectrode surfaces need to be overcome in order to deliver a uniform concentration of dissolved oxygen. Additionally, repeatability and improvements to patterning resolution would need to be implemented if the electrode size needs to be reduced in a smaller channel design; this could be accomplished by using a mask aligner for photopatterning steps, but would require extra time in the already lengthy procedure. If these microelectrodes were to be fabricated in larger numbers, optimization of the various surface chemistry steps would significantly help reduce the time and costly materials needed. Lastly, improvements to patterning for electrical leads connecting the microelectrodes to the power supply would be necessary; the carbon black leads are very large and difficult to pattern reproducibly, but metal leads could be printed at a high resolution using inkjet printing or sputtering methods.

For the biocompatibility tests developed in Chapter 3, testing with other cell types would be extremely informative, as would testing with other resin formulations or brands. Additionally, it would be useful to move to a design where the entire wells or well plate is constructed from

3D-printed resin; in this way, we could test higher SA:V ratios to more accurately model the ratios for millifluidic channels. Preliminary testing has been conducted to design and print well cartridges that fit into a common platform compatible with a plate reader. Growth curve experiments have been performed in this format, and initial results showed that *E. coli* XL1B cells were even more sensitive to untreated 3D-printed resin than in wells with only a printed disk, but these results need to be repeated. Additionally, improvements to optical clarity of resins and printer resolution would significantly reduce the variability of the biocompatibility testing conducted in the plate reader.

The COMSOL Multiphysics models developed in Chapter 4 for toluidine blue dye diffusion through PEGDA could be used to predict transport of other molecules through PEGDA. Conducting diffusion experiments with a variety of tracer dyes of different sizes would be helpful in further characterizing transport through PEGDA barriers and could be used to determine at which point molecules are large enough to be impeded by the cross-linked hydrogel. Analytical or microscopy methods to determine the pore size, porosity, or tortuosity of the cross-linked hydrogel would be useful in more accurately modeling transport through this barrier. Additionally, in-line measurements could be conducted for substrate or oxygen concentration in the perfusion channels before and after the cell culture region, consumption by the cells could be incorporated into the COMSOL simulation to model cell growth kinetics within the 3D-printed channel. As for adjusting the design of the PEGDA barrier, transport through hydrogels of different cross-linking densities could be measured by varying the molecular weight and concentration of the polymer. Ideally, one would move towards hydrogel barriers with a shorter distance between the perfusion and cell culture channels and a wider

cross-sectional area for diffusion, in order to reduce the time needed for a molecule to diffuse through the barrier.

The 3D-printed microbial cell culture channel experiment may be the most interesting to pursue in future work. This experiment could be repeated with different bacteria strains or with a co-culture of cells. One interesting example of a simple co-culture that could be investigated is RFP-producing *E. coli* XL1B and GFP-producing *P. putida*. The *E. coli* is able to grow in more anaerobic conditions, while the *P. putida* requires higher oxygen levels. It would be interesting to grow these cells together in an oxygen gradient and visualize where cells of each species are able to survive using fluorescence microscopy. Eventually, this device construction could be used with cells harvested from the termite microbiome. However, for viewing non-fluorescent microbes through the 3D-printed channel as well as one can view them through glass and PDMS, optical clarity and printing resolution must be drastically improved; with the field of additive manufacturing progressing as quickly as it is, this may be possible in the next few years. Despite this, 3D-printed devices, provided they can be treated to prevent biotoxicity to the microbes, may work better in some respects than the PDMS used in current generations. This is because the 3D-printed resin polymer has a much lower oxygen permeability than PDMS, so the oxygen diffusing into the culture region would be reduced, which would be beneficial for the sensitive anaerobic termite microbes.

References

1. M. Funke, A. Buchenauer, U. Schnakenberg, W. Mokwa, S. Diederichs, A. Mertens, C. Müller, F. Kensy and J. Büchs, *Biotechnology and Bioengineering*, 2010, **107**, 497-505.
2. M. J. Gonzalez-Guerrero, J. P. Esquivel, D. Sanchez-Molas, P. Godignon, F. X. Munoz, F. J. del Campo, F. Giroud, S. D. Minteer and N. Sabate, *Lab on a Chip*, 2013, **13**, 2972-2979.
3. C. M. Moore, S. D. Minteer and R. S. Martin, *Lab on a Chip*, 2005, **5**, 218-225.
4. J. Diao, L. Young, S. Kim, E. A. Fogarty, S. M. Heilman, P. Zhou, M. L. Shuler, M. Wu and M. P. DeLisa, *Lab on a Chip*, 2006, **6**, 381-388.
5. L. M. Lanning, R. M. Ford and T. Long, *Biotechnology and bioengineering*, 2008, **100**, 653-663.
6. T. Long and R. M. Ford, *Environmental science & technology*, 2009, **43**, 1546-1552.
7. D. A. Markov, P. C. Samson, D. K. Schaffer, A. Dhummakupt, J. P. Wikswo and L. M. Shor, *Journal of Visualized Experiments*, 2010, **39**.
8. E. Cimetta, C. Cannizzaro, R. James, T. Biechele, R. T. Moon, N. Elvassore and G. Vunjak-Novakovic, *Lab on a chip*, 2010, **10**, 3277-3283.
9. L. Businaro, A. De Ninno, G. Schiavoni, V. Lucarini, G. Ciasca, A. Gerardino, F. Belardelli, L. Gabriele and F. Mattei, *Lab on a Chip*, 2013, **13**, 229-239.
10. H. Ma, T. Liu, J. Qin and B. Lin, *Electrophoresis*, 2010, **31**, 1599-1605.
11. J. Kim, M. Hegde and A. Jayaraman, *Lab on a Chip*, 2010, **10**, 43-50.
12. S. Chung, R. Sudo, P. J. Mack, C.-R. Wan, V. Vickerman and R. D. Kamm, *Lab on a Chip*, 2009, **9**, 269-275.
13. E. K. Sackmann, A. L. Fulton and D. J. Beebe, *Nature*, 2014, **507**, 181-189.
14. A. K. Au, W. Lee and A. Folch, *Lab on a Chip*, 2014, **14**, 1294-1301.
15. N. Bhattacharjee, A. Urrios, S. Kang and A. Folch, *Lab on a Chip*, 2016, **16**, 1720-1742.
16. C. Chen, Y. Wang, S. Y. Lockwood and D. M. Spence, *Analyst*, 2014, **139**, 3219-3226.
17. C. M. B. Ho, S. H. Ng, K. H. H. Li and Y.-J. Yoon, *Lab on a Chip*, 2015, **15**, 3627-3637.
18. L. E. Bertassoni, M. Cecconi, V. Manoharan, M. Nikkhah, J. Hjortnaes, A. L. Cristino, G. Barabaschi, D. Demarchi, M. R. Dokmeci, Y. Yang and A. Khademhosseini, *Lab on a Chip*, 2014, **14**, 2202-2211.
19. A. J. Capel, S. Edmondson, S. D. R. Christie, R. D. Goodridge, R. J. Bibb and M. Thurstans, *Lab on a Chip*, 2013, **13**, 4583-4590.
20. P. J. Kitson, M. H. Rosnes, V. Sans, V. Dragone and L. Cronin, *Lab on a Chip*, 2012, **12**, 3267-3271.
21. A. Lee, *Lab on a Chip*, 2013, **13**, 1660-1661.
22. G. Comina, A. Suska and D. Filippini, *Lab on a Chip*, 2014, DOI: 10.1039/C4LC00394B.
23. A. Waldbaur, H. Rapp, K. Lange and B. E. Rapp, *Analytical Methods*, 2011, **3**, 2681-2716.
24. S. Waheed, J. M. Cabot, N. P. Macdonald, T. Lewis, R. M. Guijt, B. Paull and M. C. Breadmore, *Lab on a Chip*, 2016, DOI: 10.1039/C6LC00284F.
25. A. K. Au, N. Bhattacharjee, L. F. Horowitz, T. C. Chang and A. Folch, *Lab on a Chip*, 2015, **15**, 1934-1941.
26. L. Nejdl, J. Kudr, K. Cihalova, D. Chudobova, M. Zurek, L. Zalud, L. Kopecny, F. Burian, B. Ruttkay–Nedecky, S. Krizkova, M. Konecna, D. Hynek, P. Kopel, J. Prasek, V. Adam and R. Kizek, *ELECTROPHORESIS*, 2014, **35**, 2333-2345.
27. S. Takenaga, B. Schneider, E. Erbay, M. Biselli, T. Schnitzler, M. J. Schöning and T. Wagner, *physica status solidi (a)*, 2015, **212**, 1347-1352.
28. K. B. Anderson, S. Y. Lockwood, R. S. Martin and D. M. Spence, *Analytical Chemistry*, 2013, **85**, 5622-5626.
29. W. Lee, D. Kwon, W. Choi, G. Y. Jung, A. K. Au, A. Folch and S. Jeon, *Scientific Reports*, 2015, **5**, 7717.

30. S. M. Oskui, G. Diamante, C. Liao, W. Shi, J. Gan, D. Schlenk and W. H. Grover, *Environmental Science & Technology Letters*, 2016, **3**, 1-6.
31. F. Zhu, J. Skommer, N. P. Macdonald, T. Friedrich, J. Kaslin and D. Wlodkowic, *Biomicrofluidics*, 2015, **9**, 046502.
32. N. P. Macdonald, F. Zhu, C. J. Hall, J. Reboud, P. S. Crosier, E. E. Patton, D. Wlodkowic and J. M. Cooper, *Lab on a Chip*, 2016, **16**, 291-297.
33. J. A. Breznak and A. Brune, *Annual Review of Entomology*, 1994, **39**, 453-487.
34. H. Watanabe and G. Tokuda, *Annu Rev Entomol*, 2010, **55**, 609-632.
35. A. Brune, *Nat Rev Micro*, 2014, **12**, 168-180.
36. R. Chandra, H. Takeuchi and T. Hasegawa, *Renewable and Sustainable Energy Reviews*, 2012, **16**, 1462-1476.
37. A. Brune, D. Emerson and J. A. Breznak, *Applied and environmental microbiology*, 1995, **61**, 2681-2687.
38. F. A. Bertolino, I. E. De Vito, G. A. Messina, H. Fernández and J. Raba, *Journal of Electroanalytical Chemistry*, 2011, **651**, 204-210.
39. E. Bitziou, M. E. Snowden, M. B. Joseph, S. J. Leigh, J. A. Covington, J. V. Macpherson and P. R. Unwin, *Journal of Electroanalytical Chemistry*, 2013, **692**, 72-79.
40. X. Zhang, C. Chen, J. Li, L. Zhang and E. Wang, *Analytical Chemistry*, 2013, **85**, 5335-5339.
41. J. Parisi, L. Su and Y. Lei, *Lab on a Chip*, 2013, **13**, 1501-1508.
42. Y. J. Kim, J. E. Jones, H. Li, H. Yampara-Iquise, G. Zheng, C. A. Carson, M. Cooperstock, M. Sherman and Q. Yu, *Journal of Electroanalytical Chemistry*, 2013, **702**, 72-78.
43. A. Sahin, K. Dooley, D. M. Cropek, A. C. West and S. Banta, *Sensors and Actuators B: Chemical*, 2011, **158**, 353-360.
44. X. Hu, Q. He, H. Lu and H. Chen, *Journal of Electroanalytical Chemistry*, 2010, **638**, 21-27.
45. N. Lewpiriyawong, K. Kandaswamy, C. Yang, V. Ivanov and R. Stocker, *Analytical Chemistry*, 2011, **83**, 9579-9585.
46. S. H. Ling, Y. C. Lam and K. S. Chian, *Analytical Chemistry*, 2012, **84**, 6463-6470.
47. J. S. Mellors, W. A. Black, A. G. Chambers, J. A. Starkey, N. A. Lacher and J. M. Ramsey, *Analytical Chemistry*, 2013, **85**, 4100-4106.
48. J. Wu, K. Xu, J. P. Landers and S. G. Weber, *Analytical Chemistry*, 2013, **85**, 3095-3103.
49. R. Galindo, A. Dector, L. G. Arriaga, S. Gutiérrez and P. Herrasti, *Journal of Electroanalytical Chemistry*, 2012, **671**, 38-43.
50. D. Morales-Acosta, H. Rodriguez, L. A. Godinez and L. G. Arriaga, *Journal of Power Sources*, 2010, **195**, 1862-1865.
51. F. M. Cuevas-Muniz, M. Guerra-Balcazar, J. P. Esquivel, N. Sabate, L. G. Arriaga and J. Ledesma-Garcia, *Journal of Power Sources*, 2012, **216**, 297-303.
52. M. Guerra-Balcázar, D. Morales-Acosta, F. Castaneda, J. Ledesma-García and L. G. Arriaga, *Electrochemistry Communications*, 2010, **12**, 864-867.
53. L. Abad, F. Javier Del Campo, F. X. Munoz, L. J. Fernandez, D. Calavia, G. Colom, J. P. Salvador, M. P. Marco, V. Escamilla-Gomez, B. Esteban-Fernandez de Avila, S. Campuzano, M. Pedrero, J. M. Pingarron, N. Godino, R. Gorkin, 3rd and J. Ducree, *Electrophoresis*, 2012, **33**.
54. P. J. Castle and P. W. Bohn, *Analytical Chemistry*, 2005, **77**.
55. Z. Hao, H. Chen and D. Ma, *Analytical Chemistry*, 2009, **81**, 8649-8653.
56. G. H. Kwon, Y. Y. Choi, J. Y. Park, D. H. Woo, K. B. Lee, J. H. Kim and S. H. Lee, *Lab on a Chip*, 2010, **10**, 1604-1610.
57. B. Mustin and B. Stoeber, *Lab Chip*, 2012, **12**, 4702-4708.
58. J. Deng, A. Dhummakupt, P. C. Samson, J. P. Wikswo and L. M. Shor, *Analytical Chemistry*, 2013, **85**, 5411-5419.
59. G. Whitesides, E. Ostuni, S. Takayama, X. Jiang and D. Ingber, *Annual Review of Biomedical Engineering*, 2001, **3**, 335-373.

60. R. Mukhopadhyay, *Analytical Chemistry*, 2007, **79**, 3248-3253.
61. S. W. Hu, X. Q. Ren, M. Bachman, C. E. Sims, G. P. Li and N. L. Allbritton, *Analytical Chemistry*, 2004, **76**, 1865-1870.
62. Y. L. Wang, H. H. Lai, M. Bachman, C. E. Sims, G. P. Li and N. L. Allbritton, *Analytical Chemistry*, 2005, **77**, 7539-7546.
63. M. H. Schneider, Y. Tran and P. Tabeling, *Langmuir*, 2011, **27**, 1232-1240.
64. M. H. Schneider, H. Willaime, Y. Tran, F. Rezgui and P. Tabeling, *Analytical Chemistry*, 2010, **82**, 8848-8855.
65. U. Tallarek, E. Rapp, H. Sann, U. Reichl and A. Seidel-Morgenstern, *Langmuir*, 2003, **19**, 4527-4531.
66. A. A. Gorman and M. A. J. Rodgers, *Journal of the American Chemical Society*, 1986, **108**, 5074-5078.
67. J. M. Drake, P. Levitz, N. J. Turro, K. S. Nitsche and K. F. Cassidy, *Journal of Physical Chemistry*, 1988, **92**, 4680-4684.
68. G. M. Walker, M. S. Ozers and D. J. Beebe, *Biomedical Microdevices*, 2002, **4**, 161-166.
69. S. S. Cutie, D. E. Henton, C. Powell, R. E. Reim, P. B. Smith and T. L. Staples, *J. Appl. Polym. Sci.*, 1997, **64**, 577-589.
70. Y. Kim and J. Yi, *Korean J. Chem. Eng.*, 2008, **25**, 383-385.
71. F. J. H. Hol and C. Dekker, *Science*, 2014, **346**.
72. K. C. Bhargava, B. Thompson and N. Malmstadt, *Proceedings of the National Academy of Sciences of the United States of America*, 2014, **111**, 15013-15018.
73. K. G. Lee, K. J. Park, S. Seok, S. Shin, D. H. Kim, J. Y. Park, Y. S. Heo, S. J. Lee and T. J. Lee, *RSC Advances*, 2014, **4**, 32876-32880.
74. H. Seitz, W. Rieder, S. Irsen, B. Leukers and C. Tille, *Journal of Biomedical Materials Research Part B: Applied Biomaterials*, 2005, **74B**, 782-788.
75. F. C. Fierz, F. Beckmann, M. Huser, S. H. Irsen, B. Leukers, F. Witte, Ö. Degistirici, A. Andronache, M. Thie and B. Müller, *Biomaterials*, 2008, **29**, 3799-3806.
76. M. S. Mannoor, Z. Jiang, T. James, Y. L. Kong, K. A. Malatesta, W. O. Soboyejo, N. Verma, D. H. Gracias and M. C. McAlpine, *Nano Letters*, 2013, **13**, 2634-2639.
77. N. N. Zein, I. A. Hanouneh, P. D. Bishop, M. Samaan, B. Eghtesad, C. Quintini, C. Miller, L. Yerian and R. Klatte, *Liver Transplantation*, 2013, **19**, 1304-1310.
78. B. C. Gross, J. L. Erkal, S. Y. Lockwood, C. Chen and D. M. Spence, *Analytical Chemistry*, 2014, **86**, 3240-3253.
79. M. Di Lorenzo, A. R. Thomson, K. Schneider, P. J. Cameron and I. Ieropoulos, *Biosensors and Bioelectronics*, 2014, **62**, 182-188.
80. Z. Zguris, How Mechanical Properties of Stereolithography 3D Prints are Affected by UV Curing [White Paper], https://formlabs.com/media/upload/How-Mechanical-Properties-of-SLA-3D-Prints-Are-Affected-by-UV-Curing.pdf, (accessed November 5, 2016).
81. Clear Photoactive Resin for Form 1, Form 1plus, Form 2, Safety Data Sheet, https://formlabs.com/media/upload/Clear-SDS_u324bsC.pdf, (accessed November 5, 2016).
82. J. W. Stansbury, *Dental materials : official publication of the Academy of Dental Materials*, 2012, **28**, 13-22.
83. M. Espinosa-Urgel, A. Salido and J. L. Ramos, *J Bacteriol*, 2000, **182**, 2363-2369.
84. J. L. Ramos, E. Díaz, D. Dowling, V. de Lorenzo, S. Molin, F. O'Gara, C. Ramos and K. N. Timmis, *Biotechnology (N Y)*, 1994, **12**, 1349-1356.
85. K. E. Nelson, C. Weinel, I. T. Paulsen, R. J. Dodson, H. Hilbert, V. A. Martins dos Santos, D. E. Fouts, S. R. Gill, M. Pop, M. Holmes, L. Brinkac, M. Beanan, R. T. DeBoy, S. Daugherty, J. Kolonay, R. Madupu, W. Nelson, O. White, J. Peterson, H. Khouri, I. Hance, P. Chris Lee, E. Holtzapple, D. Scanlan, K. Tran, A. Moazzez, T. Utterback, M. Rizzo, K. Lee, D. Kosack, D. Moestl, H. Wedler, J. Lauber, D. Stjepandic, J. Hoheisel, M. Straetz, S. Heim, C. Kiewitz, J. A.

Eisen, K. N. Timmis, A. Dusterhoft, B. Tummler and C. M. Fraser, *Environ Microbiol*, 2002, **4**, 799-808.
86. M. L. Schuler and F. Kargi, *Bioprocess Engineering: Basic Concepts*, Prentice-Hall, Inc., Upper Saddle River, NJ, Second edn., 2002.
87. D. B. Weibel, W. R. DiLuzio and G. M. Whitesides, *Nature Reviews Microbiology*, 2007, **5**, 209-218.
88. J.-Y. Cheng, M.-H. Yen, C.-T. Kuo and T.-H. Young, *Biomicrofluidics*, 2008, **2**, -.
89. T. M. Keenan, C. W. Frevert, A. Wu, V. Wong and A. Folch, *Lab Chip*, 2010, **10**, 116-122.
90. J. Choi, Y.-G. Jung, J. Kim, S. Kim, Y. Jung, H. Na and S. Kwon, *Lab on a Chip*, 2013, **13**, 280-287.
91. F. Ding, S. H. Hsu, D. H. Wu and W. Y. Chiang, *Journal of Biomaterials Science, Polymer Edition*, 2009, **20**, 605-618.
92. G. G. Ferrer, M. M. Pradas, J. L. G. Ribelles, F. R. Colomer, I. Castilla-Cortazar and A. Vidaurre, *European Polymer Journal*, 2010, **46**, 774-782.
93. D. Or, S. Phutane and A. Dechesne, *Vadose Zone Journal*, 2007, **6**, 298-305.
94. Y. Wu, S. Joseph and N. R. Aluru, *The Journal of Physical Chemistry B*, 2009, **113**, 3512-3520.
95. B. G. Chung, K.-H. Lee, A. Khademhosseini and S.-H. Lee, *Lab on a Chip*, 2012, **12**, 45-59.
96. N. Thaitrong, N. M. Toriello, N. Del Bueno and R. A. Mathies, *Analytical Chemistry*, 2009, **81**, 1371-1377.
97. A. Hatch, E. Garcia and P. Yager, *Proceedings of the IEEE*, 2004, **92**, 126-139.
98. J. A. Burdick, A. Khademhosseini and R. Langer, *Langmuir*, 2004, **20**, 5153-5156.
99. P. Kim, H. E. Jeong, A. Khademhosseini and K. Y. Suh, *Lab on a Chip*, 2006, **6**, 1432-1437.
100. Y. Luo and M. S. Shoichet, *Biomacromolecules*, 2004, **5**, 2315-2323.
101. M. Kim and T. Kim, *Analytical Chemistry*, 2010, **82**, 9401-9409.
102. S.-F. Chong, J. H. Lee, A. N. Zelikin and F. Caruso, *Langmuir*, 2011, **27**, 1724-1730.
103. C. P. Huang, J. Lu, H. Seon, A. P. Lee, L. A. Flanagan, H.-Y. Kim, A. J. Putnam and N. L. Jeon, *Lab on a Chip*, 2009, **9**, 1740-1748.
104. T. Frisk, S. Rydholm, T. Liebmann, H. A. Svahn, G. Stemme and H. Brismar, *Electrophoresis*, 2007, **28**, 4705-4712.
105. S. Han, K. Yang, Y. Shin, J. S. Lee, R. D. Kamm, S. Chung and S.-W. Cho, *Lab on a Chip*, 2012, **12**, 2305-2308.
106. G. S. Jeong, S. Han, Y. Shin, G. H. Kwon, R. D. Kamm, S.-H. Lee and S. Chung, *Analytical Chemistry*, 2011, **83**, 8454-8459.
107. C. R. Kothapalli, E. van Veen, S. de Valence, S. Chung, I. K. Zervantonakis, F. B. Gertler and R. D. Kamm, *Lab on a Chip*, 2011, **11**, 497-507.
108. V. V. Abhyankar, M. W. Toepke, C. L. Cortesio, M. A. Lokuta, A. Huttenlocher and D. J. Beebe, *Lab Chip*, 2008, **8**, 1507-1515.
109. S. Turri, M. Levi, E. Emilitri, R. Suriano and R. Bongiovanni, *Macromolecular Chemistry and Physics*, 2010, **211**, 879-887.
110. G. Papavasiliou, P. Songprawat, V. Perez-Luna, E. Hammes, M. Morris, Y.-C. Chiu and E. Brey, *Tissue Engineering - Part C: Methods*, 2008, **14**, 129-140.
111. A. Khademhosseini, C. Bettinger, J. M. Karp, J. Yeh, Y. Ling, J. Borenstein, J. Fukuda and R. Langer, *Journal of Biomaterials Science-Polymer Edition*, 2006, **17**, 1221-1240.
112. A. Khademhosseini, J. Yeh, S. Jon, G. Eng, K. Y. Suh, J. A. Burdick and R. Langer, *Lab on a Chip*, 2004, **4**, 425-430.
113. M. B. Mellott, K. Searcy and M. V. Pishko, *Biomaterials*, 2001, **22**, 929-941.
114. Z. Liu, L. Xiao, B. Xu, Y. Zhang, A. F. T. Mak, Y. Li, W.-Y. Man and M. Yang, *Biomicrofluidics*, 2012, **6**.
115. H. Xu, J. Wu, C.-C. Chu and M. L. Shuler, *Biomedical Microdevices*, 2012, **14**, 409-418.

116. W. Saadi, S. W. Rhee, F. Lin, B. Vahidi, B. G. Chung and N. L. Jeon, *Biomedical Microdevices*, 2007, **9**, 627-635.
117. L. J. Halverson and M. K. Firestone, *Applied and environmental microbiology*, 2000, **66**, 2414-2421.
118. A. L. Kadilak, Y. Liu, S. Shrestha, J. R. Bernard, W. E. Mustain and L. M. Shor, *Journal of Electroanalytical Chemistry*, 2014, **727**, 141-147.
119. M. J. Goudie, A. P. Ghuman, S. B. Collins, R. M. Pidaparti and H. Handa, *Journal of Drug Delivery*, 2016, **2016**, 7913616.
120. E. L. Cussler, *Diffusion: Mass Transfer in Fluid Systems*, Cambridge University Press, New York, NY, Third edn., 2009.